Investigation of defects and microstructure in nanoporous Au

By

C. LAKSHMANAN

PHYS 02 2013 04 002

Indira Gandhi Centre for Atomic Research

A thesis
Submitted to
The Board of Studies in Physical Sciences

In partial fulfillment of requirements for the Degree of
DOCTOR OF PHILOSOPHY
of
HOMI BHABHA NATIONAL INSTITUTE

August, 2018

Homi Bhabha National Institute

Recommendations of the Viva Voce Committee

As members of the Viva Voce Committee, we certify that we have read the dissertation prepared by Mr. C. Lakshmanan entitled "Investigation of defects and microstructure in nanoporous Au" and recommend that it may be accepted as fulfilling the thesis requirement for the award of Degree of Doctor of Philosophy.

Chairman - Dr. C. S. Sundar **Date:** 7/2/2019

Guide / Convener - Dr. R. Rajaraman **Date:** 7.2.2019

Co-guide - Dr. R. N. Viswanath **Date:** 7/2/2019

Examiner - Dr. K. Sivaji **Date:** Feb 7, 2019

Member 1- Dr. G. Amarendra **Date:**

Member 2- Dr. Tom Mathews **Date:** 07/02/2019

Final approval and acceptance of this thesis is contingent upon the candidate's submission of the final copies of the thesis to HBNI.

We hereby certify that we have read this thesis prepared under our direction and recommend that it may be accepted as fulfilling the thesis requirement.

Date:

Place: IGCAR, Kalpakkam

7.2.19

Dr. R. N. Viswanath
Co-guide

Dr. R. Rajaraman
Guide

Statement by Author

This dissertation has been submitted in partial fulfillment of requirements for an advanced degree at Homi Bhabha National Institute (HBNI) and is deposited in the Library to be made available to borrowers under rules of the HBNI.

Brief quotations from this dissertation are allowable without special permission, provided that accurate acknowledgement of source is made. Requests for permission for extended quotation from or reproduction of this manuscript in whole or in part may be granted by the Competent Authority of HBNI when in his or her judgment the proposed use of the material is in the interests of scholarship. In all other instances, however, permission must be obtained from the author.

C. Lakshmanan

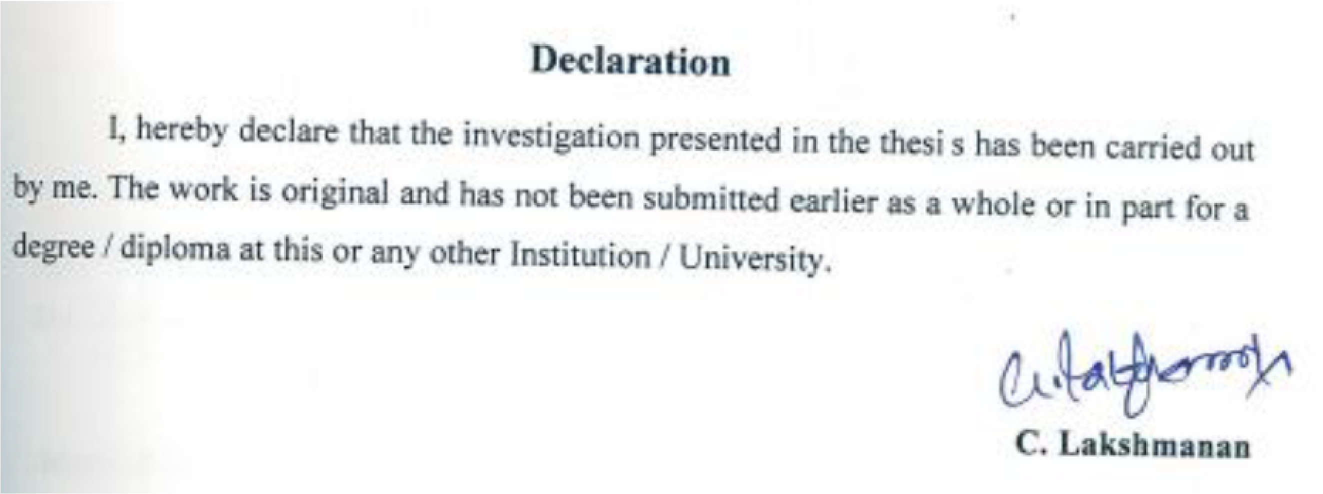

Declaration

I, hereby declare that the investigation presented in the thesi s has been carried out by me. The work is original and has not been submitted earlier as a whole or in part for a degree / diploma at this or any other Institution / University.

C. Lakshmanan

List of Publications

Journal

Published

1. **C. Lakshmanan**, R. N. Viswanath, S. R. Polaki, R. Rajaraman, S. Dash and A. K. Tyagi, "Surface area of nanoporous gold: Effect on temperature", Electrochimica Acta, 182 (2015)565. **doi:** https://doi.org/10.1016/j.electacta.2015.09.104

2. **C. Lakshmanan,** R. N. Viswanath, R. Rajaraman, S. Dash, G. Amarendra , C. S. Sundar, "Evolution of defects in nanoporous gold with annealing temperature using low-energy positron beam experiments", EuroPhysics Letters, 117, (2017) 48007.
doi: https://doi.org/10.1209/0295-5075/117/48007

3. **C. Lakshmanan**, Anil K. Behera, R. N. Viswanath, S. Amirthapandian, R. Rajaraman, G. Amarendra, "Microstructure studies in nanoporous Au: Effects on electro-oxidation" Scripta Materialia, 146 (2018) 68. **doi:** https://doi.org/10.1016/j.scriptamat.2017.11.018

4. **C. Lakshmanan**, R. N. Viswanath, Padmalochan Panda, B. Sundaravel, R. Rajaraman, G. Amarendra, " Effect of vacancies on Mechanical properties of pure and Fe^+ ion irradiated Nanoporous Au ". Applied Physics Letters. (under review).

Publications in the conference proceedings

1. **C. Lakshmanan**, R.N. Viswanath, S.R. Polaki, and R. Rajaraman, "Determination of surface area of nanoporous metals: Insights from double layer charging", AIP Conf. Proc. 1665, (2015)140033. d**oi:** https://doi.org/10.1063/1.4918242

2. **C. Lakshmanan**, R. N. Viswanath, R. Rajaraman, S. Dash and A. K. Tyagi, "Synthesis and electrochemical double layer characterization of nanoporous gold", Materials Today: Proc. 3 (2016) 1702. **doi:** https://doi.org/10.1016/j.matpr.2016.04.062

3. **C. Lakshmanan**, R.N. Viswanath, B.Sundaravel, R. Rajaraman, S. Dash, G. Amarendra, C. S. Sundar, "Defects in partially dealloyed Fe^+ irradiated $Ag_{75}Au_{25}$", AIP Conf. Proc. 1832, (2017) 140031. **doi:** https://doi.org/10.1063/1.4980813

Research paper presented in international / national conferences

1. **C. Lakshmanan**, R. N. Viswanath, Padmalochan Panda, R. Rajaraman, B. Sundaravel, R. Ramaseshan, G. Amarendra, C.S. Sundar, "Mechanical behavior of nanoporous Au: Insights from positron Annihilation Spectroscopy" RSM- MSENM- 2018, Kalpakkam, India, 7-9 May, 2018.

2. **C. Lakshmanan**, R. N. Viswanath, Padmalochan Panda, R. Rajaraman, B. Sundaravel, R. Ramaseshan, G. Amarendra, C.S. Sundar, "Positron studies of defects correlated mechanical properties in nanoporous Au" DAE BRNS Trombay Positron Meeting (POSITRON-2018), Mumbai, India, 23-24 March, 2018.

3. **C. Lakhsmanan**, R.N. Viswanath, R. Rajaraman, G. Amarendra, C.S. Sundar, "Defects in nanoporous Au: insights from variable energy positron Doppler broadening studies", MRSI symposium on "Advances in Functional and Exotic Materials" (AFEM-2018), MRSI – 2018, Tiruchirappalli, India, 14-16 February, 2018.

Other Publications (not included in thesis)

Journals

1. M. Vairavel, K. Saravanan, G. Jaiganesh, **C. Lakshmanan**, R. Rajaraman, B. Sundaravel, Binaykumar Panigrahi, G. Amarendra, "Oxygen and chromium solute interactions with interstitial and vacancy defects in Fe and FeCr alloy by ion channeling and *ab-initio* study" Acta Materialia, 143 (2018) 198. **doi:** https://doi.org/10.1016/j.actamat.2017.10.022

2. Anil K. Behera, R. N. Viswanath, **C. Lakshmanan**, K. K. Madapu, M. Kamruddin, T. Mathews "Synthesis, morphology and visible luminescence properties of vertically aligned lightly doped porous silicon nanowalls" Microporous and Mesoporous Materials 273 (2019) 99. **doi:** https://doi.org/10.1016/j.micromeso.2018.06.052

3. M. Vairavel, G. Jaiganesh, **C. Lakshmanan**, B. Sundaravel, R. Rajaraman, Binaykumar Panigrahi, G. Amarendra, "Defect structure of oxygen-vacancy clusters in O18 and self-ion implanted Fe(100) crystal by ion channeling and ab-initio study" (submitted to Acta Materialia)

4. Anil K. Behera, C. Lakshmanan, R. N. Viswanath, Tom Mathews, M. Kamruddin, P. Shankar, “Infrared induced enhancement of electrochemical hydrogen in flexible polymer supported carbon-palladium electrodes” (submitted to Heliyon).

__Research paper presented in international / national conferences__

1. Anil K. Behera, R.N. Viswanath, **C. Lakshmanan**, S.R. Polaki, R.M. Sarguna, Tom Mathews, “Thermal Oxidation and Nitridation of Si Nanowalls Prepared by Metal Assisted”, AIP Conf. Proc. 1942 (2018) 050062.
   doi: https://doi.org/10.1063/1.5028693

2. Anil K. Behra**, C. Lakshmanan**, R. N. Viswanath, R. Rajaraman, Tom Mathews, G. Amarendra, “Low energy positron beam studies on thermal oxidized Silicon Nanowalls” RSM- MSENM- 2018, Kalpakkam, India, 7-9 May, 2018.

3. K. Kamalakkannan, **C. Lakshmanan**, R. Rajaraman, K. Sivaji, B. Sundaravel, G. Amarendra, “Positron annihilation studies of N^+ and Al^+ implanted 6H-SiC Crystal” DAE BRNS Trombay Positron Meeting (POSITRON-2018), Mumbai, India, 23-24 March, 2018.

4. R. Mohandoss, **C. Lakshmanan**, K. K. Madapu, R. N. Viswanath, S. Dash and A. K. Tyagi, “Emission behavior of pure and lithium doped porous silicon”, Materials Today: Proc. 3 (2016) 1707. **doi:** https://doi.org/10.1016/j.matpr.2016.04.063

5. Anil K. Behera, R. N. Viswanath, **C. Lakshmanan**, S. R. Polaki, G. Mangamma, Tom Mathews, S. Dash, “Growth mechanism of silver nanoparticle on silicon substrate by galvanic displacement process”, International Conference on Advances in Nanomaterials and Nanotechnology, New Delhi 4-5 Nov, 2016.

6. Anil K. Behera, **C. Laksmanan**, R. N. Viswanath, S. Parida, T. Mathews, S. Dash, “Luminescence behavior of porous silicon in the presence of de-wetted silver”, Second International Conference on Materials Science and Technology (ICMST), Kerala, 5-8 June, 2016.

7. R. Mohandoss, **C. Lakshmanan**, K. K. Madapu, R.N. Viswanath, S. Dash, “Luminescent behavior in nanoporous silicon”, 3rd National Conference on Hierarchically Structure Materials (NCHSM 2015), SRM University, Chennai, India , 25-26 Feb, 2015

C. Lakshmanan

Dedicated to

Dr. A. P. J. Abdul Kalam Sir……

(1931 – 2015)

Science is beautiful gift to humanity, we should not distort it………

Acknowledgements

This thesis would not have been possible without the support and encouragement of many people who contributed directly and indirectly with valuable assistance. I feel short of words in expressing my gratitude for their help at various stages of this work.

I sincerely thank and express my deepest gratitude to my supervisor, Dr. R. Rajaraman for his expertise, understanding and patience and for giving me this incredible opportunity to become a part of his research group. His valuable suggestions, guidance, wholehearted support and encouragement throughout the course of the present work are inimitable.

I am deeply grateful to my thesis mentor Dr. R. N. Viswanath for initiating me into this fascinating, cutting-edge research project that I had the pleasure of working on. I have learnt, grown and gained invaluable research experience from him. I immensely thank him for the stimulating discussions, constructive criticisms and friendly discussions ranging from science to politics. The passion for fine research kindled by him would be commemorated forever.

I would like to thank my doctoral committee members Dr. C. S. Sundar, Chairman, Dr. G. Amarendra and Dr. Tom Mathews for their insightful comments, suggestions and encouragement which made me widen my research perspective that helped me gain a thorough understanding of my work.

I would like to thank the former directors of Indira Gandhi Centre for Atomic Research, Dr. P. R. Vasudeva Rao, Dr. S. A. V. Satyamurthy and the present director, Dr. A. K. Bhaduri for providing timely sanctions/approvals whenever necessary. I would like to express my deep gratitude to Dr. C. S. Sundar, Dr. M. P. Janawadkar and Dr. G. Amarendra former and present Group Directors, MSG for providing a conducive atmosphere during my entire research tenure at MSG. I thank Dr. Saibaba and Dr. Lakshmi Narasiman for the wonderful hospitality during my stay at JRF Enclave.

I deeply express my heart-felt thanks to my lab members Ms. M. Premila, Ms. J. Parimala, Dr. S. Abhaya and Mr. Renjith Ramachandran for continuous encouragement, feedbacks and careful review of my thesis and fruitful discussions. I am thankful to my

collaborators Dr. B. Sundaravel, Dr. R. Ramaseshan, Dr. S. Amirthapandian, Dr. S. R. Polaki, Mr. M. Vairavel, Mr. Padmalochan Panda, MSG for their scientific inputs and timely help in completing my experiments. My special thanks are due Dr. C. David, Dr. S. Balaji and Mr. Anand from MSG, Dr. Arup Dasgupta, Dr. K. G. Ragavendra, Mr. M. Sivakumar, Mr. Saikumaran, Miss. Vaishnavi Krupa from MMG; Dr. K. Ananthasivan, Dr. A. Senapati, Dr. Sanjaykumar, from MC&MFCG, for helping me carry out several experiments at various stages of my research work. I thank my lab mates Dr. R. Mohandoss, Anil, Alka, Bijay, Parvathy, Ravi and Vishnu for their friendly support and scientific discussions. A special word of thanks to LN_2 *plant members for providing unlimited quantities of* LN_2 *for my experiments.*

I wish to thank my friends, seniors and juniors for giving unforgettable moments during my stay at IGCAR and for the entire fun frolic that we had together. I thank Dr. Mahendran, Dr. Karthickeyan, Dr. Jai Ganesh, Dr. Anees, Dr. Devidas, Dr. Srini, Dr. Ragav, Dr. Jega, Ashwin, Nithi, Veera, Sekar, Thangam, Naveen Siva, Sai, Ragavendran, Thiru, Bharath, Dhilipan, Velraj, Bala. My fellow friends, who have been with me right from the beginning of my research work, - Radhikesh, Irshad, Nilakantha, Vairavel, Padmalochan, Zaibudheen, Santhosh, Shivang and Madusmita – No formal thanks, but I cherish the moments which we spent together.

I appreciate the sports ambience created by the Inter-lab cricket tournament, Intra-Enclave Cricket League and Enclave Badminton League. I would like to thank all my teachers, who had taught me at various stages of my educational career.

No words can suffice to thank my dear family for their patience, understanding and love. I owe highest gratitude and thanks to my dear parents Mr. S. Chelladurai & Smt. C. Meenakshi for their unsurpassed sacrifice, unconditional love & belief in every stage of my life – that has made me achieve this far. My heartiest thanks to my grandparents, my brother, sisters and brother and sister in- law for all their good wishes and affection. Special thanks to the tiny tots of our family - Sadhana, Nethra, Nila and Keerthi for their unparalleled joyous occasions that made me feel years younger.

Last but not least, I would like to place my deep sense of respect and reverence to a fascinating personality Dr. A. P. J. Abdul Kalam Sir to whom I dedicate my thesis.

Table of Contents

Synopsis

In nanomaterials, the fraction of atoms residing at the surface is very high as compared to their bulk counterpart. Hence, materials with large surface area or structures of smaller dimensions play a decisive role in controlling or enhancing their functional properties. Technical advances in nanomaterials development contribute tremendously to the progress of nanotechnology. Nanoporous metallic materials are a class of nanomaterials, possessing specific functionalities and exhibit novel physical, mechanical and catalytic properties sensitive to the surroundings. The basic microstructure in nanoporous metallic materials, resulting in their modified properties, consists of interconnected nanometer sized open network channels with similar sized dense continuous metallic struts. In such novel self-assembled nanoporous architecture, the open network channels and the dense continuous metallic struts are commonly called pores and ligaments. The typical size of pores or diameter of ligaments evolved in nanoporous metallic materials ranges from a few nm to a few tens of nanometer. Interestingly, the dimensions of the porous and ligament microstructures can be easily modified or controlled up to micrometer dimensions without affecting their skeleton porous-ligament morphological habit.

Among the nanoporous metallic materials, nanoporous gold (np- Au) has gained significant attention in recent years due to its novelty and potential functional applications as sensors, piezo-resistors and actuators [1]. Nanoporous Au exhibits novel materials characteristic features viz., chemical stability, biocompatibility, high conductivity and ultra-small structural features with high surface area and hence is used extensively in reactive fluids and gaseous medium is high. Nanoporous Au is ideally suited to investigate the scaling effect on physical and mechanical properties with structure size because of its unique annealing behavior: the length scale of both pore and ligaments can be easily adjusted by a thermal treatment over a wide range from 5 nm to the micron length scale. Collectively, the inherent properties of Au, combined with the possible effects due to porosity, make the np- Au a potential candidate material for both fundamental and applied research.

Designing a material from the atomic level to achieve a tailored response in extreme application is a grand challenge in materials research. An easy way to achieve np- Au with large surface area (10 – 70 m^2/g) is electrochemical dealloying. Dealloying method has the advantage of producing bicontinuous nanoporous structures with an assembly of interconnected ligaments and three-dimensional pores. However, to obtain such a nanoporous Au assembly upon electrochemical dealloying, a monolithic Au based starting alloy system is pre-requisite, because the porosity evolution is determined by a competition among the kinetic processes of selective removal of less noble metal atoms, and a capillary driven surface diffusion of Au [2]. In this context, Ag-Au binary alloy system satisfies the above requirements where the solubility of Ag and Au is uniform throughout the binary alloy phase. We have used $Ag_{75}Au_{25}$ binary alloy system as the master alloy to synthesis np- Au samples. It is a facile way to synthesis np- Au with a uniform distribution of ligaments with the diameter *d*, of ~ 5 nm.

Nanoporous Au with distinctly different surface states and high density of defects in the ligaments attract more attention in the functional materials field. The atomic defects in np- Au, retained during the evolution of nanoporosity, often play an important role in the variation of electronic, optical, catalytic, sensor and mechanical properties. Over the past few decades, many techniques have been developed with wider analyzing abilities to study the nature of lattice defects and chemical stoichiometry of surface and near-surface layers. Among all, positron annihilation spectroscopy has been widely used for the determination of atomic defects, including vacancies, vacancy cluster, dislocation, stacking faults and micro-voids [3].

In order to produce and understand the nature of distinct surface states of np- Au, electrochemical characterization coupled with microstructure studies were carried out. In electrochemical methods, Cyclic Voltammetry (CV) and Electrochemical Impedance Spectroscopy (EIS) are surface sensitive, which provides microscopic finger print of various electrochemical processes that occur during the dealloying and electro-oxidation/reduction processes from the current-voltage curves and Nyquist plots, respectively [4]. The vacancies and encased voids reside in the ligaments [5] and the associated lattice strain or stress field affects the mechanical robustness of np- Au. Thus, the microstructure of np- Au is of key importance for many engineering applications. Conventional electron microscopy study of nanoporous structure provides insufficient information about defect present in the ligaments. Hence, high-resolution Transmission Electron Microscope (HRTEM) along with Electron Energy Loss Spectroscopy (EELS) was used to study microstructure of np- Au with distinct surface states.

In addition to the importance of microstructure in np- Au with different surface states, quantification of the surface area is also of equal importance. A proper quantification of the surface area of np- Au is necessary for better understanding of the surface and size dependent properties since their specific surface reactivity depends on the delocalized atom density at the pore surface and their co-ordination with the interacting medium [6]. Here, we report the accurate measurement of specific surface area of np- Au using the double layer charging. These results are compared by using gas adsorption isotherms, electrochemical adsorption/desorption method and a geometrical model.

The study of defects in np- Au is of interest, given both fundamental research perspective and technological development. Due to the large concentration of atomic defects present in np- Au, a wide variation in catalytic and mechanical properties is observed in np- Au as compared to bulk Au [3]. Not much information is available in the literature on the generation of atomic defects during the formation of np- Au and their evolution with increase in annealing temperature. The defects evolved in ligament or ligament/pore interface during thermal coarsening is investigated using the techniques positron annihilation spectroscopy (PAS), high-resolution transmission electron microscopy (HRTEM) and scanning electron microscopy (SEM). In order to investigate the defect environment as a function of sample depth, variable energy positron Doppler broadening line shape measurements were recorded on different temperature annealed np-Au with the variation of positron beam energy. The positron diffusion length obtained from the analysis of the Doppler broadening line shape measurements provide information on the behavior of positron that is influenced by the presence of defects in np- Au samples [7]. Information on positron diffusion behavior in np-Au can also be obtained using a low energy positron beam experiments by looking at the spectral signatures for three-photon annihilations from positronium, (a positron-electron bound state). The fraction of impinging positrons that diffuse back to the entrance surface and annihilate as a positronium can be estimated from the measurement of relative fraction, f, of the $3\gamma/2\gamma$ yields. Measurement of positronium fraction $f_{(3\gamma/2\gamma)}$ provides precious information on surface state effects of the np- Au samples.

In nanomaterials, the scaling behavior of mechanical properties with structure size is often studied to verify the phenomenon “smaller is stronger”. A Hall-Petch exponent of -0.3 has been obtained for np- Au, with ligament diameter d, which is at variance with conventional Hall-Petch exponent of -0.5 reported for bulk Au. The decreased exponent -0.3 obtained has been rationalized by invoking the constrained motion of dislocation along the ligaments [8]. This suggests that apart from the ligament diameter in controlling the plasticity in np- Au, the concentration of defects evolved in the ligament networks also plays a key role in governing the mechanical behavior in np- Au, in particular the Hall-Petch scaling exponent value. In order to understand further about the correlation between the mechanical behavior and strain field of vacancy defects, we extended the defects and mechanical property studies to irradiated np- Au samples also. Studying the defects and mechanical behavior of pure and irradiated np- Au is necessary to understand the contribution of the defects that are generated in the ligaments towards mechanical behavior in the geometrically constrained three dimensional porous-ligament network architects.

The thesis is organized into seven chapters, and the contents of each chapter are outlined briefly:

Chapter 1 presents a brief introduction about nanoporous materials, in particular nanoporous Au and its physical, mechanical and chemical properties and potential applications. A comprehensive literature survey has been provided on nanoporous Au. Positron interaction with solids and nanoscale materials are discussed briefly. A dedicated section discussing the advancements in the mechanical behavior of nanoporous Au and its scaling behavior has been presented.

Chapter 2 contains brief description about electrochemical dealloying method and electrochemical characterization techniques. The experimental techniques positron lifetime spectroscopy and variable energy Doppler broadening spectroscopy to study the defect structures and the positron diffusion behaviour in the porous-ligament network architect are detailed briefly. The important characterization tools required for morphological, structural, and elemental analysis are also discussed. The principle of nanoindentation technique to analyze mechanical properties of np- Au is also introduced.

Chapter 3 includes detailed description about the synthesis of np- Au from $Ag_{75}Au_{25}$ binary alloy using electrochemical dealloying method and development of np- Au with distinctly different surface states viz., as-dealloyed, oxygen reduced and oxidized surface states achieved by cyclic voltammetry and electrochemical impedance spectroscopy measurements. Electrochemical measurements combined with HRTEM coupled EELS have been performed to follow the microstructural changes in np- Au. The microscopy results reveal that different types of lattice defects such as SFT are present in np- Au and oxide formed np- Au. It is shown that Au inter-planar spacing for Au (111) and Au (200) in the defect-concentrated regions in as- dealloyed np- Au has increased by 8 %, compared to clean metallic (oxygen reduced) np- Au. Noticeably, the stacking fault tetrahedral defects have disappeared in the oxygen reduced clean metallic np- Au sample.

Chapter 4 mainly deals with on measurements of the specific surface area of np- Au carried out both experimentally and analytically and the results obtained are compared with "geometrical ball-stick model." Nanoporous Au was investigated for temperature dependent properties like specific capacitance C_s and specific mass surface area α_m. An electrochemical double layer capacitance ratio method was employed to carry out these studies. It is shown that for reduced clean metallic nanoporous Au sample, the variation in $ln\ (C_s)$ versus $1/T$ plot is almost linear, which supports the negative temperature coefficient predicted by the double layer model. This observation is in direct contrast with positively charged as- dealloyed nanoporous Au that did not reveal any such trend. We compare the specific-mass surface area α_m of nanoporous Au values with the geometrical surface area α_g, obtained by using the “ball-stick geometrical model” coupled with scanning electron microscopy images. Evolution of ultra-small nanometric structures during dealloying renders positively charged as- dealloyed nanoporous Au vulnerable to oxidation and ligament coarsening upon its oxygen reduction. The validation of the specific-mass surface area obtained from the capacitance ratio method was confirmed by Brunauer-Emmett-Teller (BET) analysis and the process of adsorption/desorption of OH adsorbed species on pore surfaces in reduced clean metallic np- Au.

Chapter 5 explains positron interaction in np- Au using positron lifetime spectroscopy and low energy positron Doppler broadening spectroscopy. Positron lifetime in as-dealloyed np- Au samples indicated two-lifetime components, with different concentration of defects, identified with annihilation at vacancies within the ligaments and at the ligament-pore interface. The variation of these lifetime values with annealing temperature indicates that the vacancy type defects that migrated towards the ligament surfaces are prone to coarsening of the ligaments. Low energy positron Doppler broadening spectroscopy studies were also carried out to measure the Doppler line shape S- parameter with annealing temperature. The results show that the Doppler S-parameter increases gradually with increasing annealing temperature up to 473 K, after which it decreased and reached the bulk Au value at 1073 K. These stages are assigned to the initial growth of voids, followed by their breaking up associated with the ligament coarsening. The effective positron diffusion length L_{eff} in nanoporous gold has been extracted from the S-parameter versus incident positron beam energy plot using the VEPFIT code. The variation of L_{eff} with the ligament diameter, d, scales as $d^{1/3}$ that point to the diffusion of positrons along the ligament length. This is also substantiated by measurement of the positronium fraction.

Chapter 6 explains the correlation of the role of defects and its concentration with mechanical hardness behavior of both np- Au and bulk Au under irradiation conditions. Nanoindentation technique is used to measure the hardness in irradiated and bulk regions of the samples. Degree of hardness increased tremendously in np- Au compared to bulk Au under irradiation. This indicates that the dislocation motion is limited in irradiated np-Au compared to irradiated bulk Au. To understand the reason behind the hardness variation after irradiation, low energy positron beam Doppler broadening spectroscopy studies are carried out for probing the variation of defects concentration with annealing temperature. The linear correlation obtained between hardness and square root of vacancy concentration clearly explains that vacancy have significantly larger effects on mechanical behavior in np- Au. The slope of hardness H, vs. square root of vacancy concentration $C_v^{0.5}$ plot is high for irradiated np- Au compared to as- dealloyed np- Au and irradiated bulk Au, which indicates the strain field associated with the atomic defects is higher in irradiated np- Au.

Chapter 7 summaries the salient features of the thesis and discusses the outcome of the described work. It also presents the scope of the results on np- Au discussed in the present thesis for future technology.

List of Figures

List of tables

Chapter 1

Introduction

1.1. Nanoporous materials

In nanomaterials, the fraction of atoms that resides at the surface is very high compared to their bulk counterpart. Hence, materials with large surface area or structures of smaller dimensions play a decisive role in controlling or enhancing their functional properties. Technical advances in nanomaterials development, contribute tremendously to the progress of nanotechnology used today. In metal nanoparticles, the fraction of metal atoms residing at the surface region is very high compared to the bulk metal. Hence, the physical and chemical properties are controlled by the structure size and larger surface area of the metal nanoparticle wherein bulk material properties are controlled by volume. Introducing fine porosity into the bulk metal materials is a way to create such a characteristic feature [9]. Based on the pore dimensions and the features evolved during the formation of porosity, materials with pores can be subdivided into three categories, set out by IUPAC (International Union of Pure and Applied Chemistry) [10] Microporous materials: 0.2-2 nm; Mesoporous materials: 2-50 nm; Macroporous materials: 50-1000 nm. Hence, from IUPAC standpoint, the term nanoporous brings out an intrinsic size scale that goes from 1- 100 nm. Such a new class of low-density materials with complex morphology has received more attention in recent years.

Nanoporous metallic materials are a class of nanomaterial that possesses specific functionalities and exhibit physical, mechanical and catalytic properties sensitive to the surroundings. The basic microstructure in nanoporous metallic materials resulting in their modified properties consists of interconnected nanometer sized open network channels with similar sized dense continuous metallic struts. This novel self-assembled architecture, of a three-dimensional bicontinuous network of randomly interconnected metal nanoparticles are commonly called pores and nano-struts are commonly called as ligaments [2]. The typical size of pores or diameter of ligaments evolved in nanoporous metallic materials ranges from few nm to few tens of nanometer. Interestingly, the dimensions of the porous and ligament microstructure structures in nanoporous materials can be easily modified or controlled up to micrometer dimensions without affecting its skeleton porous-ligament morphological habit. Among the nanoporous metallic materials, nanoporous Au (np- Au) has gained more attention in recent years due to its novelty and potential functional applications as sensors, piezo-resistors, catalysts and actuators [1].

1.2. Nanoporous Au

Nanoporous Au exhibits novel material characteristic features viz., chemical stability, biocompatibility, high conductivity and structural features with less structure size and high surface area. Hence, it is extensively used in reactive fluids and gaseous medium. In addition, np- Au is ideally suited to investigate the scaling effect on physical and mechanical properties with structure size because of its unique annealing behavior: the length scale of both pore and ligaments can be easily adjusted by a thermal treatment over a wide range from 5 nm to the micron length scale. Collectively, the inherent properties of Au, combined with the possible effects due to porosity, make the np- Au a potential candidate material for technology, especially in the field of catalyst [11], sensors [12] and actuators [13,14].

Two dealloying routes have been mostly used to form np- Au: free corrosion dealloying [15,16] and electrochemical dealloying [1]. The former method refers to the process in which the alloy is submerged in an oxidizing electrolyte (typically aqueous nitric acid- HNO_3) that facilitates the dissolution of less noble element. In the electrochemical dealloying, on the other hand, the selective removal of the less noble element is facilitated by introducing an electric potential to the system. A three electrode electrochemical cell is employed for the dealloying process. It consists of a working electrode, a counter electrode and a reference electrode and an electrolyte (aqueous perchloric acid – $HClO_4$)[14]. Generally, a binary alloy system used for producing nanoporous structure by the dealloying process containing one element has to be less noble and electrochemically reactive. In Ag-Au binary alloy system, Ag is the less noble element, and Au is considered as highly noble. The driving force for dealloying is the difference in standard potential ΔE of the constituents Ag and Au. Two additional parameters that are essential to consider for the dealloying process are the so-called critical potential and the composition threshold or parting limit. Pickering, in his pioneering work, was the first one to introduce the relationship between the applied potential and dissolution rate that characterizes the electrochemical dealloying process [18]. Erlebacher showed via scanning electron microscopy (SEM) that dealloying Ag-Au produces ligament size around 5-10 nm [2] and their Monte Carlo model explained the mechanism involving the selective silver dissolution and gold diffusion during the dealloying [19].

Volume fraction (fraction of actual solid material in a given volume) of Au atoms in np- Au, or its relative density are substantially high compared to polymeric foams or commercial Aluminum foams. It is generally expressed as ρ^{*}/ ρ_{s}, where ρ^{*} denotes the density of the porous material and ρ_{s} is that of the corresponding dense material. Typical relative density for np- Au ranges between 0.25-0.42 with enlarged nodes at which the ligament connects. Figure 1.1 shows the scanning electron microscopy image of an as-dealloyed np- Au obtained from $Ag_{75}Au_{25}$ alloy [20]. It is worth to note that such a porous-ligament interconnected morphology is important when considering the deformation mechanics and mechanical properties of np- Au.

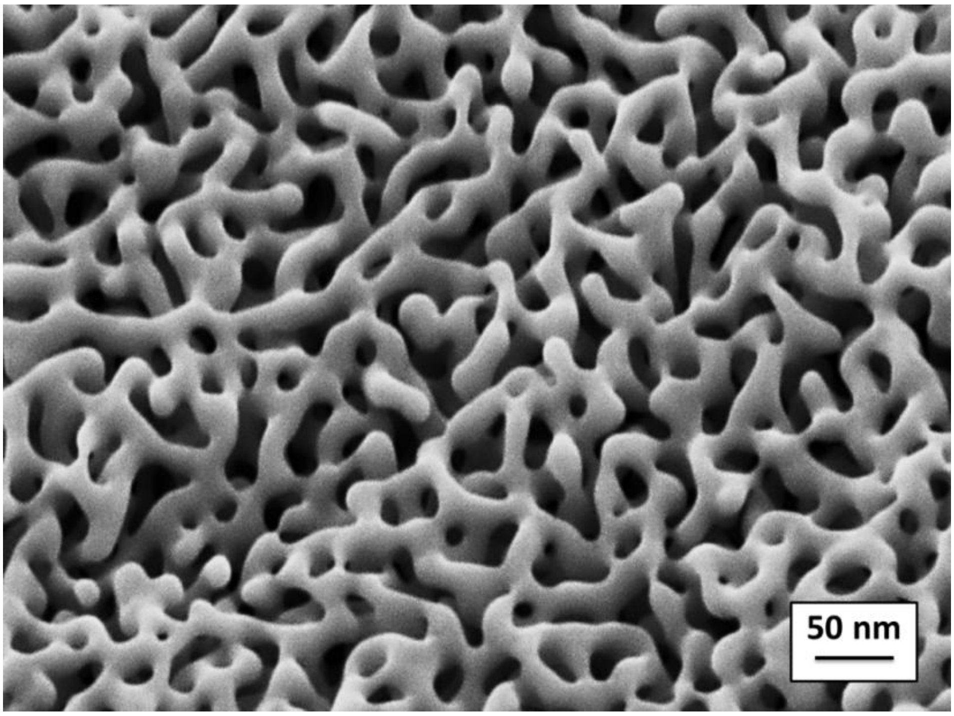

Fig. 1.1 Typical scanning electron micrograph image of np- Au microstructure synthesized by dealloying alloy $Ag_{75}Au_{25}$ [20].

Crystal defects including vacancy and vacancy cluster, dislocations, twins, and stacking faults [3,5,17] have been observed in the dealloyed np- Au. Generally, the dealloyed samples by electrochemical dealloying process have a high density of crystal defects in comparison with np- Au samples prepared simply by a free corrosion process. This is probably because of the presence of potential controlled excess charge flow across the electrode surfaces in the electrochemical dealloyed np- Au.

Nanoporous Au is an excellent candidate to study the size effect due to its unique temperature annealing nature in which both the ligaments diameter and pore diameter can be varied from 5 nm to few micron scales. It is observed that the ratio of the ligament to pore dimension can be easily adjusted without changing the macroscopic dimension of the sample (ligament connectivity, sample shape). Figure 1.2 shows the typical scanning electron microscopy images of np- Au in two length scale obtained by thermal annealing [21].

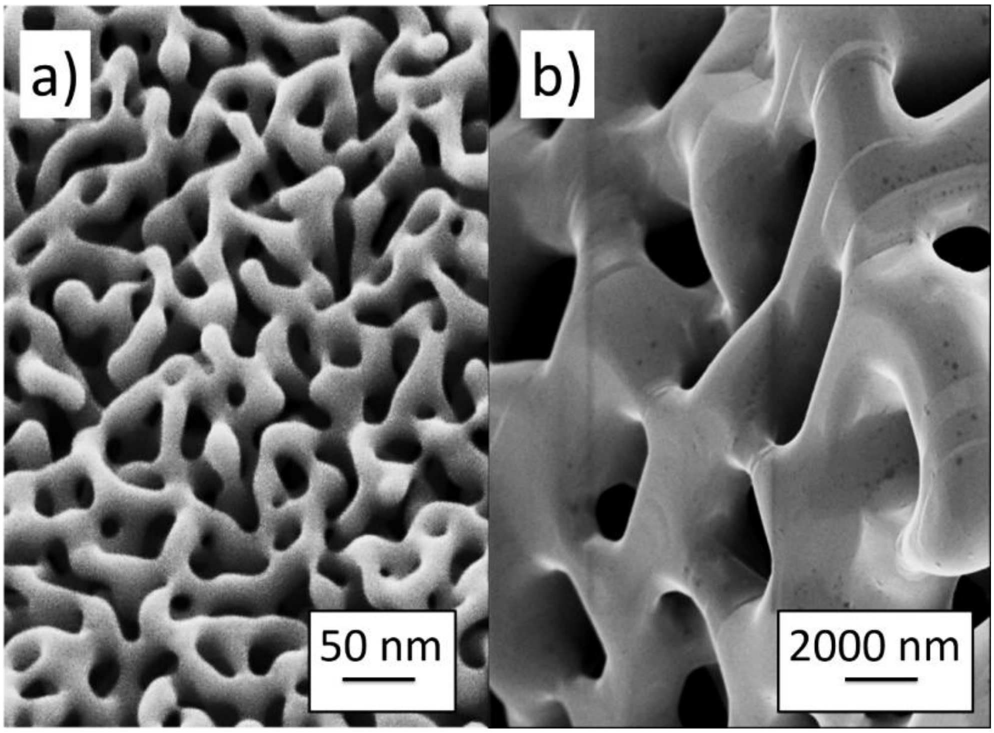

Fig. 1.2 Typical micrograph images of np- Au in two different length scales [21].

Viswanath et al. [3] identified the open volume defect presents in the ligament network using positron annihilation lifetime spectroscopy (PALS) coupled with scanning electron microscopy (SEM). The variation of positron annihilation lifetime parameters in np- Au with annealing temperature is shown in Figure 1.3. The results in Figure 1.3 summarizes that the thermalized positrons annihilated at vacancies within the ligaments and the ligament-pore interface [3]. The variation of lifetime parameter with annealing temperature shows distinct changes that correlate the migration of vacancies to the growth of ligaments. The same authors have demonstrated further the scaling behavior of hardness with ligament diameter and vacancy concentration in np- Au using Vickers hardness data and PALS [8].

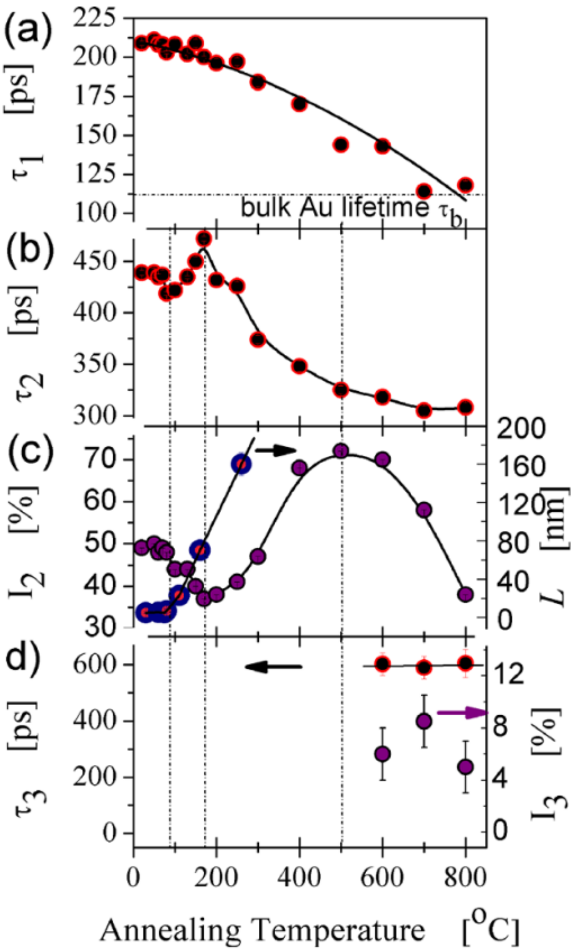

Fig. 1.3 Variation of positron lifetime parameters. a) τ_1 b) τ_2 c) I_2 and d) τ_3 with annealing temperature in np- Au. The right ordinate in panel c) shows the increase in the ligament diameter, L with temperature as obtained from SEM studies. The vertical dotted lines mark the distinctive stages, inferred from positron experiments, corresponding to the migration of vacancies at 85ºC, instability at the surface of ligaments at 175ºC and the transition to closed pore structure at 500ºC. Adopted from Ref. [3].

In nanomaterials, the scaling behavior of mechanical properties with structure size is often studied to verify the phenomenon of "smaller is stronger." Hall-Petch exponent of -0.3 has been reported for np- Au, with ligament diameter *d*, which is at variance with conventional Hall-Petch exponent of -0.5 reported for bulk Au [8] . The decreased exponent -0.3 obtained has been rationalized by invoking the constrained motion of dislocation along the ligaments, shown in Figure 1.4.

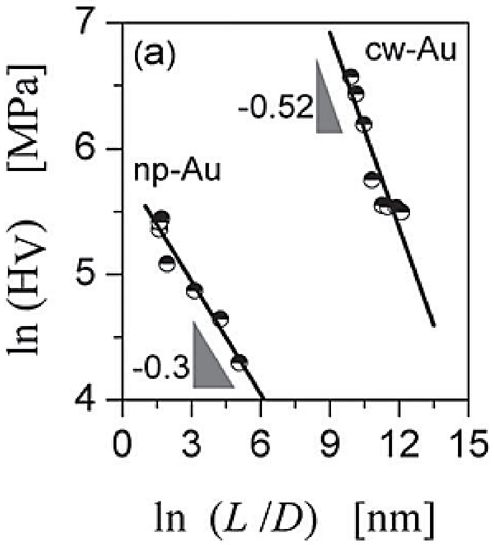

Fig. 1.4 Plot of ln(H_V) versus ln(*L/D*) for np- Au. Straight lines in the figure are the best empirical fit of the relation between hardness H_V and ligament size, *L* with a slope of -0.3 for np- Au and between hardness H_V and grain size, D with a slope of -0.52 for bulk Au. Adopted from Ref. [8].

This suggests that apart from the ligament diameter in controlling the plastic deformation behavior in np- Au, the microstructure evolved in the ensemble of porous-ligament network is also a critical parameter in governing the mechanical behavior in np-Au, especially its Hall-Petch scaling exponent value.

1.3. Functional properties of nanoporous Au: Role of defects

Since the present thesis deals with different kind of defect studies in nanoporous metallic materials, it is helpful to give a brief introduction on defects classification by their dimensionality. It is worth noting that point defects have distinct features compared to other defects in crystal systems and their entropy will also be increased by the increase in the density of point defects. Therefore, open volume defects, including point defects are highly sensitive to functional properties than other high-dimensional defects. Although over the past several decades, physical and chemical properties have dominant applications by nanostructured materials, considerable attention has been paid recently towards the defect studies on metal nanoparticles. The structure size and surface area correlate with defects in the metal nanoparticles and significantly alter physical, chemical properties in contrast to their macroscopic bulk counterparts.

There are very few experimental techniques that can identify and quantify the lattice defects which are classified as direct and indirect methods. The group of direct techniques consists of microscope methods, such as transmission or scanning electron microscopy (TEM or SEM) and electron back scattered diffraction (EBSD) is very useful in the study of grain boundary structure and its defects. Electrical resistometry [22], X-ray line profile analysis (XLPA) [23] and positron annihilation spectroscopy (PAS) [7] are typical examples of indirect methods. Lattice defects such as dislocations and stacking faults can be observed in TEM images due to contrast caused by their strain fields. XLPA method is very effective to study defects by analyzing the breadth and shape of the diffraction peak profiles. The X-ray diffraction peak profiles broaden mainly due to crystallite size, dislocation and planar defects especially stacking faults and twin boundaries. The electrical resistivity measurements of metallic crystalline materials find out the vacancies, interstitials, dislocation, defect-impurity complexes, stacking faults and grain boundaries due to scattering of conduction electrons by phonons. Among all above techniques, positron annihilation spectroscopy (PAS) is a non-destructive characterization technique, which can probe material on the atomic scale (10^{-7} - 10^{-4}) and can be used to identify all kinds of open volume defects. Furthermore, in a PAS experiment, it is possible to derive certain defect-specific annihilation parameters that can be used to distinguish between various types of defects like monovacancy, dislocation loops and vacancy clusters [24].

This method enables the determination of vacancy concentration as well as type and density of dislocations. PAS technique includes different techniques such as positron annihilation lifetime spectroscopy (PALS), angular correlation of electron-positron annihilation radiation (ACAR) and Doppler broadening spectroscopy (DBS). DBS measures the momentum distribution of the annihilating positron-electron pair by measuring the energies of the annihilation photons and is suitable for probing the chemical surroundings of the defects. To analyze the surface and subsurface defects in thin film and irradiated materials, energy controlled positron beam is used by variable energy positron Doppler broadening spectroscopy. Positron annihilation lifetime spectroscopy on nanomaterials appears as a unique tool to study the interfacial structure of solids. Schafer and Würschum [25,26] performed positron lifetime measurements on the nanocrystalline metallic samples and proposed that positron gets trapped effectively in crystalline interface and interface intersection regions.

Defects present in Au ligaments influence significantly the volumetric effect (size effect) in np- Au and the defects that are localized on the ligament surface or ligament/pore interface (surface effect) serve to alter or modify its functional properties. A volumetric shrinkage of ~ 30% in np- Au was reported by Parida et al. [17]. The authors relate the volume shrinkage effect observed in np- Au during in-situ dealloying process to plastic deformation and indicated that detailed micro characterization of np-Au is needed to understand further the potential importance of np- Au for functional applications.

Microstructural characterization studies using high resolution transmission electron microscopy HRTEM and scanning electron microscopy will be effective tool to understand the role of defects in the governance of materials functionality. Rosner et al. conducted high-angle annular dark-field scanning transmission electron microscopy (HAADF-STEM) study on as- dealloyed np- Au leaf and reported that individual Au ligaments contain encased voids [5]. Evolution of the ligament structure in np- Au through dealloying route is known to create lattice strain. Petegam et al. studied the internal strain in np- Au using X-ray diffraction technique in in-situ and ex-situ conditions and reported that the np- Au has similar grain morphology and orientation as that of the parent alloy sample used for the dealloying experiments [27].

Microscopically, the ligament structure adopts a unique configuration in which the atomic defects and oxygen-containing species interact together with the Au atoms and contribute to the overall functioning of the ligament-porous network structure. Recent studies exploring the catalytic effect in np- Au suggested that Au is catalytically active not only in its chemically pure form but, also, holding variety of catalytic reactions in the presence of easily reducible oxygen adsorbed species [28–30]. It has been demonstrated recently that nanoporous Au / oxide hybrid electrodes (Li-O_2, MnO_2, etc.,) performs as pseudo-capacitor and indicated that their charge transfer and storage efficiencies depend on structure size and accessible surface area of nanoporous network [31]. This implies that np- Au with modified Au ligament surfaces is suitable as electrodes for super-capacitor applications [32].

Bulk Au has very poor catalytic activation of H_2, O_2, CO [33]. However, when gold is dispersed in the form of nanoscale particles, it behaves as a good catalyst. Further investigation on nano scaled Au may shed light on the origin of catalytic property of gold [11]. Unlike the nanoparticulate catalysts, dealloyed np- Au with high density of low coordinated Au atoms on ligament surfaces and defects like edge and kinks show excellent catalytic properties. Liu et al., have studied np- Au using the high-angle annular dark-field scanning transmission electron microscopy and reported that weakly-coordinated Au surface atoms residing at the ligament surfaces contribute intrinsically to the catalytic property of np- Au [28]. In line with discussion on intrinsic microstructure variations in np- Au to the catalytic properties, Zugic et al., have demonstrated, based on in-situ electron microscopy studies, that variation of oxygen-Au stoichiometry and atomic restructuring effect have a direct influence on various catalytic reactions, especially for selective alcohol oxidation reactions [29]. Although many reports point out that np- Au ceases to behave as a catalyst due to the existence of atomic defects in the ligaments, our practical goal is to develop mechanically stable np- Au for use in applications that require some mechanical integrity.

Most important parameters in controlling the mechanical properties of np- Au are structure size or ligament diameter and relative density or porosity. Li and Sieradzki investigated the presence of a ductile-brittle transition based on the ligament size in np- Au [34]. Balk et al. observed dislocation activity with nucleation followed by gliding of the dislocation along the ligament in np- Au during the in-situ mechanical indentation studies using transmission electron microscope (TEM) [35]. Gliding of nucleated dislocation defects within the ligament initiates plasticity. As regarding the plastic deformation behavior, Hodge *et al.* showed that the hardness of np- Au measured by nanoindentation decreases with the increasing characteristic length of the foam structure [36]. Figure 1.5 shows the compiled ligament yield strength data obtained with different relative densities and length scale of np- Au using the Gibson-Ashby relation [37], which is commonly used to study the mechanical strength of porous medium.

The plastic deformation in a confined sample volume can be realized through the nucleation and motion of newly generated dislocations and not by interaction or storage of existing dislocations as in the case of bulk. In solids with such small volumes high stresses are required for populating new dislocations. The scaling equation, developed by Gibson and Ashby, for conventional porous materials is used to obtain the ligament yield strength [37].

$$\sigma_y^M = C\sigma_y^L\left(\frac{\rho^*}{\rho_s}\right)^n \qquad (1.1)$$

Here (ρ^*/ρ_s) is the solid fraction (≤ 0.3), wherein ρ^* denotes the density of porous materials, and ρ_s denotes the density of the dense metal counterpart, n = 1.5 is a density exponent, and C is a proportionality constant ~ 0.3. Biener et al. explained from the analysis of nanoindentation data that np- Au is a high yield strength material and at 15 nm ligament diameter, the yield strength value is estimated as 1.5 GPa, close to the theoretical strength Au [38]. Further, Biener et al. demonstrated the variation of hardness of np- Au with relative densities ranging from 0.25-0.42 and ligament sizes from 10-100 nm thus bringing together the size and porosity dependent mechanical properties [39].

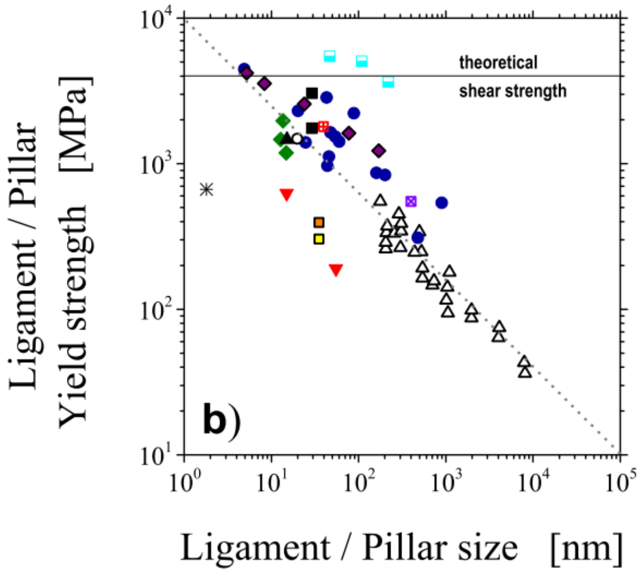

Fig. 1.5 Ligament yield strength of np- Au as a function of ligament diameter. Compiled experimental data were collected from different studies on np-Au. Adopted from Ref. [36] with most available data added.

It has been reported that mechanical properties (yield strength, hardness) of np-Au depend upon ligament size and relative density and that np- Au can be as strong as bulk Au. The yield strength of ligament in np- Au approaches the theoretical yield strength of Au. Along the same line of investigations, Volkert *et al.* showed that the yield strength of np- Au with 15 nm ligament size approaches the intrinsic strength of bulk Au [40]. Individual ligaments of np- Au with relative density of about 36% achieved a yield strength value of 1.5 GPa, which is close to the theoretical shear strength of bulk

Au. Hakamada et al. suggest that np- Au undergoes deformation similar to those of Au nanowires [41,42]. Consistent with the suggestion by Hakamada et al., results obtained from various experimental studies on np- Au in the present study also point out that the deformation of individual ligament is similar to the one of Au micropillars and nanowires [43,44].

Designing nanostructured metals with higher surface area to attain tailored response in extreme conditions such as nuclear radiation is a grand challenge in nanomaterials field because they provide the larger interfaces with smaller structure size that attract, absorb and annihilate defects. Radiation-induced defects diffusing quickly to surface and annihilating are the key factors in reducing the damage and imparting stability in certain nanomaterials. On account of that, nanoporous metals are considered as the best candidate materials for radiation tolerance because their large free surfaces act as sink to maximize defect recovery [45]. Since surfaces are perfect sinks, nanoporous metals, due to their high surface to volume ratio, have the potential to become a new class of radiation tolerant materials [46,47]. Bringa et al. have framed the optimum length scale for retaining radiation resistance behavior in np- Au using molecular dynamics (MD) simulations and basic experiments [48]. When the ligament or filament diameter is less than cascade length scale, the ligament melts and breaks with increase of radiation dose. On the other hand, if the ligament diameter is higher than the cascade length scale, the ligament behaves as a bulk material and tends to accumulate damage.

Results on radiation hardening in metallic materials using nanoindentation have been reported often in the literature [49]. Despite the abundant ongoing research on mechanical behavior on np- Au, there is limited knowledge available in the literature about the correlation between the mechanical properties and strain field of vacancy defects in as-prepared and irradiated np- Au. Study of the defects and mechanical behavior of pure and irradiated np- Au is found necessary to discern the contribution of the defects that are generated in the ligaments, to the mechanical behavior in the geometrically constrained three-dimensional porous-ligament network.

With the introduction as mentioned above, the present thesis motivates to synthesis np- Au using an electrochemical route, study the temperature dependent surface area in np- Au, microstructural features evolved in np- Au with ligament diameter, role of defects in the coarsening of np- Au skeleton ensemble, and size and defects coupled mechanical behavior in pure and Fe^+ ion irradiated np- Au.

Chapter 2

Experimental methods

This chapter deals with the experimental methods and characterization techniques used for the present thesis. Initial part of the chapter discusses in detailed manner about the fabrication and electrochemical characterization of nanoporous Au samples. Later part of the chapter describes experimental techniques that have been employed to investigate the physical, structural and mechanical properties of nanoporous Au samples.

2.1. Methods of sample preparation

2.1.1. Alloy preparation

A bicontinous metal void structure, i.e., nanoporous (np-) metal fabricated through selective dissolution (dealloying) method [2,14]. In this thesis work np- Au samples were prepared by electrochemical dealloying method from the master alloy $Ag_{75}Au_{25}$ (at.%). The AgAu binary alloy system was used to achieve np- Au because both of Au and Ag have face-centered-cubic structure with similar lattice parameter (4.08 Å) and exhibit solid solubility across the entire composition range [50] and no phase separation occurs during dealloying [17]. Figure 2.1 shows the binary phase diagram of AgAu alloy system.

The master alloy of composition $Ag_{75}Au_{25}$ was prepared by arc melting method where the high purity Ag (99.99%) and Au (99.99%) were obtained from Alfa Aesar®. Electric arc-furnace chamber, evacuated to create a vacuum (10^{-6} mbar) and filled with Argon gas to avoid oxidations, used during alloying to melt and mix the pure metal components. The arc-melting process was repeatedly carried out until the master alloy acquires a button shape. After melting, the alloy ingots were vacuum sealed in quartz ampoule and homogenized by annealing at 800^0C for 20 hrs. After homogenization, the master alloy ingots were subjected to cold-rolling to form a 200 µm thick foil. Prior to use in the dealloying process, the foils were cut into 2 cm x 2 cm samples by a diamond cutting machine. These master alloy samples were annealed at 700^{0}C for 10 hrs to remove frozen stress and then subjected to electrochemical dealloying studies.

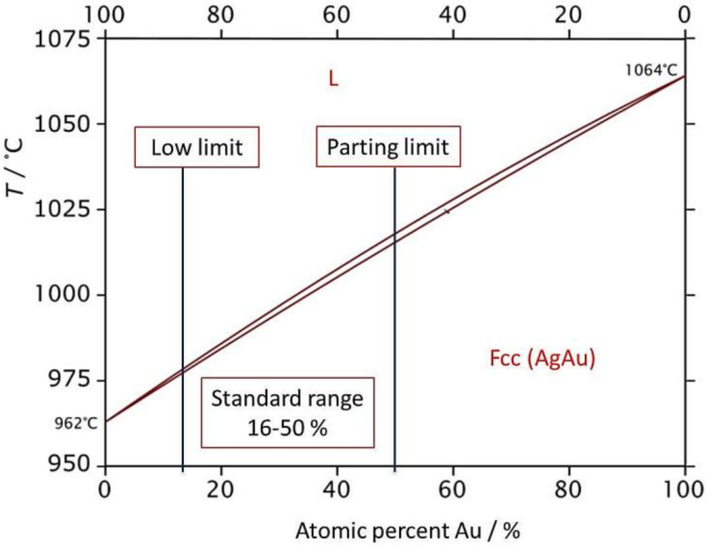

Fig. 2.1 Phase diagram of binary AgAu alloy system [50]. Based on initial alloy composition three regions are classifies to achieve nanoporous Au structure [51]. Reprinted with permission of ASM International. All rights reserved. www.asminternational.org.

2.1.2. Dealloying method

Dealloying is one of the most important methods to fabricate nanoporous materials. It is a common corrosion process which is defined as the selective electrolytic dissolution of electrochemically more active or less noble element from homogeneous binary alloy solid solution leaving uniform, random, and bicontinuous skeleton material that consists of almost more noble elements [12]. In this thesis, the $Ag_{75}Au_{25}$ master alloy is used where Au is a more noble element, and Ag is a less noble element. Here, the selective removal of Ag is driven by the applied electrochemical potential in the electrolyte (1M $HClO_4$), which is used to control the pore and ligament size compared to free corrosion methods [15,16]. The fine ligament size and pore size achieved by applying an electrochemical potential above the critical value [52].

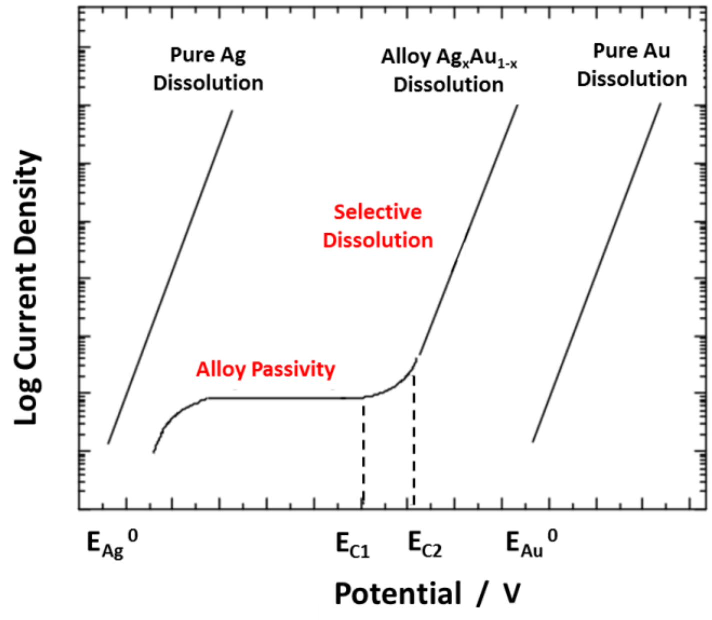

Fig. 2.2 Schematic illustration of the *I-E* behavior of pure metal Ag and Au dissolution and corresponding Ag_xAu_{1-x} alloy dissolution [53]. The dashed lines indicated the typical ambiguity in defining a critical potential.

Figure 2.2 shows schematic illustration of *I-E* curves for Ag, Au and AgAu binary alloy [53]. The difference in Standard reduction potential, determines the electrochemical activity of the alloy components, above 0.5 V (vs. *SHE*). In our system the difference in standard electrode potential of Ag and Au is:

$$E_{Au^{3+}/Au} - E_{Ag^{+}/Ag} = 0.80\,V \tag{2.1}$$

To avoid surface passivation and produce mechanically stable structure, the precursor alloy composition range of more noble (Au) element present in the master alloy should be within 16-50 % [19,51]. While dealloying, four possible mechanisms involves the formation of nanoporous metal from the binary alloy system:

(1) Simultaneous process of dissolution-restructuring mechanism: Dissolution of less noble element followed by restructuring of more noble element [2,54].

(2) Surface diffusion mechanism: only less noble element dissolves and atoms of more noble element cluster by surface diffusion. The coarsening was achieved by surface diffusion of more noble elements [55].

(3) Volume diffusion: to explain dealloying in bulk layers, Pickering and Wagner [56] suggested volume diffusion, where injection of vacancies into bulk to transport less noble element to the surface.

(4) Percolation model: Sieradzki et al. proposed this model where the continuously connected cluster of the less noble metal element must exist to facilitate dissolution [57]. Electrolyte penetrate into the bulk interior through the pathway provided by these less noble metal clusters

During dealloying, volume shrinkage would take place; usually, over 50% of their compositional atoms are dissolved. Parida et al. reported volume shrinkage up to 30% during electrochemical dealloying of master alloy $Ag_{75}Au_{25}$ alloy [17]. This volume shrinkage affects the relative density of the porous metals which is the most important determining parameter in the mechanical behavior of porous metal. A schematic of all the above mechanisms is given in Figure 2.3.

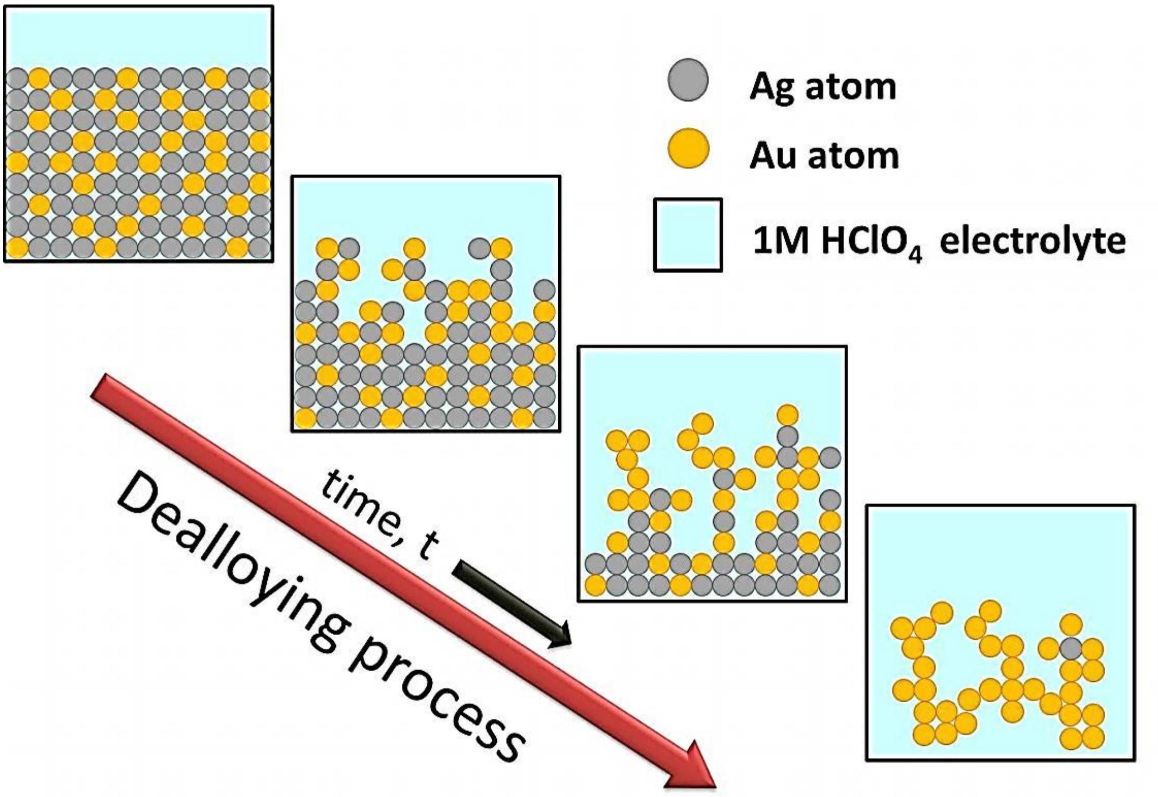

Fig. 2.3 Schematic illustration of dealloying mechanism of AgAu binary alloy.

2.2. Dealloying set-up

A typical three-electrode system was suggested to prepare the nanoporous metal samples through electrochemical dealloying process. The working electrode (WE) was master alloy $Ag_{75}Au_{25}$, Counter Electrode (CE) was the Ag coil, and Reference Electrode (RE) was pseudo Ag/AgCl electrode, and the 1M $HClO_4$ was used as the electrolyte.

2.2.1. Reference electrode preparation

The reference electrode (RE) was prepared by the electrochemical method, and it is called as pseudo Ag/AgCl reference electrode. The pseudo Ag/AgCl RE was prepared by oxidizing a pure Ag wire (0.5 mm thickness) at 0.90 V for about 120 s in 1M (mol L^{-1}) aqueous HCl solution. In this setup, WE is an Ag wire which will be used as pseudo Ag/AgCl RE in dealloying experiment and CE is another pure Ag wire. The pseudo Ag/AgCl coated RE is immediately rinsed with ultra-high pure deionized 18 MΩ water. The potential of pseudo Ag/AgCl versus standard Ag/AgCl (3M Saturated KCl) is -0.198 V and Standard Hydrogen Electrode (*SHE*) is -0.398 V.

2.2.2. Electrochemical Cell

The three-electrode cell configuration setup is adopted in this thesis to synthesize the np- Au sample, as schematically shown in Figure 2.4. In this configuration, the applied electrode potential of WE is maintained relative to the RE and the resulting current then passes between the WE and CE [58]. The general requirement for a RE is a reliable reference for potential control includes stability over time and temperature and reproducible electrode potential [59]. The lab made pseudo Ag/AgCl RE was chosen for low cost, nontoxic components and its compact size in the small cell arrangements compared to other electrodes.

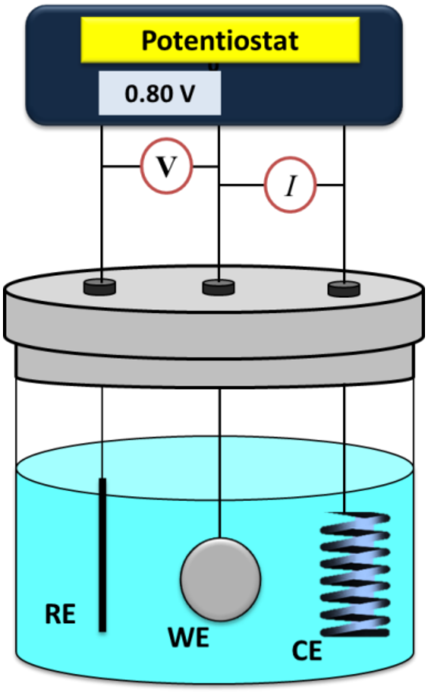

Fig. 2.4 A typical three electrode cell setup for dealloying process. WE: $Ag_{75}Au_{25}$ binary alloy; RE: Ag/AgCl electrode; CE: Ag coil in the $HClO_4$ electrolyte.

In the electrochemical dealloying process, all three electrodes are immersed in the electrolyte with separate distances in an electrochemical cell made by glassware. The dealloying is performed using chronoampeometry technique (CA) by applying a reduction potential of 0.80 V vs. pseudo Ag/AgCl RE controlled using a commercial potentiostat (PGSTAT 302N Metrohm Autolab e.v.) and monitoring dealloyed current. The dealloying potential increased stepwise up to 0.90 V slowly and the process is performed until the cell current decays to 10 μA and by this time all the silver atoms would have dissolved from the master alloy $Ag_{75}Au_{25}$. The dealloyed nanoporous Au sample had taken out from the cell and rinsed with ultra-high pure deionized water. Hereafter, electrochemically dealloyed np- Au sample will be subjected to as a working electrode (WE) for all electrochemical techniques such as Cyclic Voltammetry and Electrochemical Impedance Spectroscopy.

2.3. Electrochemical techniques

2.3.1. Cyclic Voltammetry

Cyclic Voltammetry (CV) is a dynamic in-situ electrochemical technique to measure anodic and cathodic current as a function of potential [58]. It is used to study the electro-oxidation/reduction events on noble metals and tune the interface behavior at the electrode surface [4]. The potential applied on WE, between upper E_2 and lower E_1, vertex potentials, is varied in a triangular wave manner with a scan rate $\upsilon = dE/dt$ within the potential window and measuring the resulting current. The scan direction is reversed when the potential reaches E_2, returning to the initial value E_1. The resulting current I plotted versus potential E for the anodic and cathodic potentials scans constitutes one cycle of the cyclic voltammogram. CV method offers the opportunity to understand the mechanism of electrosorption (adsorption/desorption) processes on noble metals, particularly formation of surface oxidation [4].

2.3.2. Electrochemical Impedance Spectroscopy

Electrochemical Impedance Spectroscopy (EIS) is a powerful tool to get insight of the electrode-electrolyte interface behavior [58]. WE is subjected to a sinusoidal AC signal with a defined frequency and a small amplitude, which is superimposed on the cell DC potential or current and resulting total impedance (Z) obtained from Nyquist plot (real (Z') vs. imaginary (Z'') part of impedance at corresponding frequency), Bode plot (phase angle (ϕ) vs. frequency), and frequency dependent capacitance [59]. In the absence of faradic reaction, EIS measurement can be interpreted via electronic circuit, containing a resistor in series with a capacitor element, where both elements represent the ohmic solution resistance and the capacitance of the double layer, respectively.

2.4. Positron annihilation spectroscopic techniques

The investigation of the structure and lattice defects in nanoporous materials is of high interest for material science. These atomic defects in nanoporous solids often play an essential role in the electronic, optical, catalytic, sensor and mechanical properties. Over last few decades, many techniques have been developed to analyze surfaces, near-surface layers and interfaces to study the lattice defects and its chemical environment changes, large number of experimental methods have been developed with widespread analyzing abilities. Among all, Positron techniques have been developed and applied in many different fields. Positrons provide a unique tool for non-destructive solid-state material characterization and have been used in different experimental techniques to study defects ranging from individual missing atoms to micro-voids [60]. In recent years, positrons have increasingly been used as a tool for investigating solids to get information on depth wise distribution of defects in porous materials such as nanoporous Au [7].

The positron is the antiparticle of the electron, in that it has the same rest mass, spin (1/2), and the same magnitude of electric charge, though with the opposite sign. In vacuum, it is stable and having the same lifetime as an electron. The existence of the positron was first proposed by Dirac [61,62] in 1928 as an explanation for the negative energy solutions obtained from the relativistically invariant wave equation. Soon after, the positron was discovered by Anderson in 1932 [63]; he observed that cloud chamber particle tracks resulting from the passage of cosmic rays which, when subjected to a magnetic field, showed a curvature identical to that expected for a particle with the mass-to-charge ratio of an electron but in the opposite direction. When positron interacts strongly with its antiparticle, the electron, mutual annihilation occurs. The mass-energy of the two particles is completely converted into two, or with a distinctly smaller probability (1/370) three gamma photons. These annihilated gamma rays reflect the information about electronic properties and chemical nature of the annihilated site, i.e., leaves a fingerprint in the annihilation radiation [64].

The positron characterization depends on the local density and local electron momentum. As discussed above the positron eventually annihilate with an electron with the emission of two anti-parallel 511 keV gamma rays. Detection of these annihilation events has led to the development of various positron annihilation spectroscopy techniques. However, we used two major techniques in this thesis; Positron Annihilation Lifetime Spectroscopy (PALS) and Doppler Broadening Spectroscopy (DBS). The positron lifetime is inversely dependent on the local electron density whereas the Doppler broadening spectroscopy on the local electron momentum [24].

2.4.1. Positron Sources

Positron can be produced either by pair production or by β^+ decay from radioactive nuclides.. Radionuclides (^{22}Na, ^{58}Co, ^{64}Cu, ^{68}Ge) are the most commonly used positron sources for experiments. Among all, ^{22}Na isotope is the most suitable for the positron annihilation experiments with relatively high positron yield of 90.4% and half-life of 2.6 years [65].

$$^{22}_{11}Na \rightarrow {}^{22}_{10}Ne + e^{+} + \nu + \gamma \qquad (2.2)$$

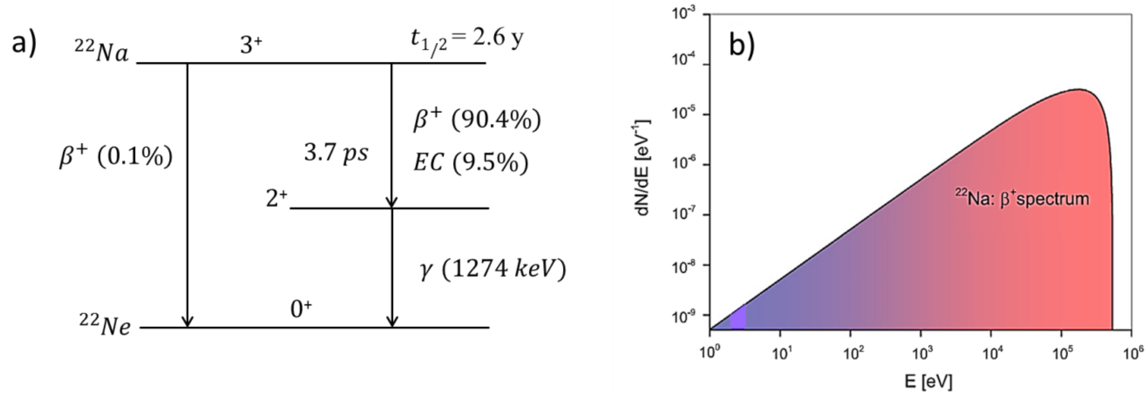

Fig. 2.5 a) schematic diagram of positron emission from ^{22}Na. b) Energy distribution curve of emitted positron from ^{22}Na (reproduced from Ref. [66])

^{22}Na (~10 μCi) source enclosed between thin (~4 μm) Ni foil has been used as the positron source for the conventional positron annihilation experiments. The decay scheme is shown in Figure 2.5 a). The 2$^+$ excited state is ^{22}Ne de-excites to ground state by emitting γ-ray of energy 1274 keV. The half-life of the excited (2$^+$) state in 3.7 ps, which is much smaller than the positron lifetime in the matter. Thus, the near simultaneous emission of 1274 keV γ-ray is considered as the birth signal of the β^+ particle (positron). The energy spectrum of ^{22}Na source extends up to an end point energy of 545 keV [66], as shown in Figure 2.5 b).

2.4.2. Positron interaction with matter

2.4.2.1. Implantation and Thermalization

An energetic positron incident on a solid surface will either backscatter or will get implanted into the matter. An implanted positron will get thermalized, during the implantation process, and then diffuse through the lattice until it eventually encounters an electron with which it will annihilate. Before reaching thermal equilibrium, it penetrates the material to an average depth $\bar{z}$, which is dependent on the implanted positron energy E_p, and sample density ρ. It means positron can probe the bulk of solid with an energy distribution as shown in Figure 2.5 b). Positron energy is lost during the implantation via various interaction mechanisms; it participates several ionization processes, exciton formation, and positron phonon interaction until it reaches thermal equilibrium. The kinetic energy of positron entering the solid is much larger than the thermal energy of diffusion, independent of the origin of the positron. The difference between this energy is dissipated in the crystal within the few picoseconds. The whole process is called thermalization. The implantation profile is a probability distribution which represents the depth at which positrons will thermalize. The positron interaction with matter is shown in Figure 2.6.

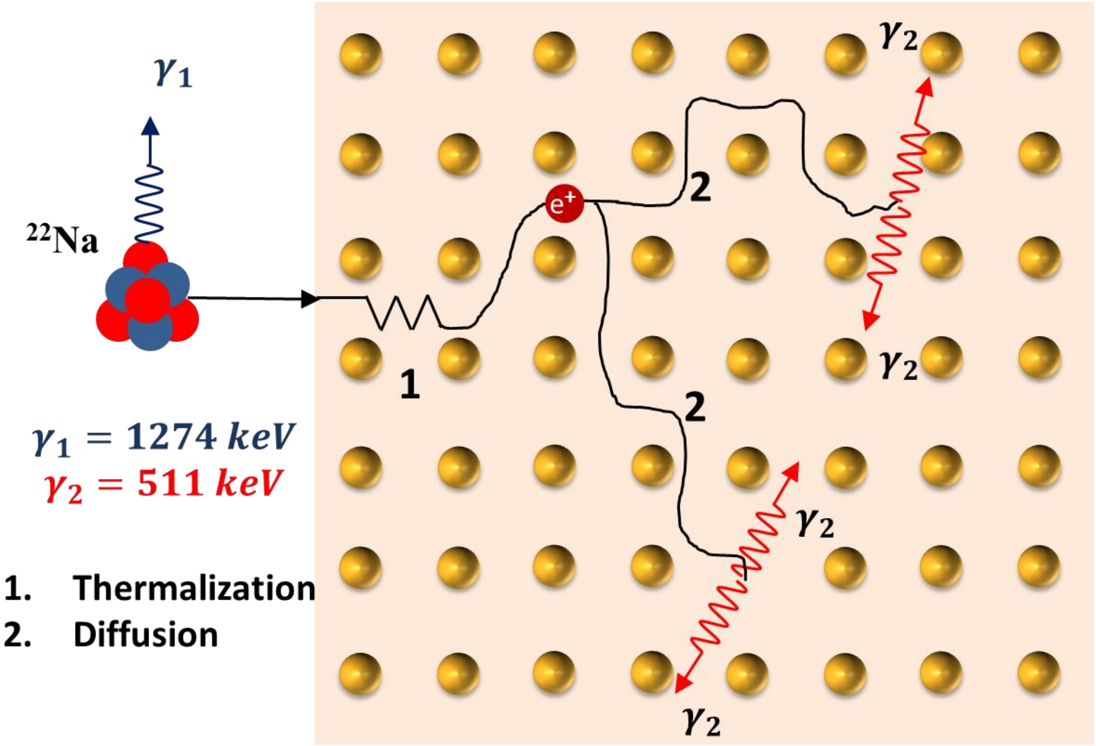

Fig. 2.6 Schematic of positron interaction with material.

While probing near surface region of samples with low energy positron beam, quantitative description of the implantation profile is needed, which is the depth distribution of the implanted positrons before diffusion. The distribution of positron or implantation profile $P(z,E_p)$ varies with implantation energy E_p, and the material density. The positron implantation profile is generally represented by a Makhovian implantation profile [67] given by,

$$P(z,E_p) = \frac{mz^{m-1}}{z_0^m}\exp\left[-\left(\frac{z^m}{z_0}\right)\right] \qquad (2.3)$$

where z is the depth from the sample surface, m = 2.0 for Si and z_0 depends on the positron energy E_p through relations,

$$z_0 = \frac{AE_p^n}{\rho\Gamma\left(1+\frac{1}{m}\right)} \qquad (2.4)$$

where Γ is gamma function and $\bar{z}$ is the mean implantation depth, ρ is the density of the sample in g/cc. n = 1.6 and A = 4.0 $\mu gcm^{-2}keV^{-n}$ for most of the metals and semiconductors. The mean implantation depth $\bar{z}$ can be calculated [68,69] by using,

$$\bar{z} = \frac{AE_p^n}{\rho} \quad (nm) \tag{2.5}$$

Increasing energy positron energy increases the mean implantation depth and width of the positron distribution for Au is shown in Figure 2.7.

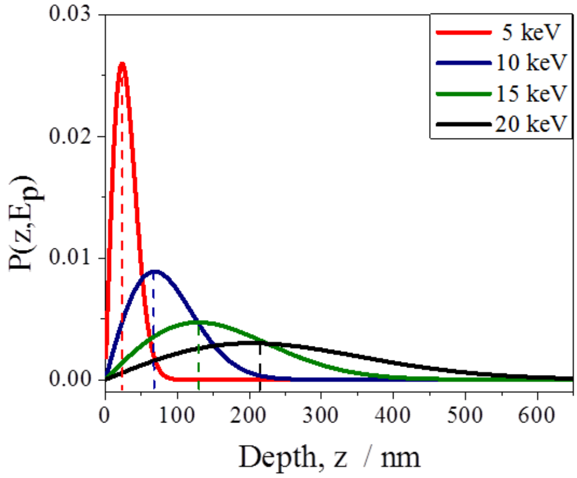

Fig. 2.7 Makhovian profile of positron implantation at various energies for Au. The dotted line shows the mean implantation depth ($\bar{z}$) for various positron implanted energies.

2.4.2.2. Diffusion and Trapping

When positron reaches thermal energies, they start to diffuse through the lattice and behave as a charged particle driven by electrostatic interactions and diffuse randomly as long as it is in a delocalized Bloch-state. Due to their positive charge, the positrons are repelled by nuclei and have their largest probability density in interstitial regions. This positron will have the following behaviors: (1) annihilate with an electron in bulk (2) trapped by the defect site and (3) diffuse back to the surface for the cases in which implantation energy is < 20keV.

The positron diffusion can be approximated by a steady state one-dimensional diffusion equation [24] given as,

$$D_+ \frac{\partial^2 n}{\partial z^2} - \frac{D_+ e}{kT} \frac{\partial}{\partial z} \left(\varepsilon(z) n(z)\right) - \frac{n(z)}{\tau_1} + n_0(z) = 0 \qquad (2.6)$$

where $n(z)$ is the positron probability density, D_+ is the positron diffusion coefficient, T is the temperature, $\varepsilon(z)$ is the electric field, e is the positron charge and $n_0(z)$ is the positron stopping rate at depth z which is independent of the implantation profile given in equation (2.6).

The positron diffusion length L_+, is defined as,

$$L_+ = \sqrt{\tau_b D_+} \qquad (2.7)$$

where τ_b is the defect-free bulk sample.

The thermalized positron reaches a defect site and it can be trapped i.e. the transition from the delocalized state to the localized state is called positron trapping [70]. The positron trapping rate κ describe how fast positron trapped to a defect d,

$$\kappa = \mu_d C_d \qquad (2.8)$$

μ_d is the specific trapping coefficient (10^{14}- 10^{16} s^{-1} at room temperature), C_d is the concentration of defects.

2.4.3. Positron Annihilation Lifetime Spectroscopy (PALS)

Positron lifetime in the material is characterized by the time distribution of annihilation events, and each event is defined as the time interval between the emission of 1274 keV and annihilation line of 511 keV. The annihilation rate of positron (λ) which is inverse of the lifetime(τ) of positron inside the solid and is directly proportional to the overlap of positron ($n_+(\mathbf{r})$) and electron ($n_-(\mathbf{r})$) densities and given as [24],

$$\lambda = \frac{1}{\tau} = \pi r_0^2 c \int n_+(r) n_-(r) \gamma dr \qquad (2.9)$$

where $\gamma = (1 + (\Delta n_{-}/n_{-})$ is the enhancement in electron density around the positron due to Coulomb attraction, r_0 is the classical electron radius, and c is the speed of light. When a vacancy is created by the removal of positive ion core, the net reduction in the local electron density is reflected as an increase in the lifetime of positron trapped at the site. The intensity of such a lifetime component gives the concentration of defect sites. The experimental lifetime spectrum can be understood with simple rate equations provided trapping of non-thermalized positron which is negligible and the non-interacting defects are homogeneously distributed in the sample. Under these conditions, the time-dependent positron diffusion equation for a sample with only one defect type can be written as,

$$\frac{dn_b(t)}{dt} = -\lambda_b n_b(t) - \kappa_1 n_b(t) \tag{2.10}$$

$$\frac{dn_d(t)}{dt} = -\lambda_d n_d(t) + \kappa_1 n_b(t) \tag{2.11}$$

The solution to the coupled differential equation is the decay spectrum which is expressed as,

$$D(t) = I_1 e^{-t/\tau_1} + I_2 e^{-t/\tau_d} \tag{2.12}$$

Here n_b is the fraction of positrons annihilating from the Bloch like delocalized state, $\lambda_b (= 1/\tau_b)$ is the annihilation rate in the defect-free State, κ_1 is the trapping rate of the defect d, and $\lambda_d (= 1/\tau_d)$ annihilation rate in the defect site which has n_d fraction of positrons annihilating from it. τ_d is the positron lifetime pertaining at defect *d*. I_1 and I_2 are the intensities of these two annihilation sites such that $I_1 + I_2 = 1$. $\tau_1 = 1/(\lambda_d + \kappa_1)$ is the reduced bulk lifetime in the presence of defect site. The actual lifetime spectrum is the absolute value of the time derivative of the expression shown in equation (2.12). Through the lifetime measurements, one tries to identify these lifetime components and thus get an idea of the defect species and their concentration in the sample.

To obtain the exponential decay spectrum composed of multiple slopes, i.e., multiple trap sites are present, the time difference between the birth of positrons (tagged by the 1274 keV gamma emission by Ne de-excitation) and death of positrons (tagged by 511 keV from e^-e^+ annihilation) is measured for each event. The generated spectrum is fitted with multiple exponentials which are convoluted with the Gaussian resolution function of the spectrometer. For *n* distinct sites of annihilation, *n* annihilation rates exist and the decay spectrum. Therefore, a spectrum can be written as [24],

$$N(t) = G(t) \otimes \sum_{i=1}^{k+1} \frac{I_i}{\tau_i}\ exp\left(\frac{-t}{\tau_i}\right) \tag{2.13}$$

N(t) is the number of positron in the solid at the time *t*. A_i is constant in the positron state *i*, λ_i is the annihilation rate in the positron state *I* and *G(t)* is Gaussian instrumental resolution function.

The experimental setup for this is a fast-fast positron lifetime unit represented by the block diagram shown in Figure 2.8. A BaF_2 scintillator - photomultiplier tube (SCIONIX Holland) combinations are used as the gamma detectors. The gamma-photon induced scintillation happens mainly via a fast de-excitation process with the emission of 220 nm photons from the BaF_2 scintillator [71]. The photons are coupled to PMT having a photo cathode to produce photo electrons, which are amplified by a set of dynodes and finally collected at anode to produce a fast voltage pulse. Energy discriminated signals from each constant fraction differential discriminator (CFDD) are validated using a fast coincidence unit which is used to trigger time-to-amplitude Converter (TAC) to process only true events of each annihilation process. The resulting voltage pulse from TAC is energy discriminated output as corresponding to 1274 to 511 keV. The time of arrival for each pulse is also generated via constant fraction algorithm [71] using the same CFDD units. The fast pulses from each CFDD are processed in the TAC to generate voltage pulse with amplitudes proportional to the time difference between the two gamma rays. The voltage pulses are collected and analyzed using PC based MCA (multichannel analyzer) unit, and the decay spectrum is generated. Time calibration is done to convert channel numbers to time scale using delay cables with known delay time.

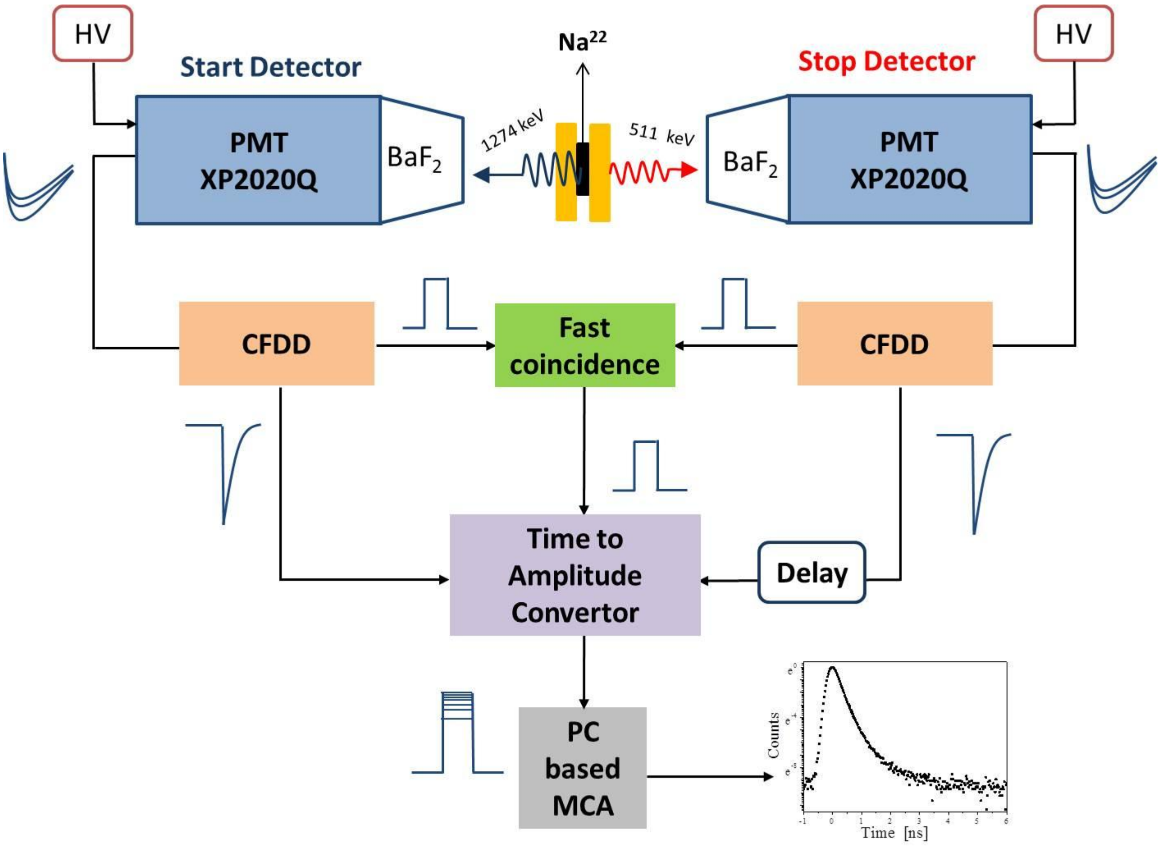

Fig. 2.8 Schematic diagram of fast-fast positron lifetime spectrometer.

The obtained decay spectrum is fitted with multiple exponential decay functions using *LT9* program [72] which takes care of Gaussian resolution function, obtained by analysing a standard reference sample, usually iron or nickel. A time resolution of~260 ps is obtained for the present experimental setup. Figure 2.9 shown measured lifetime spectrum of annealed bulk Au and fitted curve using *LT9* program.

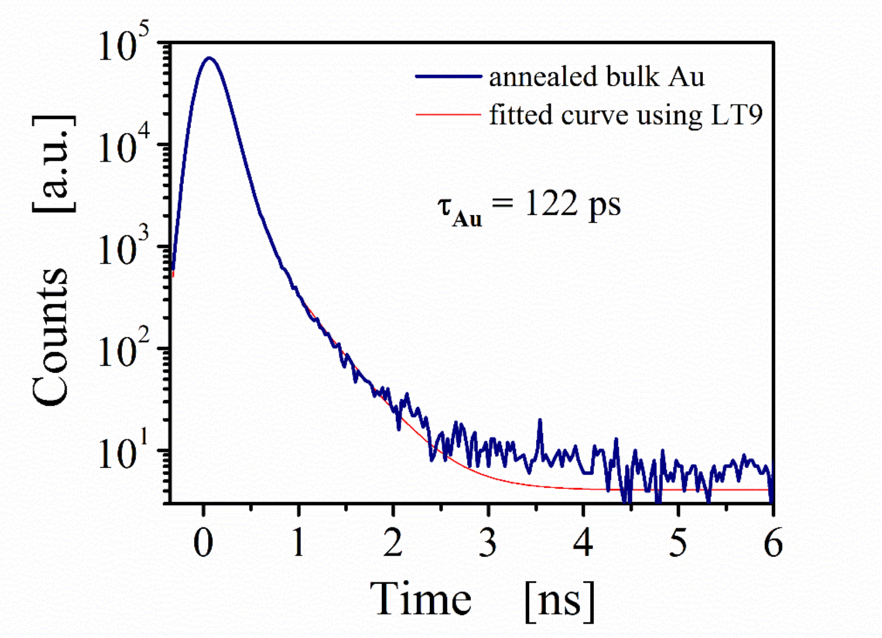

Fig. 2.9. A typical lifetime spectrum of annealed bulk Au sample.

2.4.4. Doppler Broadening Spectroscopy (DBS)

Doppler-broadening Spectroscopy is used to characterize sample based on the principle of energy and momentum conservation of annihilating electron-positron pair, resulting in emission of two gamma rays at nearly opposite direction. The frequency of the photons is shifted due to Doppler Effect. This causes a shift in the energy (or momentum) of the gamma-ray described by ΔE = $\Delta E = {}^{1}/_{2}\,(p_z c)$ where p_z is the momentum parallel to the direction of annihilation gamma, and c is the speed of light [24]. Prior to annihilation, the positrons are thermalized. Since, the momentum of the thermalized positron is much smaller than the momentum of the electron, the momentum information derived from annihilation process describes momentum of electrons. Information about the electron momentum obtained from the annihilation radiation from both bulk and defects sites can be broadly split into two major contribution viz., (1) arising from low momentum valence electrons and (2) high momentum core electrons. In defect site, the fraction of the valence of electron involved in the annihilation process increases compared with that of core electrons. The Doppler broadening spectrum is measured using high purity Germanium (HpGe) detector. The broadening in the annihilation peak was studied by line-shape parameters called S (shape or valence electron annihilation parameter) and W (wing or core electron annihilation parameter) which are defined as,

$$S = \frac{A_s}{A_t} = \frac{\int_{511-E_s}^{511+E_s} N(E)dE}{\int N(E)dE} \tag{2.14}$$

$$W = \frac{A_w}{A_t} = \frac{\int_{511-E_{w1}}^{511-E_{w1}} N(E)dE + \int_{511+E_{w2}}^{511+E_{w2}} N(E)dE}{\int N(E)dE} \tag{2.15}$$

where E_s, E_{w1}, and E_{w2} are chosen such that sensitivity of S and W to changes in defect type and concentration is optimum. The typical values are E_s = 1 keV, E_{w1} = 3 keV and E_{w2} = 5 keV. *N(E)* represents the Doppler-broadened spectrum, and thus the denominator in each expression represents total counts in the spectrum. Figure 2.10 shows a typical schematic diagram of area normalized Doppler broadening spectra. S and W parameters are highly sensitive to the open volume defects [7].

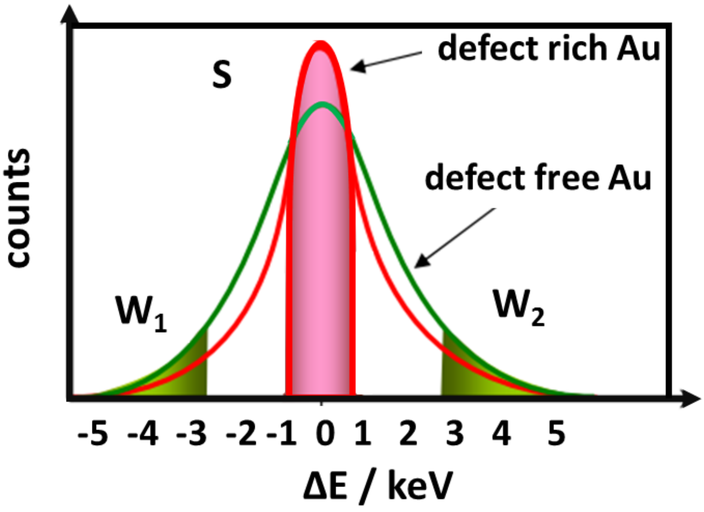

Fig. 2.10 A Doppler broadened 511 keV peak obtained, using HpGe detector, of well annealed bulk Au and as- dealloyed np- Au sample. Shaded regions represent areas used for S and W line shape parameters.

2.4.4.1. Variable low energy positron beam based Doppler broadening Spectroscopy

Apart from depth resolved S and W parameters, obtained from low energy positron beam experiments, positron diffusion length and positronium fraction, $f_{3\gamma/2\gamma}$ provides an opportunity to obtain insight of the positron behavior in thin films, irradiated materials and pore architecture of porous materials, e.g. np- Au. The endpoint energy of the positron emitted from the ^{22}Na is about 545 keV which penetrate over a depth of few hundred micrometers. To investigate defects in depth resolved manner, positron energy need to be controlled. The discovery of the negative work function for positrons shown by certain metals [73] made this possible. A thermalized positron reaching the surface of negative work function materials would be emitted from surface with energy equal to work function of these materials and this process is called as moderation. This is achieved in most of the positron beam system, worldwide by using well annealed W (100) single crystals of thickness < 1μm [74], which is having moderation efficiency of 10^{-4} to 10^{-5}. If these low energy positrons can be velocity filtered from the fast unmoderated positrons, then further control of implantation energy is possible. Figure 2.11 shows the moderated β^+ spectrum with moderating energy of 2.8 eV (negative work function of W (100)) [66,75].

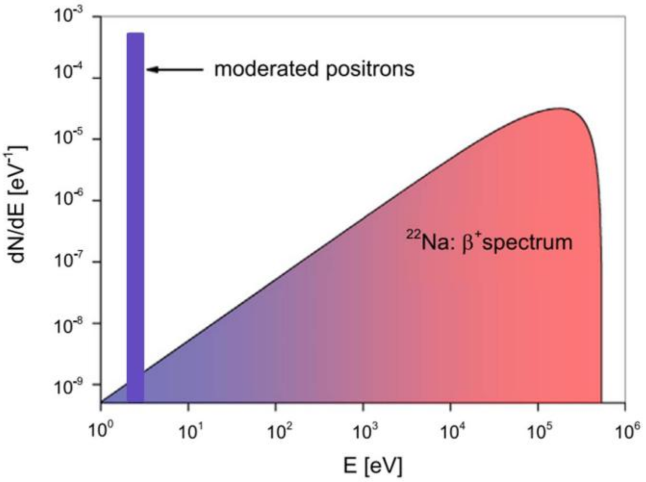

Fig. 2.11 Energy distribution curve of emitted positron from ^{22}Na and after moderation. The β+ decay spectrum reduces to a narrow curve centered at 2.8 eV after moderation in W (100) foil. (Adopted from Ref. [66])

The process of velocity control is achieved in a high vacuum system where positron fall on to the thin moderator such that many thermalized near to surface of the W (100), from where they are emitted with work function energy of ~2.8 eV. These low energy positrons are transported electrostatically into the transport region which also contains the velocity filter. The filter can be a magnetic bend or electric field – magnetic field transverse combination (E x B filter) which allows only positrons of specific energy to cross the filter [76]. The slow mono-energetic positron is separated from un-moderated fast positron by transport through 180^0 U-bend magnetic solenoid tube, whose axial magnetic field is sufficient to bend the low energy positron, while fast positron travel straight and are lost at the bend. The filtered positrons are accelerated to the required energy, which can be varied from 235 eV to 22 keV by applying a high voltage to the sample and implant them to different depths [60]. The annihilation gamma-ray spectrum was recorded using High purity Germanium (HpGe) detector having energy resolution of 1.40 keV at 662 keV gamma line of ^{137}Cs. The analysis of S and W parameters as a function of controlled positron energy provides a powerful approach to interpret the depth profiling data, especially concerning identification positron diffusion in nanoporous materials. Figure 2.12 is shown the photograph of Low energy positron beam Doppler broadening spectroscopy technique facility used in this thesis work. Figure 2.13 is shown the schematic diagram of the low energy positron beam facility.

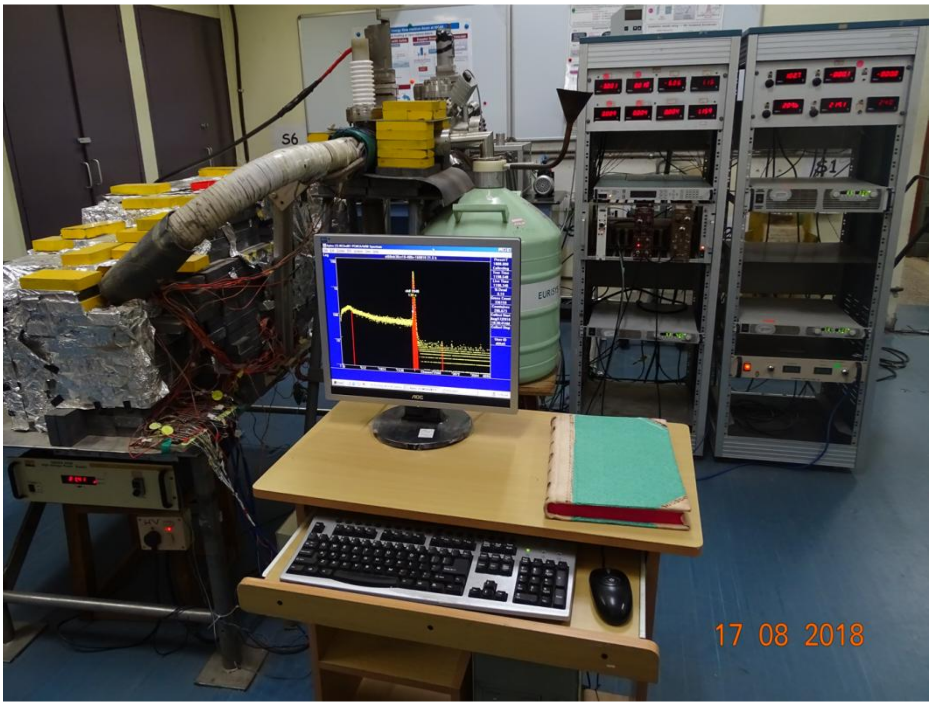

Fig. 2.12 Photograph of low energy positron beam Doppler broadening spectroscopy technique facility.

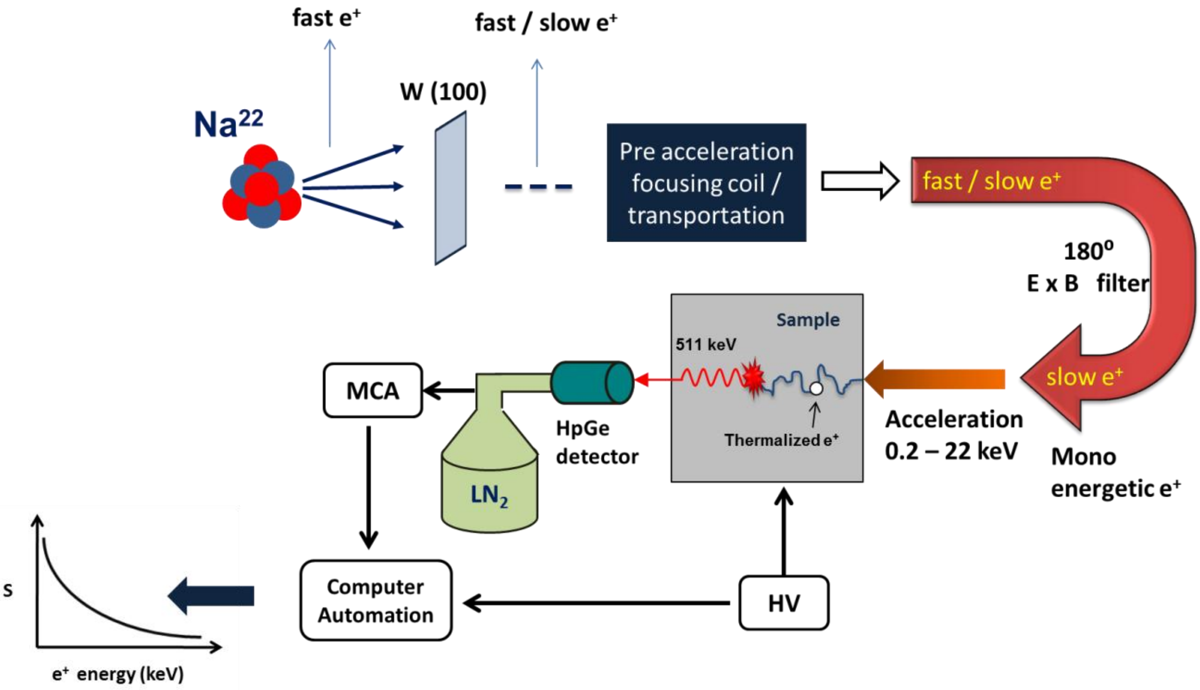

Fig. 2.13 Schematic representation of a low energy positron beam set-up using a radioactive source ^{22}Na

The experimentally observed S-parameter at a positron energy E can be approximated written as,

$$S = f_s S_s + f_d S_d + f_b S_b \tag{2.16}$$

where f_s, f_d, f_b represents fraction of positron annihilating in the surface, defected and bulk layers respectively and S_s, S_d, S_b represents S - parameter of the surface, defected and bulk layers respectively. VEPFIT code is used to fit the experimental S vs. E_p data and gives the fraction of positrons annihilating in various layers as a function of depth of the sample [77]. It involves solving positron diffusion equation taking into the account the positron implantation profile, diffusion, trapping and annihilation in the sample.

2.5. Ion implantation

Before discussing ion implantation procedure, the interactions of energetic ions with crystalline solid are briefly discussed. A schematic of ion-solid interaction is shown in Figure 2.14.

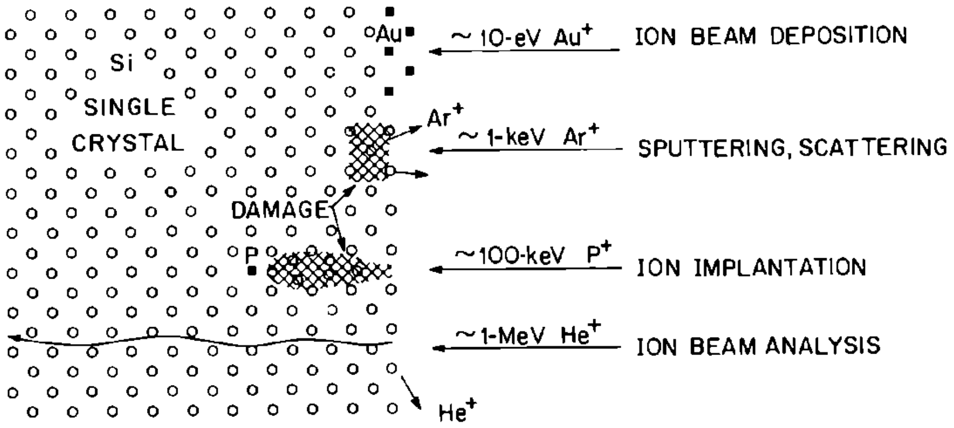

Fig. 2.14 Schematic illustration of ion beam interactions with a crystalline solid [78].

Ion-solid interactions are mainly depend on energy and mass of incident ions. Low energy ion (10-100 eV) comes to rest at surface of solids and form epitaxial layers. A 1 keV heavy ion sputters the solid surface due to large energy transfer to target. At higher energies (100-300 keV) ion comes to rest around 100 nm depth in a disordered lattice created by its passage. The 1 MeV light ions are used for ion beam analysis of solid state materials [78].

In ion implantation process, high energy ions (hundreds of keV to few MeV energy) are bombarded in to a solid using an ion accelerator which results in the introduction of desired atoms into the surface layer of a solid substrate. Ion implantation is a non-equilibrium process which is alternative method to equilibrium process of introducing dopant atoms into the lattice. Range distribution of implanted ions in substrate is approximately Gaussian in shape and they are characterized by projected range, R_p, and a straggling, ΔR_p, about this mean value, which is pictured in Figure 2.15. For simulation of ion and damage profiles, the stopping and range of ions in matter (SRIM) software is used [79].

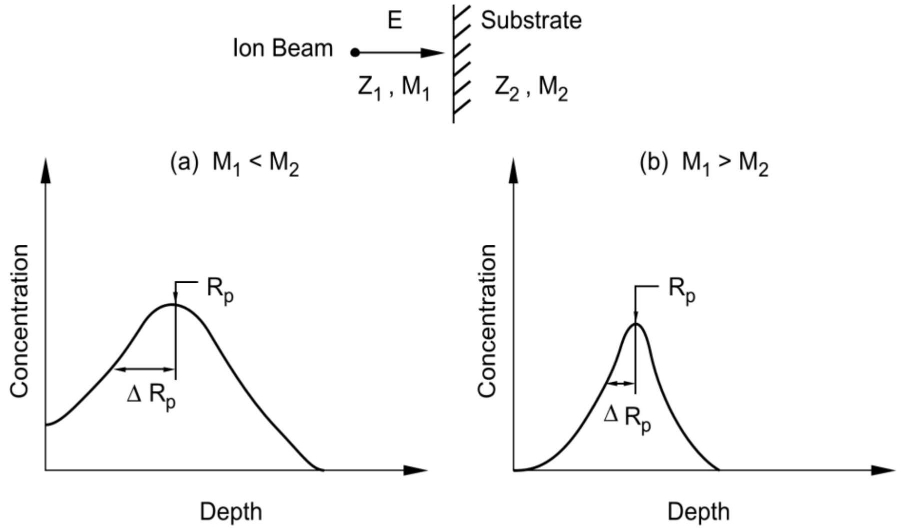

Fig. 2.15 The depth distribution of implanted atoms in an amorphous target for the cases in which the ion mass is (a) less than the mass of the substrate atoms or (b) greater than the mass of the substrate atoms. To a first approximation, the mean depth, R_p, depends on ion mass, M_1, and incident energy, E, whereas the relative width, $\Delta R_p/R_p$, of the distribution depends primarily on the ratio between ion mass and the mass of the substrate ion, M_2. (adopted from Ref. [80])

2.5.1. Accelerator used for ion implantation

In present thesis work, 1.7 MV tandetron accelerator (HVEE, The Netherlands) was used for ion implantation. Ion energy ranging from 200 keV to 15 MeV could be obtained from this accelerator depends upon charge state of the ions. The photograph and parts of the accelerator are shown in the Figure 2.16. First, negative ions of desired atomic species are produced by ion source of the accelerator. The 1.7 MV tandetron accelerator has a high brightness duoplasmatron ion source which is used for the production of H^+ or He^+ ions and a sputter ion source SNICS (Source of Negative Ions by Cesium Sputtering) for producing negative ions. The positive ion produced by the ion source is converted to negative ion by passing through a charge exchange region which is filled with lithium vapor. The ions produced in the ion source are focused by electrostatic einzel lens to the axis of the mass analyzing magnet. A high resolution magnet is used to select the required ions from the ion source and injected to the accelerating tube. The resolution (M/ΔM) of the magnet is 190.

The Cockroft – Walton type capacitive coupled parallel-fed solid state power supply is used for the generation of high voltage to the terminal (voltage from 100 kV to 1.7 MV with a voltage stability of ±100 V). The ion entering into the accelerating tube will gradually gain energy due to the applied voltage in the power supply at the middle of the accelerating column. The voltage is set,

$$V = \frac{E_{req} - E_{pre}}{1 + q} \qquad (2.17)$$

where E_{req} is the required energy, E_{pre} is the preinjection energy of the ion, q is the charge state of the ion. The accelerating tube and power supply are maintained with a base pressure of $1\text{x}10^{-7}$ mbar. The entire accelerating structure consisting of the accelerating tube, the high voltage terminal and the power supply is enclosed in a pressure vessel filled with SF_6 gas at 6 kg/cm^2 for achieving high voltage insulation.

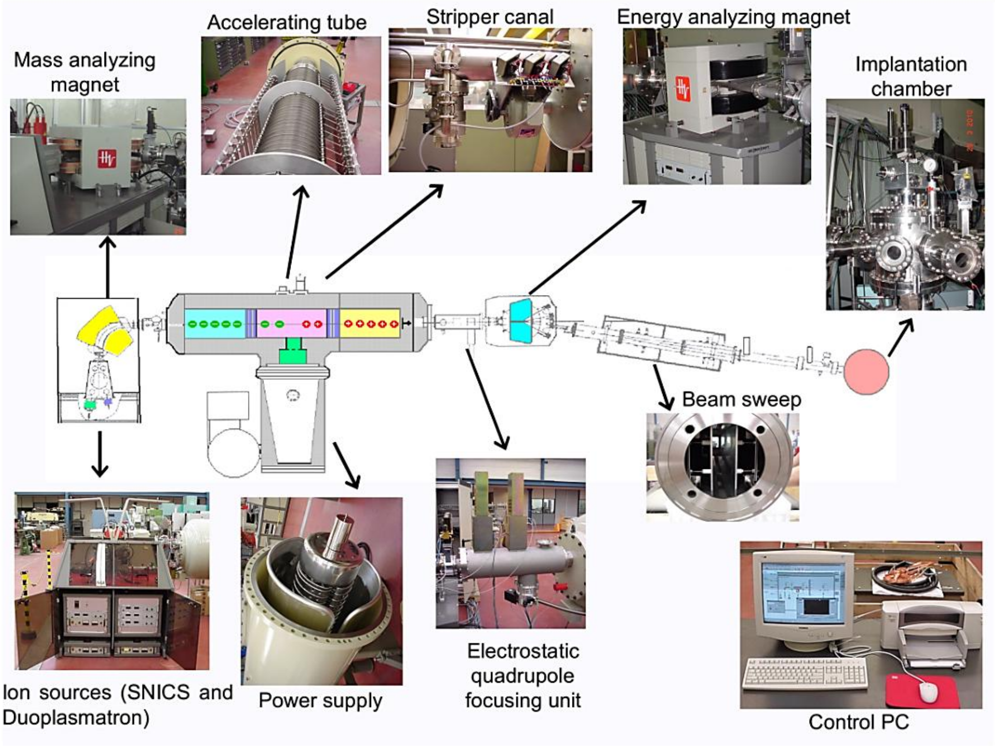

Fig. 2.16 Schematic of the 1.7 MV tandetron accelerator at IGCAR Kalpakkam and its various components.

The stripper canal present at the centre of the accelerating tube converts the negative ions into positive ions with different charge states of the ions. The charge conversion of ions takes place by interacting with the inert gas filled in this canal. A turbo molecular pump powered by a motor generator at the canal has been installed for the recirculation of the stripper gas. The ions emerging on the high energy side of the machine are focused by electrostatic quadrupole lens to the axis of the energy analyzing magnet. The high energy analyzing magnet selects the ion beam according to the energy of the ions and switches the beam to the experimental ports located at ±10º and ±30º angular positions. An implantation beam line with the beam sweep system, neutral trap, beam profile monitor and retractable slits for beam collimation has been installed at the +10º port of the switching magnet. All the controls of the accelerator are done from the PC through optical fiber cables. The number of implanted ions is given by the product of the ion flux (ion/cm^2.s) and the implantation time, t. The flux of charged particles can be measured by a current integrator, which is connected to the sample. The number of implanted ions can be calculated using the following equation,

$$N = \frac{Q}{qA} \tag{2.18}$$

where Q is the collected charge (measured by the current integrator), q is the charge state of the ion and A is the cross sectional area of ion beams.

2.6. Microstructural characterization

2.6.1. Scanning Electron Microscopy and Energy Dispersive X-ray analysis

The Field Emission Scanning Electron Microscopy (FESEM) and Energy Dispersive X-ray (EDX) analysis are the most popular imaging techniques to analyze surface morphology, elemental composition analysis [81] of np- Au samples and ligament size of np- Au using ImageJ software. In FESEM, an electron beam is generated by applying the voltage to the electron emitting filament. When the beam of electrons of energy 30 keV impinges on sample, it undergoes either elastic or inelastic scattering. The emitted electron after scattering with the energy of < 30 eV is called as secondary electrons the elastically scattered electrons with angle > 90º are referred as back scattered electrons. The secondary and backscattered electrons are carrying information of z-contrast, topography, and composition of np- Au. Heavy element (Au) backscatter electrons more strongly than less heavy element (Ag) from the master alloy $Ag_{75}Au_{25}$ and this can be useful to distinguish different chemical phases. The resolution of FESEM is few nm, where magnification can be varied from 10 to 400 kX. Inelastic scattering of electron beam by sample in SEM system is utilized in elemental characterization. High energy electrons can knock of core shell electrons by inelastic energy transfer, which result in characteristic X-ray emission from elements present in the sample. These X-rays are detected using semiconductor detector. Energy dispersive analysis of X-rays (EDX) yields quantitative information about elements present. In the present thesis, FESEM

(SUPRA 55, Zeiss) was used to examine the morphology and structure of np- Au and EDX (FEI Helios Nanolab 600i) was used to examine elemental analysis of np- Au samples.

2.6.2. Transmission Electron Microscopy

Transmission electron microscopy is a versatile and indispensible tool in the study of material due to its high spatial resolution. In TEM, the image is formed by electrons passing through the sample. The principle of operation almost same as that of an optical microscope. However, TEM has magnification and resolution capabilities that are over a thousand times beyond that offered by the optical microscope. TEM is able to analyze the morphology, localized crystal structure and defect structure with high spatial resolution leading to an understanding of material property.

When an electron is accelerated from an electron gun with a high voltage of range 100-400 kV towards a thin specimen, it will be unscattered (transmitted through specimen), elastically scattered (diffracted by specimen) and inelastically scattered by the specimen in which specimen loaded in the Copper grid. The diffracted electrons follow the Bragg's law

$$d = n\lambda/2sin\theta \qquad (2.19)$$

where d being atomic spacing, θ being the angle of incidence, λ being the wavelength of incident electron and n is the integer. Selected area electron diffraction (SAED) pattern achieved by selecting the diffracted beam from a selected area on the specimen which is similar to X-ray diffraction [82]. The major components of the TEM can be categorized into the illumination system, the objective lens/stage, and the imaging system. By adjusting these three systems and selecting the appropriate scattered electron beams from the specimen, several types of TEM images can be obtained which includes, bright and dark field images, SAED pattern, high resolution (HRTEM) images and Fast

Fourier Transform (FFT) images. The schematic diagram explains the function of this system in Figure 2.17.

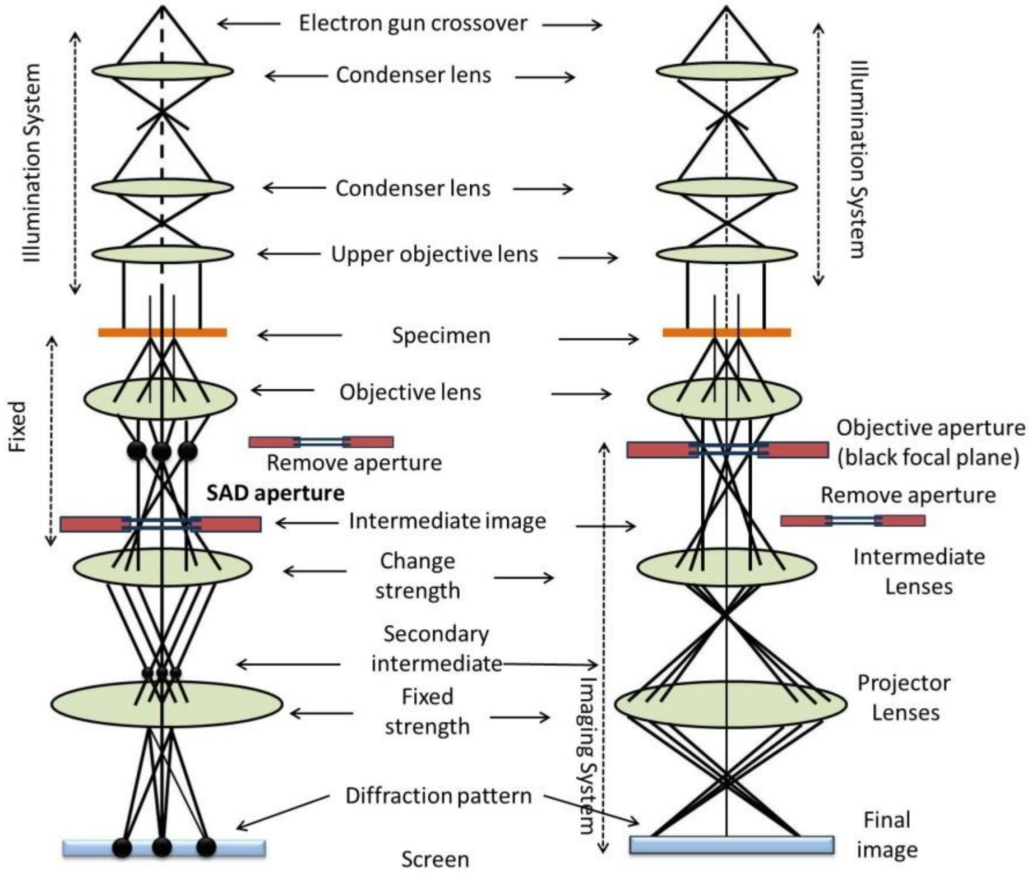

Fig. 2.17. A ray diagram of TEM showing the diffraction mode operation (left side) and standard imaging mode operation (right side) with major components of the system.

High-resolution transmission electron microscope (HR TEM) studies on np- Au samples were carried out with HR TEM (LIBRA 200FE Zeiss) operated at accelerating voltage of 200 kV to provide compositional and crystallographic information.

2.6.3. Electron Energy-Loss Spectroscopy

The electron energy-loss spectroscopy (EELS) measurement based on the energy distribution of transmitted electron through the specimen due to inelastic scattering [83]. It is a very sensitive technique for low atomic elements ($Z \leq 10$). The inelastic scattering of an incident electron leads to several interactions in the specimen such as inter- and intra-band transitions, plasma interactions, ionization, ionization of core-shell electrons

(K, L, M, N) and plural scattering. In order to obtain the characteristic energy-loss of incident electrons the transmitted electron beam is directed towards a high-resolution electron spectrometer, shown in schematic Figure 2.18

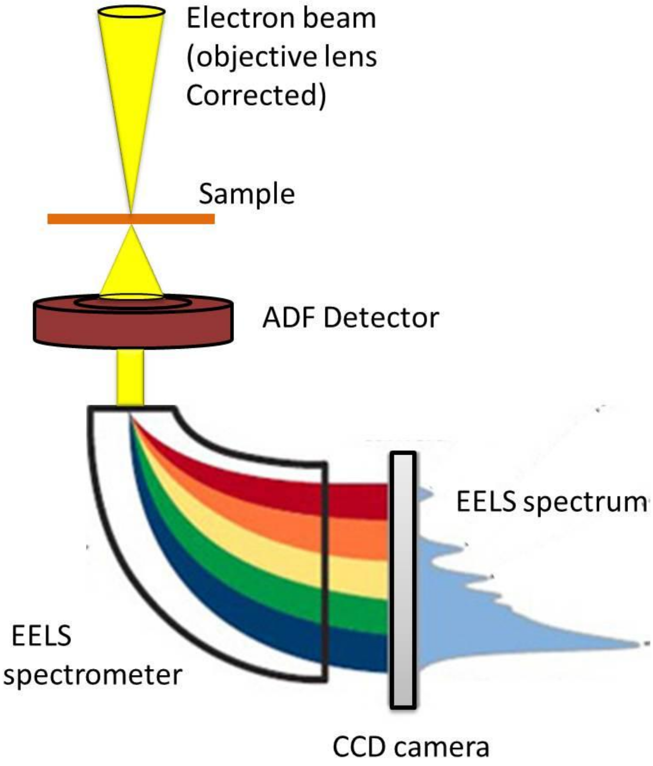

Fig. 2.18 A schematic diagram of a TEM-EELS system having in-column second order corrected omega energy filter.

. EELS spectra consist of zero loss peak (due to the elastically scattered electron), low energy-loss peak (due to plasmon transitions within valence band and stimulated collective oscillation of electron sea field), and high energy-loss peak (due to the inner shell ionization). EELS studies carried out using a HR TEM (LIBRA 200FE Zeiss) with 200 kV and in-column second order corrected omega energy filter type spectrometer with an energy resolution of 0.7 eV.

2.7. Mechanical property studies

2.7.1. Nanoindentation

The mechanical behavior of 3D interconnected metallic porous materials differs from their bulk counterpart due to the complex structure [84]. In this thesis, nanoindentation hardness measurements were carried out using ultra nanoindenter with Berkovich tip (size 30 – 50 nm), which has the shape of a three-sided pyramid [85]. Although nanoporous materials are fragile and weak in macroscopic scale, the hardness of the nanoporous material is found to be high due to the dense connectivity and small ligament size. Nanoindentation is used for measuring mechanical properties such as hardness and Young's modulus at a nanoscale level. This leads to the application of nanoindentation to extract the mechanical properties of nanoscale specimens; such as thin film, single grain and irradiated samples. Whereas classic indentation methods such as Vickers, Brinell, and Rockwell use loads in the hundreds of newton, nanoindentation uses load of 0.2 – 100 mN. The nanoindentation technique is based on the mechanism of simple hardness testing, where the probing indenter on the material is loaded into the material. The used load P_{max} together with the contact area between indenter and sample, A_c, is then used to calculate the hardness of the material.

$$H = \frac{P_{max}}{A_c} \tag{2.20}$$

The load (P) and indentation displacement (h) are measured during both loading and unloading cycles shown in Figure 2.19. There are three important quantities that must be measured from the load-displacement curves (P-h curves). The maximum load (P_{max}), maximum displacement (h_{max}), and Stiffness ($S = dP/dh$), equaling the slope of the upper portion of the unloading curve are determined. The loading is the mixture of elastic and plastic process, and the unloading is an elastic recovery process, so Young's modulus can be calculated from the unloading curve.

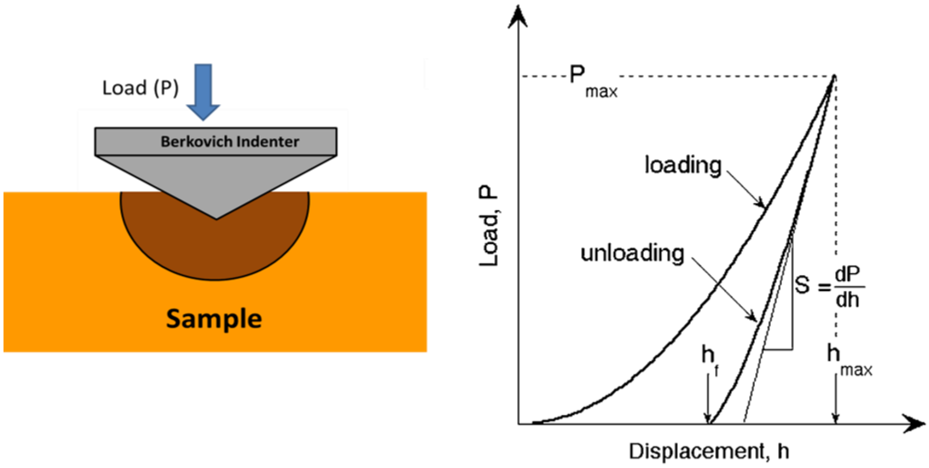

Fig. 2.19 a) A schematic diagram of nanoindenter loading on sample and corresponding affected plastic zone of the sample. b) Schematic illustration of indentation load – displacement data of indentation parameters.

2.7.2. Oliver-Pharr method

Determination of contact area between indenter and sample makes the difference between conventional hardness testing and nanohardness testing. In conventional method, the contact area is calculated from direct measurement of residual impression of the indenter and this is not possible with nanoindentation where the intented area is very small to be measured accurately. To overcome this, we have used known indenter geometry and corresponding contact area can be calculated by Oliver-Pharr method [86]. Figure 2.20 shows a typical load-displacement curve recorded during experiment. During unloading of the indenter, the elastic displacement recovers and the final indentation depth h_f remains as shown in Figure 2.20.

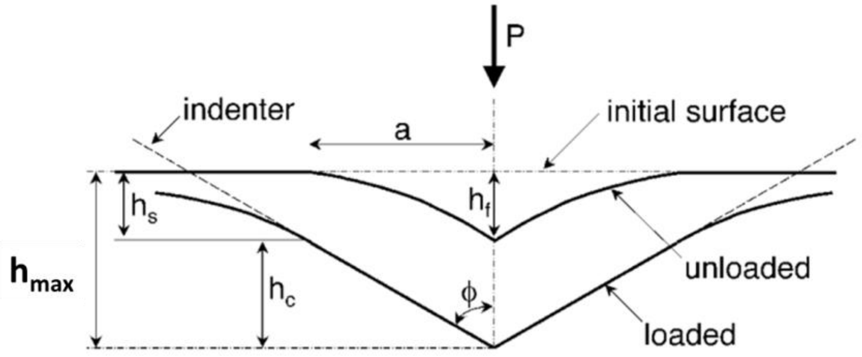

Fig. 2.20 Schematic illustration of the unloading process showing parameters characterizing the contact geometry (adopted from Ref. [106])

Determination of hardness and Young's modulus from the indentation experiments as proposed by Oliver-Pharr method to obtain the contact area A_c for calculating hardness using equation (2.20), it is essential to calculate the contact depth, h_c,

$$h_c = h_{max} - h_s \tag{2.21}$$

where h_{max} is the maximum displacement, h_s is the displacement of the surface at the perimeter of the contact as shown in Figure 2.20. The h_s depend on the indenter geometry and can be determined using Sneddon's elastic contact theory

$$h_s = \varepsilon \frac{P_{max}}{S} \tag{2.22}$$

where ε is a geometric constant which depends on the indenter geometry (for a Berkovich indenter = 0.75) and S is the contact stiffness which is obtained from load-displacement curve. Using equation (2.22) to approximate the vertical displacement of the contact periphery, h_c is determined as,

$$h_c = h_{max} - \varepsilon \frac{P_{max}}{S} \tag{2.23}$$

The contact area is obtained from the area function, also sometimes called the indenter shape function,

$$A_c = F(h_c) \tag{2.24}$$

Then hardness is estimated from equation (2.20).

Determination of elastic modulus follows from its relationship to contact area and the measured unloading stiffness through the relation,

$$S = \beta \frac{2}{\sqrt{\pi}} E_{\mathrm{eff}} \sqrt{A_c} \tag{2.25}$$

Where E_{eff} is the effective elastic modulus defined by,

$$\frac{1}{E_{eff}} = \frac{1-\upsilon^2}{E} + \frac{1-\upsilon_i^2}{E_i} \qquad (2.26)$$

The effective elastic modulus takes into account the fact that elastic displacement occur in both the specimen with Young’s modulus E and Poisson’s ratio υ and the indenter with elastic constants E_i and υ_i.

Chapter 3

Development of nanoporous metallic materials

Chapter 3 discusses the synthesis and microstructure results of nanoporous Au (np- Au). The experimental methodology involved in the synthesis of np- Au using electrochemical dealloying method will be discussed in the beginning of this chapter. The later part of this chapter describes the microstructure results obtained on np- Au in three different pre-conditioned stages such as as- dealloyed, oxide covered and reduced clean metallic states. Electrochemical measurements combined with high resolution transmission electron microscopy studies have been used to follow the microstructure changes in np- Au subjected to electro-oxidation and oxygen reduction reactions.

3.1. Introduction

The purpose of the present chapter is to synthesize np- Au and to study the microstructure and chemical information in nanoporous Au towards electro-oxidation (initial stages of oxidation and oxide formation) and oxygen reduction in aqueous medium. This proposed study is substantiated based on the fact that the electrochemical charging/discharging behavior and the manifestation of potential dependent changes at the electrode surface depend, in many cases, on whether the electrode-electrolyte interface is polarized positively or negatively with respect to the potential of zero charge (pzc) [4,87,88]. For instance, when the potential applied to the electrode is around the pzc where the specific adsorption based interaction between the electrode surface and the ions in the electrolyte remains absent or relatively weak, then, the net charge transfer across the electrode - electrolyte interface depends mainly upon the electrostatic force mediated ion mobility at the electrode surface. This renders the double layer interface formed on the specific adsorption free electrode surface to be capacitive [89,90]. The electrode-electrolyte interface structure behaves as pseudo-capacitive in potentials between onset of electro-oxidation and onset of oxide formation. In the pseudo-capacitive region, the potential controlled charge dipoles in place at the electrode surfaces [32,91]. Due to such an in-separable combination of charge transfer resistive components formed by redox process in association with capacitive double layer charging, the pseudo-capacitive to ideal capacitive electrode-electrolyte interface structure can be obtained by sweeping the applied electrode potentials from the oxidation region towards cathodic reduction region through the pzc. Unlike the process of initial stage of electro-oxidation as mentioned, in cases where the end potential applied to the electrode in anodic direction is more positive than the pseudo-capacitive potential intervals, apart from intrinsic electrochemical oxidation process, metal oxide layers in specific stoichiometry develop at the electrode surfaces [92] and the oxide formation process occurs can be described by the model of oxide growth [93].

Conway [4] provides an overview of the state of art in electro-oxidation/reduction studies on different electrode surfaces, including Au (111). Angerstein-Kozlowska et al., [94] reported on Au that transformation to Au oxide takes place along multiple charge transfer reaction steps viz., double layer charging, surface oxidation to place exchanged Au hydrous oxide and oxide layer formation in the anodic scan direction and their resulting oxygen reduction reactions and double layer discharging to Au in the cathodic scans. In addition to the current understanding of the np- Au/1M $HClO_4$ through electrochemical characterization, several recent articles have reported np- Au catalyst for oxidation reactions. Liu et al., [28] have studied np- Au using the high-angle annular dark-field scanning tunneling electron microscopy and reported that weakly-coordinated

Au surface atoms residing at the ligament surfaces contribute intrinsically to serve np- Au as a catalyst. In line with discussion on intrinsic microstructure variations in np- Au to the catalytic properties, Zugic et al., [29] has demonstrated, based on the in-situ electron microscopy studies that the variation of oxygen-Au stoichiometry and the atomic restructuring effect influence directly to different catalytic reactions, especially for selective alcohol oxidations. Even though majority of the reports suggest structural changes and surface composition in np- Au give rise to catalytic activity, important microstructure that drive np- Au for various catalytic oxidation reactions are not well understood. Detailed microstructure investigations on np- Au under various electrochemical pre-conditions and in-situ monitoring of the changes at the ligament/pore surface in contact to the electrolyte in selected potential intervals are therefore important to explore the reasoning for the existence of catalytic activity in np- Au.

Electrochemical treatment on np- Au in $HClO_4$ solution would be of particular interest since the changes that occur at the Au ligament – electrolyte interface induced by the initial stage of oxidation, oxide formation and oxygen reduction processes can be clearly distinguished. Electrochemical characterization using cyclic voltammetry and impedance spectroscopy studies have been carried out to shed insights on the changes at the np- Au/1M $HClO_4$ interface. Microstructure analysis was carried out on the electrochemical pre-treated np- Au samples ex-situ using high resolution transmission electron microscopy (HRTEM) coupled with electron energy-loss spectroscopy (EELS) to achieve the objective.

3.2. Experimental methods

3.2.1. Preparation of $Ag_{75}Au_{25}$ binary alloy for dealloying Experiments

Arc melted polycrystalline alloy ingots with nominal composition $Ag_{75}Au_{25}$ was used for dealloying experiments. The master alloy specimens were prepared using the starting high pure elemental materials Ag (99.99%) and Au (99.99%) obtained from Alfa Aesar®. The arc melted alloy pieces were heat treated in vacuum-sealed quartz ampoules at 800°C for 20 hrs for homogenization of the alloy composition. This ingot was cold-rolled into shape to disc form with dimensions of 1.5 cm diameter and 0.2 cm thickness using standard mechanical roller machine. Discs obtained from these samples were annealed at 700°C in high vacuum (10^{-6} mbar) to remove the cold work induced defects. The results obtained from the Energy-dispersive X-ray spectroscopy (EDX-ray) measurements are shown in Figure 3.1. Figure 3.1 a) shows the selected SEM image of $Ag_{75}Au_{25}$ binary alloy in which the elemental point analysis has been performed. The typical EDX spectrum collected during this analysis is shown in Figure 3.1.b). Quantitative analysis of this energy spectrum indicate that the chemical composition obtained at various locations is $Ag_{75}Au_{25}$ (at.%) within ~ 1% deviation.

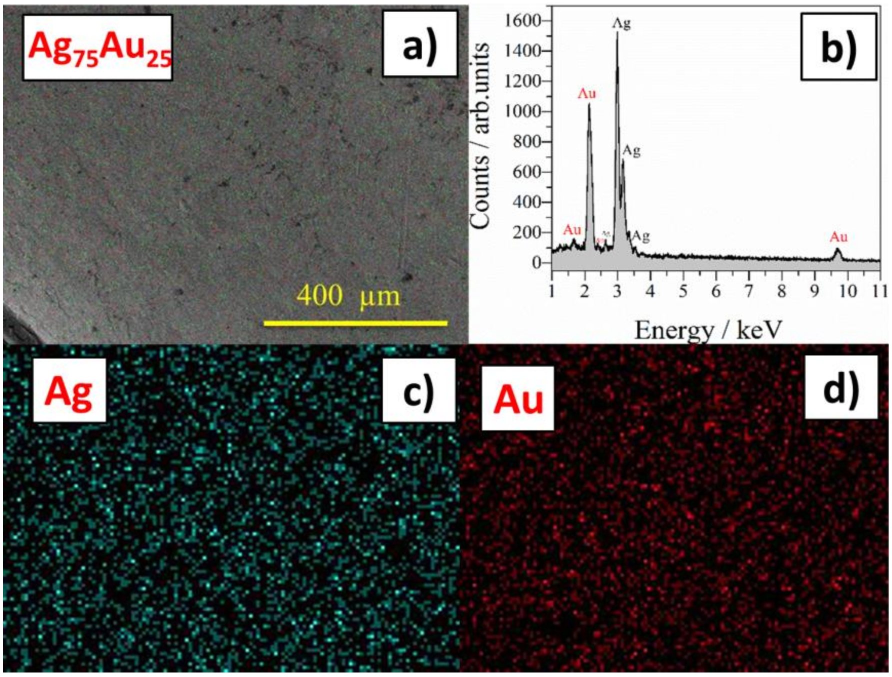

Fig. 3.1 EDX-ray elemental point analysis of $Ag_{75}Au_{25}$ alloy. a) Compositional elemental point analysis characterization using EDX spectroscopy of master alloy $Ag_{75}Au_{25}$. b) Typical energy spectrum collected during EDX-ray point analysis. c) and d) Full-scan elemental mapping showing the spatial distribution of elements Ag and Au present in the $Ag_{75}Au_{25}$ alloy used for the dealloying experiments.

3.2.2. Synthesis of nanoporous Au using electrochemical dealloying method

Electrochemical Dealloying experiments were performed on well annealed disc of $Ag_{75}Au_{25}$ electrodes in a glass electrochemical cell by applying a constant potential of 0.8 V versus pseudo Ag/AgCl reference electrode in 1M $HClO_4$ electrolyte. Figure 3.2 illustrates the electrochemical cell configuration before and after the dealloying of $Ag_{75}Au_{25}$. Noticeable changes were observed in the cell during the dealloying process. The most important observation was the change in color of the dealloyed sample after Ag gets dissolved. The dealloyed sample turns into brownish black from the original silvery color of master alloy. The dealloyed samples could be easily removed from the cell. The nanoporous Au samples were cleaned with 18 MΩ ultrapure water and used for further experiment. Figure 3.3 a) shows photographic image of master alloy $Ag_{75}Au_{25}$ disc prior to dealloying and np- Au powders after dealloying and microstructural and elemental characterization are shown in Figure 3.3 b-d).

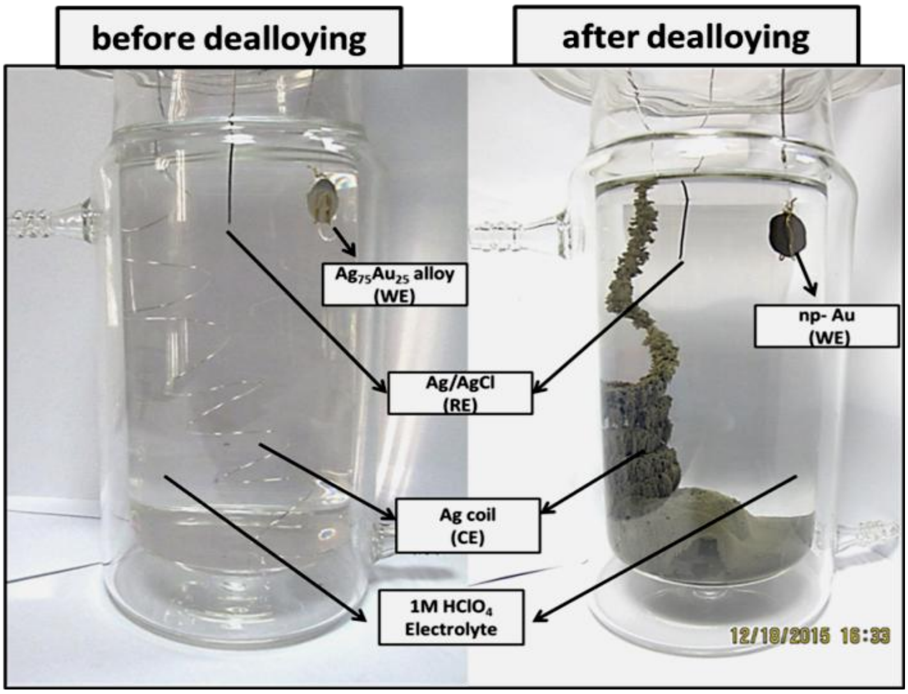

Fig. 3.2 Fabrication details of nanoporous Au. The figure shows the photograph of electrochemical cell, prior to dealloying process (left side) and after completion of dealloying process (right side)

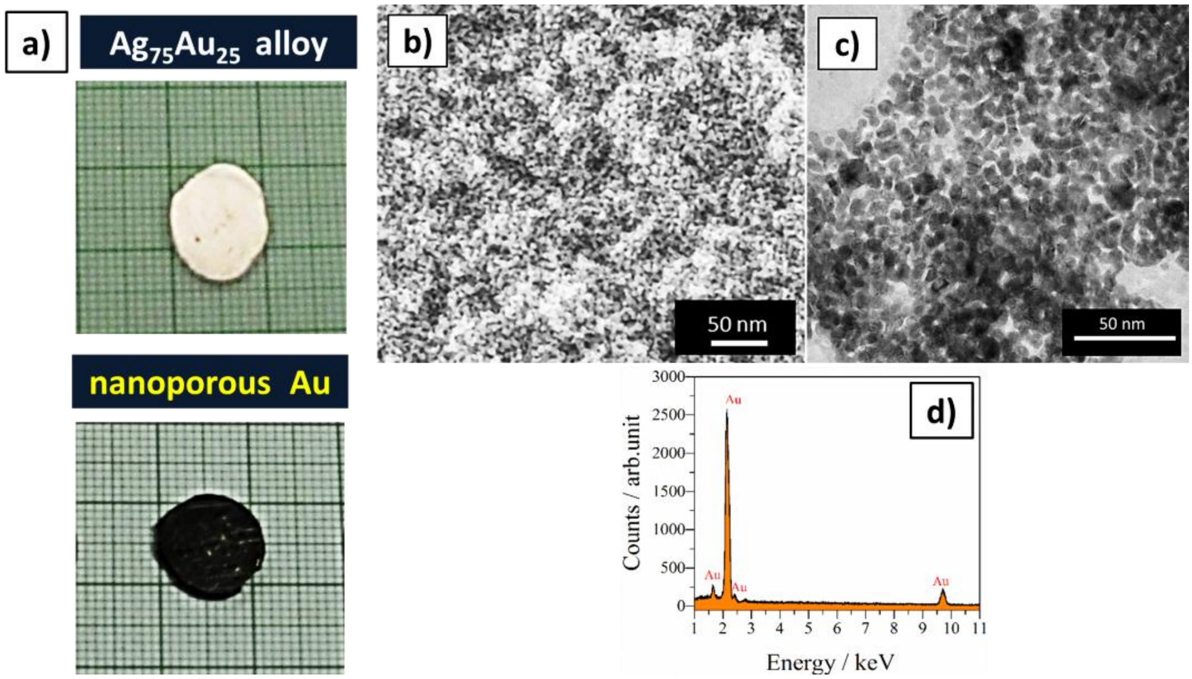

Fig. 3.3 a) Photographic images of master alloy $Ag_{75}Au_{25}$ disc prior to dealloying and np- Au disc after dealloying. b) A typical scanning electron micrograph image (fracture surface) and c) HRTEM image of np- Au powders after dealloying in 1M $HClO_4$ electrolyte. d) Typical EDX-ray of np- Au confirming the removal of Ag below the detectable limit of EDX.

3.2.3. Microstructure studies of np- Au

Nanoporous Au specimens required for microstructure studies have been prepared according to the experimental procedure as described below. In brief, arc melted $Ag_{75}Au_{25}$ alloy fine debris specimens were dealloyed in 1M $HClO_4$ electrolyte at 298 K by applying a potential of 0.80 V versus Ag/AgCl reference electrode and silver coil served as auxiliary (counter) electrode as shown schematically in Figure 3.4. The selective dissolution of Ag from the $Ag_{75}Au_{25}$ alloy led to formation of Au sponge with interpenetrating ligaments and continuous pores of dimensions ~ 5 nm. A commercial potentiostat (PGSTAT 302N, Metrohm Autolab e.v.) was used for the dealloying and subsequent electrochemical experiments. Hence prior to study the initial stage of electro-oxidation in np- Au, the as- dealloyed np- Au in $HClO_4$ electrolyte were electrochemically reduced by potential cycling in a wider intervals viz., $-0.3 < E < 1.05$ V successively till to achieve the characteristic cyclic voltammetry behavior of Au [4,32].

The procedure followed for the reduction of as- dealloyed np- Au is described in details in Chapter 4. In order to create oxide layer on the Au ligament surfaces, the as dealloyed np- Au samples were used directly.

The ultra-fine debris collected from the as-dealloyed, oxide formed and reduced (oxygen desorbed) np- Au were dispersed onto Cu grids coated with ultra-thin carbon films and studied in a high resolution transmission electron microscope (LIBRA 200FE Zeiss) operated at an accelerating voltage of 200 kV to explore their microstructure features. Analyses have also been carried out in selected regions in the high resolution TEM images using electron energy-loss spectroscopy EELS to access the oxygen contents in different electrochemical pre-conditioned np- Au.

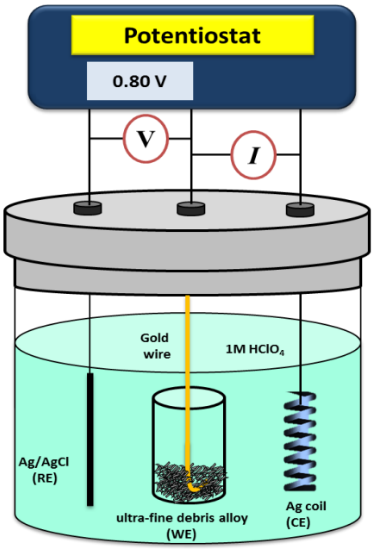

Fig. 3.4 Schematic view of electrochemical cell in three-electrode configuration used for preparing np- Au samples for TEM measurements. The ultra-fine $Ag_{75}Au_{25}$ alloy powders, Ag coil and Ag/AgCl wire served in the cell as working, counter and reference electrodes.

3.3. Results and discussion

3.3.1. Electrochemical behavior in np- Au: Effects on Microstructure

3.3.1.1. Initial stage of oxidation in np- Au

Figure 3.5 shows the cyclic voltammetry (CV) scans for reduced np- Au in 1M $HClO_4$ recorded at scan rate of 1 mVs^{-1} in the temperature interval $298 \leq T \leq 368$ K. It is seen that the features corresponding to initial stages of electrochemical oxidation develop at potentials positive to the small constant current flow region in the anodic scan where double layer charge prevails dominantly at the np- Au/1M $HClO_4$ interface. The noticeable features present are three successive current peaks at potentials E_{P1} ~ 0.93 V, E_{P2} ~ 1.0 V and E_{P3} ~ 1.04 V. It is safely assumed that these three current peaks in order present in the positive anodic potentials are qualitatively similar to those reported on (100), (110), (111) oriented single crystal Au surfaces [94,95].

First, the three oxidation peak plateaus E_{P1}, E_{P2} and E_{P3} present in the anodic part of the cyclic voltammetry scans of reduced np - Au as depicted in Figure 3.5 a) will be discussed. Results from the analysis of the voltammetry scans and based on the literature reports, it is considered that the overall appearance of the three peak plateaus in the voltammetry scans of Figure 3.5 is due to the adsorption of oxygen containing ads-species in the electrolyte on three different atomically co-ordinated sites on Au ligament/pore surfaces. A closer look at the voltammetry scans of Figure 3.5 a) reveals that the oxidation current under the peak plateaus E_{P1}, E_{P2} and E_{P3} is significantly affected with cell temperature. It is seen that as the cell temperature increases, the current density under the peak plateau E_{P1} and E_{P2} decreases, whereas that corresponds to the peak plateau E_{P3} shows an increasing trend. Importantly, at 363 K, the oxidation peak plateau E_{P3} present at 1.04 V becomes high intense and sharper. From the above results, it can be undoubtedly inferred that the changes in the current density under the peaks E_{P1}, E_{P2} and E_{P3} with temperature can be attributed to the creation of certain kinds of diffusion controlled atomic rearrangements at the np- Au/1M $HClO_4$ interface. For a better understanding of the changes in the current variations under the peak plateaus E_{P1}, E_{P2} and E_{P3} with temperature, the net charge transferred across the Au ligaments in reduced np - Au were quantified from the CV scans of Figure 3.5 a). The results are summarized in Figure 3.5 b), and c). The decreasing trend in the δQ value with the increase in cell temperature can be understood in terms of ligament coarsening in reduced np- Au [96–98].

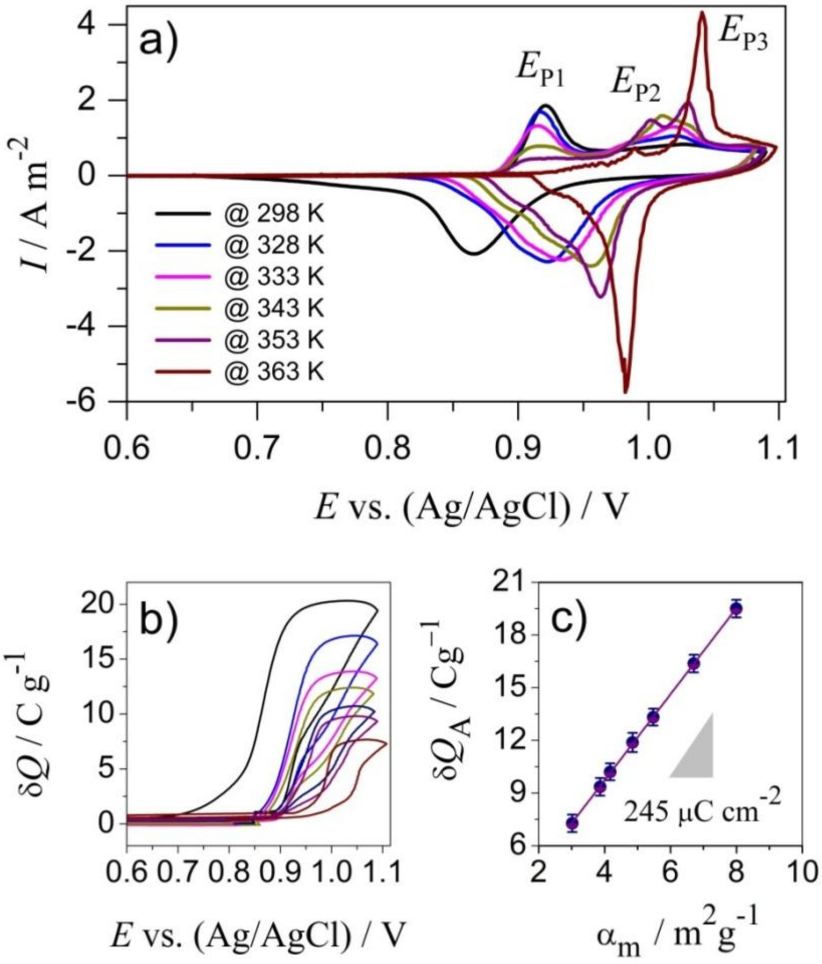

Fig. 3.5 a) Results of cyclic voltammetry measurements for reduced np- Au in 1M $HClO_4$ electrolyte in the initial stage of electro-oxidation potentials. The figure shows a series of cyclic voltammetry curves recorded at 298, 328, 333, 343, 353, 363 K. at a scan rate of 1 mV/s. b) Net charge transferred δQ in reduced clean np- Au with electrode potential E, evaluated from temperature dependent variations in the cyclic voltammetry curves depicted in sub figure (a). c) Plot of δQ versus specific surface area α_m of reduced np- Au. Mass of the sample used: 10.4 mg. It may be noted that Ag/AgCl reference electrode used here had a shift of - 198 mV with respect to the standard hydrogen electrode.

Ligament coarsening in np- Au with temperature is rather conspicuous. Therefore, it is worthwhile to use δQ versus temperature results to compute the net charge required for the adsorption of oxygen bearing ads-species on the ligament surface in reduced np -

Au. For this purpose the δQ value in C g^{-1} is plotted as a function of their specific surface area α_m in m^2 g^{-1} which is shown in Figure 3.5 c). The slope of the δQ versus α_m plot obtained from the linear regression analysis is a measure of surface charge density $\delta\sigma$ [20]. It gives 245 μC cm^{-2}. To verify the significance of the surface charge density $\delta\sigma$ results and to identify the microscopic processes involved in the evolution of the three current peaks in the anodic scans (cf. Figure 3.5 a)), the surface charge density results reported previously on bulk Au were examined. Kozlowska et al., [94] from their voltammetry studies on Au (111) in $HClO_4$ reported a surface charge density value of 222 μC cm^{-2} for a coverage of one monolayer of oxygen bearing ads-species on Au by a charge transfer of 1 e^-/Au surface atom. The excellent agreement of data between the present study and the literature report emphasizes that the physical reason for the pronounced three current peak plateaus appeared in the anodic scans of Figure 3.5 a) corresponds to the adsorption of oxygen containing ads-species on three energetically favorable Au crystal planes on the ligament/pore surfaces [99]. Concurrent with the presence of different energetic atomic sites interfaced with two-dimensionally co-ordinated oxygen ads-species at the np- Au/1M $HClO_4$ interface, one can be confident to summarize that the one electron charge transfer reaction,

$$Au + H_2O \leftrightarrow (Au - OH) + H^+ + e^- \qquad (3.1)$$

occurred during the initial stage of electro-oxidation process is surface specific and depends highly on the details of atomic structure of Au ligament surfaces in contact to the electrolyte. This one electron charge transfer reaction persists on ligament surfaces in np-Au is consistent with the microscopic model proposed by Conway [4] and Jerkiewicz et al., [92] for metal surfaces in aqueous electrolytes.

3.3.1.2. Oxide formation in np- Au

Now we inspect the voltammetry features evolved in as- dealloyed Au/1M $HClO_4$ during oxide formation reactions. The CV spectra recorded in two selected potential intervals, 1.1 < E < 1.3 V and 1.1 < E< 1.7 V, are depicted in Figure 3.6 a). In these CV scans, the lower vertex potential was fixed to 1.1 V for preventing the oxygen reduction reaction,

$$(Au - OH) + H^{+} + e^{-} \leftrightarrow Au + H_2O \qquad (3.2)$$

As shown in the CVs in Figure 3.6 a), there is almost a constant current flow region between 1.1 and 1.3 V. It points to the persistence of pseudo-capacitive double layer structure at the ligament surfaces in as- dealloyed np- Au. This observation is consistent with the previously reported results on positively charged np- Au where the current flow across the electropositive Au ligament surfaces are symmetric in terms of charge balance in the anodic and in the cathodic scans [20,100]. It is seen from the CVs in Figure 3.6 a) that there is an upsurge in the current flow above 1.1 V. This pronounced rising edge of the current wave in the positive anodic potential sweep is a clear indication that oxide formation reactions occur in as- dealloyed np - Au above 1.1 V. It should be noted that we restrict the anodic upper vertex potential to 1.7 V to avoid vigorous steady state gas evolution.

To get further insights about the oxide formation behavior, CV measurements were carried out in the potential interval 1.1 < E < 1.7 V at elevated temperatures. Four hundred voltammetry transient curves were recorded. Of all the four hundred CV scans, the first 55 scans were recorded at 273 K and the remaining scans were recorded at 343 K. In order not to obscure the plot, ten voltammetry curves (scans 10, 20, 25, 45, 55, 70, 110, 155, 235 and 400) are depicted in Figure 3.6 b). Subsequent to the completion of each CV run as shown in Figure 3.6 b), electrochemical impedance spectra were recorded at 1.15 V to find the nature of oxide formed region at the np - Au/1M $HClO_4$ interface. Figure 3.6 c) shows the Nyquist plots obtained for the oxide formed np- Au in 1M $HClO_4$. On the analysis of the impedance spectra using electronic models, it is found that the impedance spectral features of as- dealloyed np- Au /1M $HClO_4$ change during the repeated cyclic voltammetry scans. For example, a single semicircle and a loop appeared in the Nyquist plots after the lapse of 55 cyclic voltammetry scans. The appearance of the loop at lower frequencies is attributed to the presence of inductive behavior caused by the distorted nature of the electrode surface in contact with the electrolyte [101,102]. It is seen that the diameter of the single semicircle corresponding to oxide formation resistance R_{Ox} increases gradually with repeated CV scans. To get an idea about the variation of R_{Ox} with potential cycling, the R_{Ox} value obtained from the analysis of the impedance spectra in Figure 3.6 c), is plotted as a function of the scan number N_{Ox}, as shown in Figure 3.6 d). An increasing trend of R_{Ox} value with N_{Ox} is found. The voltammetry and the impedance results as discussed reveal that the pseudo capacitive electrochemical interface structure formed originally in positively charged as- dealloyed np- Au /$HClO_4$ has transformed into a resistance dominant electrochemical interface structure during the formation of oxide layer in np- Au. This subtle variation in the resistance value R_{Ox} with pre-cyclic voltammetry scans N_{Ox} is a clear indication that oxide growth kinetics at the ligament/pore surface in oxide formed np- Au/1M $HClO_4$ interface increases with measurement time.

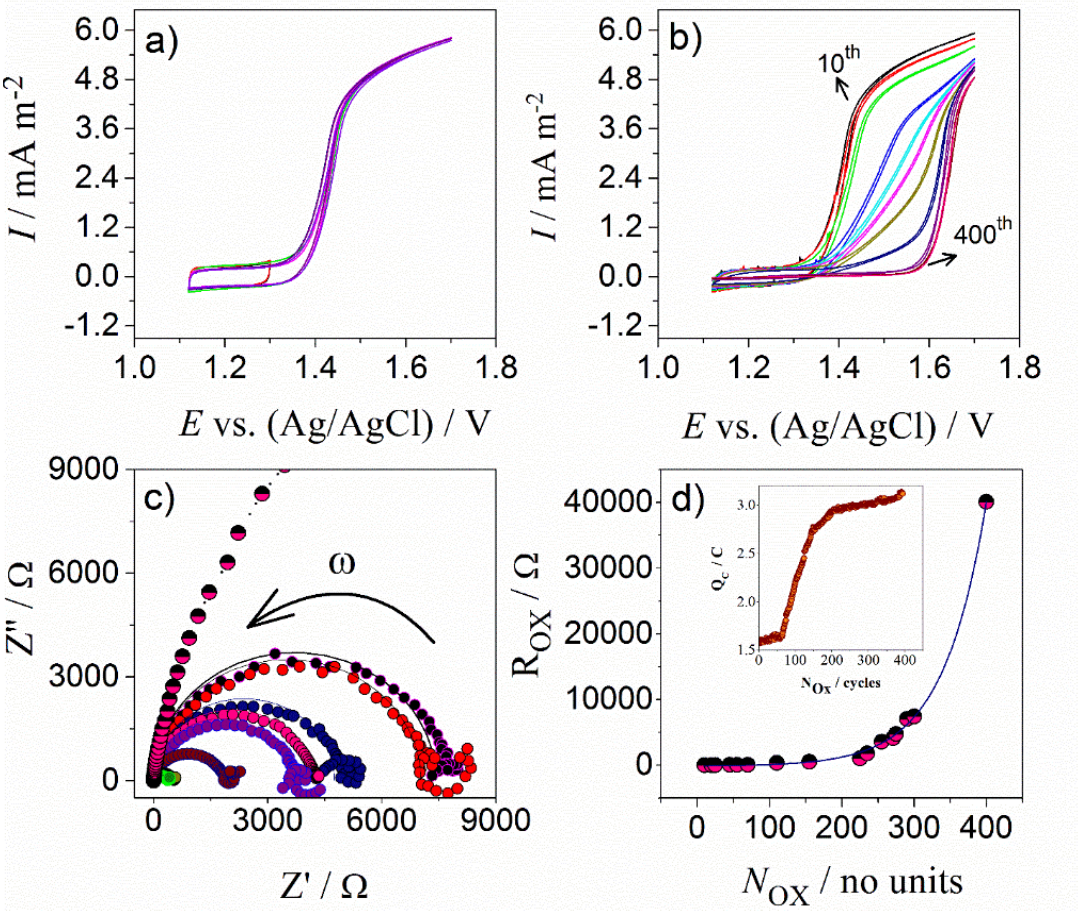

Fig. 3.6 a) Room temperature cyclic voltammetry curves for as- dealloyed np- Au in 1M $HClO_4$ recorded at a scan rate of 1 mV/s in two selected potential intervals, $1.1 < E < 1.3$ V and $1.1 < E < 1.7$ V. b) Voltammetry curves recorded in the potential interval, $1.1 < E < 1.7$ V in 343 K. Ten voltammetry curves depicted in the figure are representative of the overall behavior of 400 successive voltammetry scans. In order not to obscure the plot, ten selected voltammetry curves from the 400 successive scans (scan nos.: 10, 20, 25, 45, 55, 70, 110, 155, 235 and 400) are depicted. c) Nyquist plots for oxide formed np- Au in 1M $HClO_4$ recorded at 1.15 V in 343 K. These plots are obtained subsequent to completion of each voltammetry scans in sub figure (b). The arrow indicates the direction of measuring frequency ω. d) Variation of charge transfer resistance R_{Ox} corresponding to the formation of Au oxide as a function of pre-cyclic voltammetry scan number N_{Ox}. Inset in sub figure (d) shows cumulative charge Q_c transferred in four hundred successive pre-cyclic voltammetry scans of as- dealloyed np- Au in 1M $HClO_4$ in the oxide formation potential intervals, $1.1 < E < 1.7$ V. A Ag/AgCl reference electrode used here had a shift of - 198 mV with respect to the SHE.

Even though the electrochemical experiments can easily differentiate the microscopic variations between electro-oxidation and oxygen reduction reactions at np-

Au/1M $HClO_4$, the microstructure details at the ligament surfaces in as-dealloyed, oxide formed and reduced np- Au are not well understood. It is suggested to use high resolution transmission electron microscopy to envisage this critical issue. In fact, it becomes necessary and important to identify whether the repeated cyclic scans in the oxide formation potential intervals $1.1 < E < 1.7$ V modify the microstructure and chemical stoichiometry at the ligament surfaces in np- Au.

Despite the electrochemical charge transfer behavior discussed in np- Au towards the initial stage of electro-oxidation, the present results provide some important clues: Au surface in as- dealloyed np- Au is in hydrated form [20,103], Au oxide (Au_2O_3) layers reside in the ligament surface or pore region in oxide formed np- Au and Au surfaces in oxygen reduced np- Au is chemically inert. It is evident from the analysis of the high resolution TEM images (cf. Figures 3.7, 3.8 and 3.9)) and based on the independent microstructure studies performed to assess the electrochemical pre-treatment effect on np-Au by scanning electron microscopy (SEM) that the ligament diameter in as- dealloyed and oxide formed np- Au are found to be the same. For instance, the ligament diameter determined from the analysis of SEM micrographs is 6 ± 2 nm for as- dealloyed np- Au and 5.5 ± 2 nm for oxide formed np- Au and these values do not vary simply with the variation of temperature below 363 K. These observations are in a direct contrast with the existence of prominent ligament coarsening effect in oxygen reduced np- Au (cf. Figure 3.8) where the SFT like defect structures that have appeared in as- dealloyed (cf. Figure 3.7) and oxide formed np- Au (cf. Figure 3.9) are found to be absent. It should be noted that one of our earlier work, where the temperature effect on the surface area in np- Au is discussed, demonstrated the role of oxygen ads-species to the weakening of the ligament coarsening in as- dealloyed np- Au. An exciting question in these situations requiring attention is whether the weakening in the ligament coarsening phenomenon in oxide formed as- dealloyed np- Au is related either due to the generation of SFT defect structure or due to oxygen species (oxygen ads-species and oxides) present in the ligaments. Finding the explanation starts looking first how the oxide layer resides at the ligament surfaces contribute for the prevention of ligament coarsening and later discuss what is the role of defects in oxide formed np- Au might do for preventing the ligament growth [20].

If it is assumed that the oxide layer surrounded the ligament surfaces is contributing for the weakening of ligament coarsening, then, one would expect that the oxide formation passivates the diffusivity of oxygen into the underlying lattices. Since the oxygen diffusion behavior in hydrated as- dealloyed np- Au being unclear and the oxide formation process in np- Au becomes more effective at more positive potentials ($E > 1.4$ V), for understanding, a set of four hundred cyclic voltammograms recorded in the oxide formation potential intervals $1.1 < E < 1.7$ V [cf. Figure 3.6 b)] were analyzed. The analysis of these voltammograms yielded cumulative charge Q_c value for the repeated cyclic scans. The results are shown in the inset in Figure 3.6 d). The Q_c values depicted were obtained after subtracting the irreversible component developed during the successive scans. It includes any trace amount of Au that might be dissolved simultaneously with the oxide formation reactions [104]. For the scan number $N_{Ox} = 1$ - 55 (measurement temperature 273 K), the variation of Q_c value with N_{Ox} is found to be small. When the scan number N_{Ox} exceeded 55, the Q_c value increases rapidly at the beginning, followed by a decrease in the variation with N_{Ox}. It is seen that in the range $N_{Ox} = 56$ - 400 (measurement temperature 343 K), the variation of the Q_c value is found logarithmic with the scan number N_{Ox}. Based on the logarithmic oxide growth behavior obtained from the Q_c versus N_{Ox} plot (cf. inset in Figure 3.6 d)) and the trivalent oxidation state of Au formed on the ligament surfaces as confirmed from the analysis high resolution TEM images we attempt to explain that the oxide formation on as- dealloyed np- Au proceeds initially through the place exchange process according to the reaction,

$$AuOH \rightarrow AuO + H^+ + e^- \qquad (3.3)$$

and followed by a conversion and growth of Au_2O_3 on top of AuO by a chemical reaction,

$$2AuO + H_2O \rightarrow Au_2O_3 + 2H^+ + 2e^- \qquad (3.4)$$

These cascade reaction steps involved in the development of Au_2O_3 are in favor to the literature reports that the hydrated Au surface electrochemically oxidizes with higher valence state [99,105].

3.3.1.3. Effects on microstructure

The high resolution TEM results obtained on as-dealloyed, reduced and oxide formed np- Au samples are summarized in Figures 3.7, 3.8, 3.9, respectively. The low magnification TEM images of as-dealloyed, oxygen reduced and oxide formed np- Au are as shown in Figures 3.7 a), 3.8 a) and 3.9 a), respectively. The images illustrate the typical microstructure of nanoporous materials of nanometer sized ligament networks and interconnected pore space. Dark regions appeared in these micrographs illustrate the overlap of the ligament structure in the two-dimensional projection. Careful analysis of high resolution TEM image obtained in the marked area in Figures 3.7 and 3.9 showing several sub atomic defect structures viz., SFTs, and SFs and twinning in as- dealloyed and oxide formed np- Au. Detailed analysis has been able to reveal the structural features present in the nanoporous ligament networks. Interestingly, triangular shaped image contrast of dimensions 2 to 3 nm, representative of stacking fault tetrahedron (SFT) defects are found in a number of places in the projected image along (011) zone axis. It is worth noting that the lattice defect structures in as- dealloyed and oxide formed np- Au are presented uniquely in all samples investigated and their appearance is close or similar to the defect features reported in fcc metals under different processing conditions viz., irradiation, severe plastic deformation, quenching from temperatures close to their melting point [106–108]. Remarkably, SFT defects that are creating obstacles for the deformation activity in metallic systems [8] are found to be absent in the reduced np- Au. This implies that the SFTs are annealed out in reduced np- Au during the reduction process through ligament coarsening shown schematically in Figure 3.10 [4].

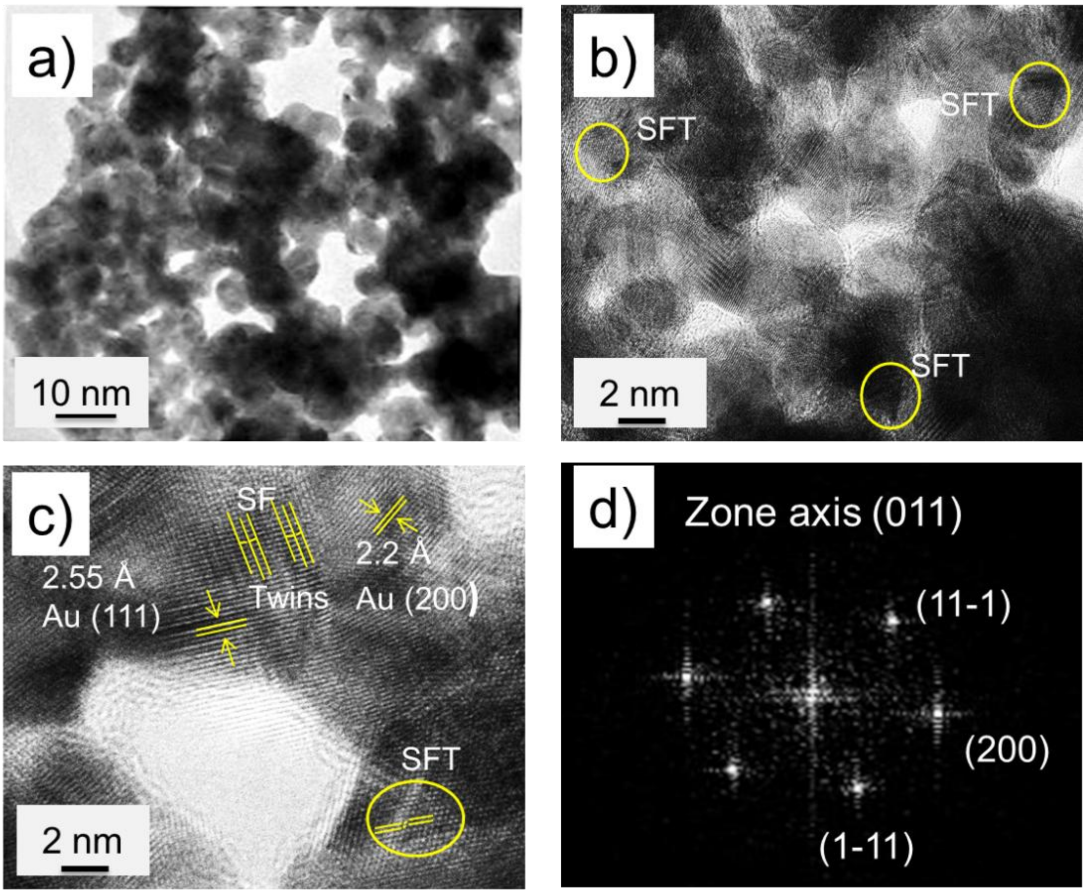

Fig. 3.7 a) Low-magnification TEM image of as- dealloyed np- Au, showing typical nanoporous microstructure of nanometer sized interconnected ligament networks and continuous pores. b), c) High resolution TEM images of selected areas in sub figure (a). Au (111) and Au (200) crystallographic arrangements and the presence of various lattice defects viz., SFT, SF, twinning are marked in these sub figures. No oxide phase can be detected in the analysis of these high resolution TEM images. d) FFT pattern of the selected area electron diffraction image in sub figure (b) showing the presence of Au (111) and Au (200) planes with their inter-planar spacing of 2.55 Å and 2.15 Å, respectively.

The Fast Fourier transform FFT pattern (Figure 3.7 d)) of the selected area in the high resolution TEM image as shown in Figure 3.7 b) revealed the presence of Au (111) and Au (200) planes with inter-planar spacing of 2.55 Å and 2.15 Å, respectively, in as-dealloyed np- Au . The FFT pattern of the selected area in Figure 3.9 a) which corresponds to oxide formed np- Au revealed the presence of two crystalline phases, Au and Au oxide. The crystallographic planes identified in np- Au in the oxide passivated condition (cf. Figure 3.9 b), c)) are Au (111), Au (200) and Au_2O_3 (111) with inter-planar spacing of 2.35 Å, 2.08 Å and 3.5 Å, respectively [109]. It should be noted that the inter-planar spacing for Au (111) and Au (200) in reduced and oxide formed np- Au samples are identical (cf. Figures 3.8 b) and 3.9 c)) and this striking observation provide some important clues for understanding the origin of the larger Au-Au inter-planar spacing yielded in as- dealloyed np- Au .

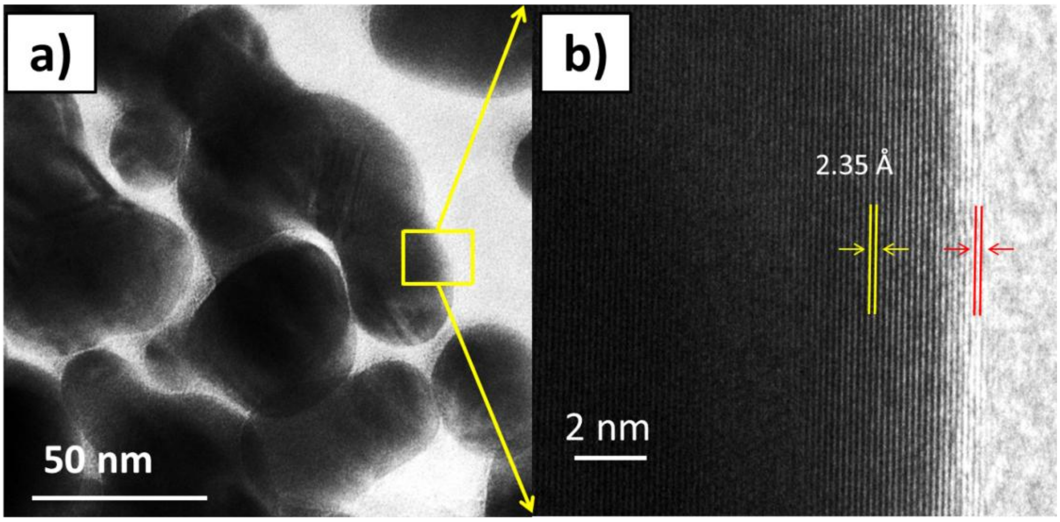

Fig. 3.8 a) Low-magnification TEM image of reduced np- Au, showing typical nanoporous microstructure of nanometer sized interconnected ligament networks and continuous pores. b) High resolution TEM image of a selected area in sub figure (a). Typical Au (111) crystallographic arrangement with inter-planar spacing of 2.35 Å is seen from the analysis of the high resolution TEM images.

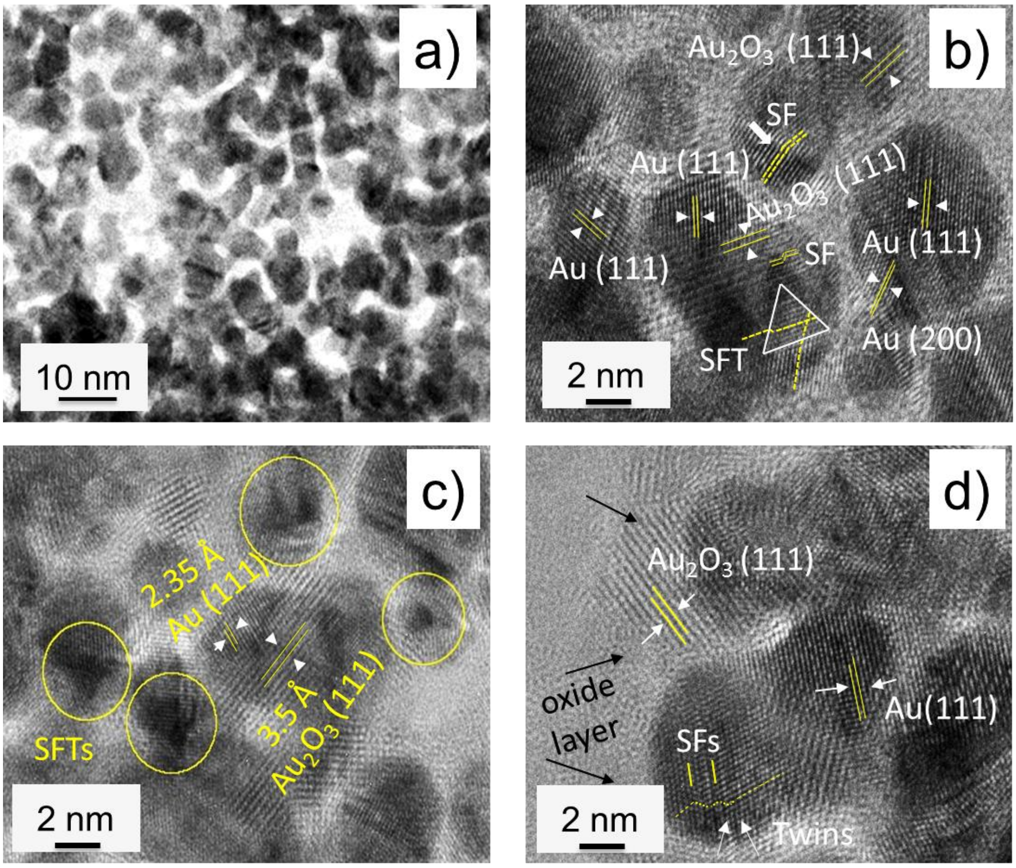

Fig. 3.9 a) Low-magnification TEM image of oxide formed np- Au, showing typical nanoporous microstructure of nanometer sized interconnected ligament networks and continuous pores. b) - d) high resolution TEM images of the selected area in sub figure (a). Au (111) and Au (200) crystallographic arrangements with the presence of various lattice defects viz., SFT, SF, twinning are marked in these sub figures. Noting that a thin Au_2O_3 (111) oxide layer with inter-planar spacing of 3.5 Å formed at the ligament surface. Inter-planar spacing for Au determined from the FFT pattern of the selected area in the high resolution TEM images are 2.35 Å for Au (111) and 2.08 Å for Au (200).

Next, the electron energy-loss spectroscopy (EELS) results obtained for all three samples are summarized. Figure 3.11 shows the electron energy-loss spectra recorded close to O-K edge at selected area in the high resolution TEM images of as- dealloyed (black line), oxide formed (red line) and reduced (blue line) np- Au. It is seen that the oxygen contents are higher in the oxide formed np- Au. According to the high resolution TEM results of oxide formed np- Au, the oxide layer spreads over the ligament/pore surfaces (cf. Figures 3.9 c), d)). This observation is in line with the reported results by

Zugic et al., [29], that the np- Au subjected to ozone gas treatment results in the formation of 1 - 2 nm Au oxide layer at the surface of the ligaments. Also, it is seen from the high resolution TEM images (Figure 3.9) that the oxide layer gets detached in several places from the Au ligaments. This indicates that under strong oxidation potentials (> 1.6 V), the Au oxide layer experiences electrochemical dissolution.

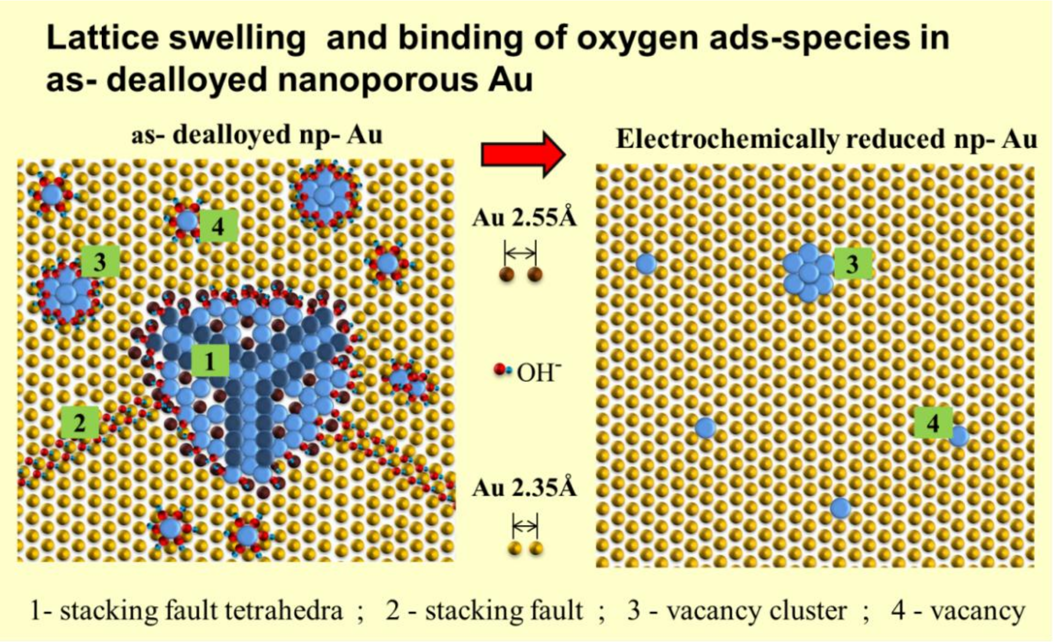

Fig. 3.10 A schematic representation of defects present in as- dealloyed np- Au. These defects are annealed out in reduced np- Au.

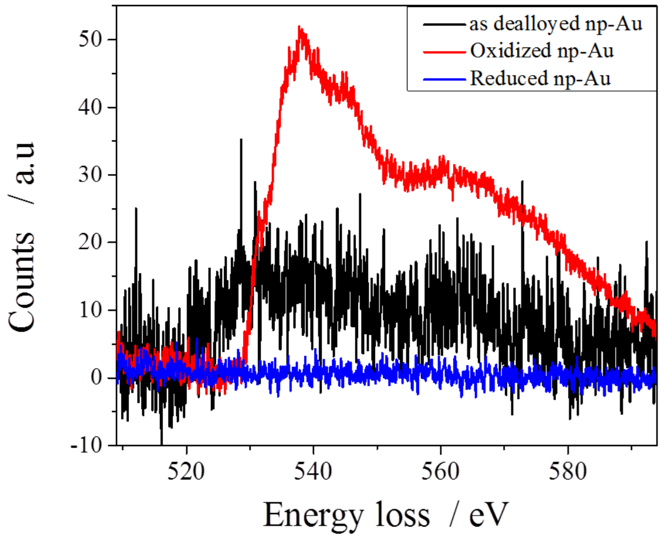

Fig. 3.11 Electron energy-loss spectra of np- Au recorded in as- dealloyed (black line), oxide formed (red line) and reduced (blue line) conditions.

The structural results obtained from the high resolution TEM images (cf. Figures 3.7, 3.8 and 3.9) indicate that the inter-planar spacings for Au (111) and Au (200) planes in as- dealloyed np- Au are not identical with those obtained in oxide formed np- Au or in reduced np- Au or in bulk Au reported in Ref. [109].

We have observed that oxygen ads-species in place with the Au atoms acts as charged dipoles and promote for the weakening of inter-ligament interactions [20].It is inferred from a series of positron annihilation studies on as- dealloyed np- Au, which demonstrates the evolution of defect structure with annealing temperature [3,8,21], that vacancy defects that are generated in the ligaments, during the formation of nanoporous structure, migrate towards the ligament/pore surfaces and agglomerate in the form of vacancy clusters. On correlating the reported positron annihilation results with the present high resolution TEM results, it is inferred that the vacancy clusters that generate in the ligaments by the aggregation of vacancies relaxed in the form of SFT defect structures. Notably, these SFTs present in oxide formed np- Au are not affected by the generation of Au_2O_3 oxides at the ligament surfaces as revealed by Figures 3.7 and 3.9. This implies that, irrespective of the chemical modifications at the ligament surface, the SFTs generated through vacancy agglomeration is found to be stable in both as- dealloyed and in oxide formed np- Au. It has been identified from the analysis of the high resolution TEM images, the inter-planar Au (111) and Au (200) spacing in as- dealloyed np- Au is largely by 8% (cf. Figure 3.7) in comparison to that obtained in oxide formed (cf. Figure 3.9) and reduced np- Au (cf. Figure 3.8). Microscopically, such differences emerge because np- Au samples used for the investigations were treated under different electrochemical potential conditions. The absence of such a swelling effect in the oxide formed np- Au are suggesting that weakly coupled oxygen ads-species with the Au atoms in the bulk might have detached and dispersed out during the formation of Au_2O_3 oxide layer.

Since the three different pre-conditioned np- Au samples investigated above have shown the characteristic nanoporous microstructure, an ensemble of interconnected pores with three-dimensional coherent ligament network with highly non-uniform curvatures, it is suggested that the fine structural features evolved in np- Au are highly sensitive to specimen geometry and local structure [8,17]. In this phenomenological sense, it is believed that the lattice swelling effect emerged in as- dealloyed np- Au may be caused by the combined effect of Au lattice defects and the presence of coupled oxygen ads-species. Apparently, this suggests that the oxygen species in as- dealloyed np- Au bind, albeit weakly, on Au atoms in the presence of lattice defects and modify the structural properties in the ligament - pore network. Microscopically, the ligament structure adopts a unique configuration in which the atomic defects and oxygen containing species interacts together with the Au atoms and contribute to the overall functioning of the ligament-porous network structure. Recent studies exploring the catalytic effect in np- Au suggested that Au is catalytically active not only in its chemically pure form, but, also, holding variety of catalytic reactions in the presence of easily reducible oxygen adsorbed species [28–30]. In the above kinds of situations, there are good reasons, related both oxygen present in the ligaments and the lattice defects that are emerged in as- dealloyed np- Au to the prevention of ligament growth. This in-turn depends on how effectively the oxygen species and defects present contributing to prevent the ligament coarsening in as-dealloyed and oxide formed np- Au, which in principle does not happen in reduced np-Au because Au is chemically considered as inert in its reduced form.

3.4. Conclusion

The results presented in this chapter show how the electrochemical technique combined with transmission electron microscopy can be used to obtain the microstructure and chemical information of np- Au towards electro-oxidation (initial stage of oxidation and oxide formation) and oxygen reduction reactions in aqueous medium. Pseudo-capacitive double layer structure develops explicitly at the as- dealloyed nanoporous Au/$HClO_4$ interface. In contrast, the electrochemical interface structure at the reduced nanoporous Au/$HClO_4$ interface is capacitive. Initial stage of electro-oxidation corresponding to the monolayer adsorption of oxygen containing species occurs on the ligament surfaces in reduced np - Au in three potentials and their separation on the electrode potential scale depends substantially on the energetically favorable Au lattice sites present on the ligament surfaces. The formation of oxides in as- dealloyed np - Au occurs in a sequential conversion of Au - OH dipoles to AuO and subsequently by a conversion and growth of Au_2O_3 on top of AuO. Formation of oxide on the ligament surfaces in as- dealloyed np- Au follows logarithmic growth process.

The inter-planar spacing for Au (111) and Au (200) in as- dealloyed nanoporous Au has increased by 8% in comparison to those obtained in reduced nanoporous Au or in bulk Au. The occurrence of such unusual lattice swelling effect evolved in as- dealloyed np- Au, in contrast to reduced np- Au or bulk Au may be attributed to the binding of oxygen ads-species, albeit weakly, in the presence of lattice defects. The results obtained from the present study are suggesting that the modified properties in np- Au in conjunction with the variation of electrochemical pre-treatment conditions depends highly on the atomic and microstructure features present locally in the ligament network. In addition, we have also demonstrated through combined electrochemical impedance and transmission electron microscopy investigations that the microscopic features evolved during the formation of nanoporosity are stabilized in both as- dealloyed and oxide formed np- Au samples and these observations are important for the use of np- Au based materials in irradiation and high temperature environments. Since the field of np- Au catalyst spans a wider range of applications starting from energy to medical resources, the results discussed in this thesis may be also useful for the design and development of smaller scale metal catalyst.

Chapter 4

Measurement of specific surface area of nanoporous Au

The specific surface area measurement on nanoporous materials play a major role in the optimization of fabrication processes of nanoporous based devices to achieve desired physico-chemical properties. In this chapter the specific surface area measurements of nanoporous Au using the electrochemical double layer charging methods and adsorption methods (Oxygen adsorption/desorption, BET) are described. The experimentally measured surface area results obtained are compared with the geometrical surface area of nanoporous Au.

4.1. Introduction

The strategies in the design of nanoporous metals for functional applications depend on a number of parameters. The important ones are surface area, geometry of the pore-ligament interconnects and chemical nature of atomic layer present at the pore surfaces and their interaction with surroundings, be it in fluidic or gaseous media [1,14,110]. Among these, the dominant interest has been focused on the surface area of nanoporous metals since their specific surface reactivity depends on the delocalized atoms at the pore surfaces and their co-ordination with the interacting medium. For instance, the electric field induced mechanical actuation effect has been observed in nanoporous metals [13,14,100]. There is an increased grafting density of biological molecules on np- Au [111]. Also, the nanoporous Au surfaces exhibit unexpected catalytic activity [1,14,30,112].

Electrochemical measurements like electrosorption of hydrogen and oxygen adsorbed atoms [113], under potential deposition (UPD) of metal atoms on test substrates [114,115] and Brunauer-Emmet-Teller (BET) method [116,117] have been used regularly for the determination of surface area in solid materials. Despite the advantages of surface area measurement techniques based on the analysis of adsorption/desorption isotherm, there are difficulties on using these techniques for the determination of true surface area in nanocrystalline metallic materials such as nanoporous metals where the atom diffusivity in the surface layer is quite high at room temperature. The reason is mainly became of the formation of surface diffusion controlled reconstruction rather than a simple atomic displacement, bond breaking, facets and atomic coarsening processes that occur during heat treatment. STM measurements by Magnussen et al. have revealed that anions chemisorbed with metal electrodes weaken the bond strength between metal atoms and facilitates surface atom transport [118,119]. Liu et al. pointed out that the thickness dependent kinetics of UPD layer formations in nanoporous metals affect the determination of their true surface area [115]. Various other molecular adsorption methods such as CO, H_2 and H_2-O_2 titration can also be used to throw light on the surface area in nanoporous solids. Of all these methods, electrochemistry based techniques offer advantages as the preparation of the nanoporous samples and the determination of surface area can be carried out at under ambient conditions in an electrochemical cell without exposure of the probe samples to other environments. In the backdrop of above, the present chapter strives to bring forward a development of an in-situ electrochemical experimental method for determination of surface area of nanoporous metals such as np- Au.

We used double layer capacitance ratio method [113] to study the temperature effect on the variation of surface area in np- Au. In the electrochemical double layer interface, the net charge transferred across the electrode surface occurs mostly by the coupled influence of diffusion of ions in the electrolyte and electrostatic forces [32,120]. Since the important contribution to the double layer charging originates from the electrode surfaces, electrochemical capacitance method determines accurately the surface area of the probed materials from the knowledge of the net charge transferred [32,113,120] . In addition to the capacitance ratio method, the surface areas of np- Au samples have been measured using the standard BET method and the process of adsorption/desorption of OH_{ads} species.

4.2. Determination of surface area of np- Au

4.2.1. Electrochemical method

Figure 4.1 summarizes the typical cyclic voltammogram of Au in aqueous acidic electrolyte. It has the advantage of resolving the charge layer on top of the Au surface, called as double layer capacitance and the charge layer that formed at the adsorbed Au surface, which is known as pseudocapacitance.

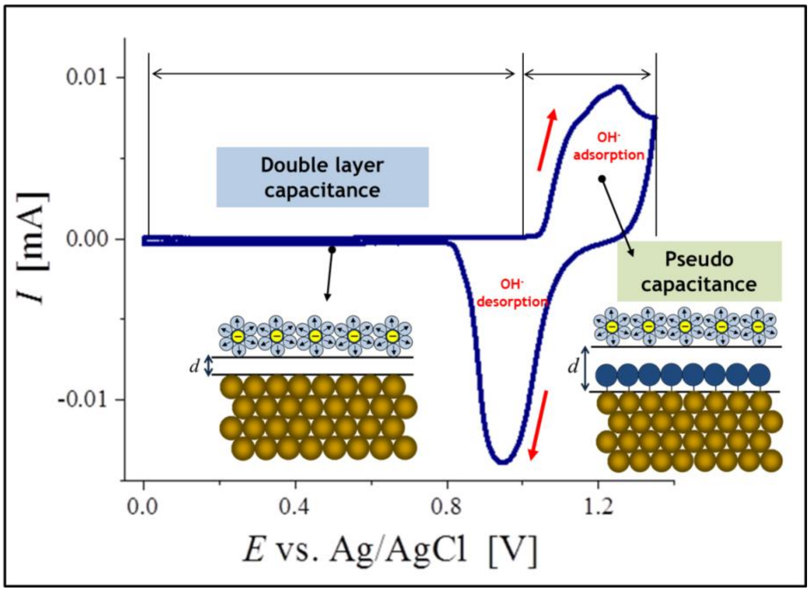

Fig. 4.1 Room temperature cyclic voltammetry for Au in $HClO_4$. Typical voltammogram of Au in a wider potential interval showed features of weakly ion adsorbed double layer dominant pseudocapacitance region and double layer dominant region.

The schematic view of the double layer and pseudocapacitive layer formed on the Au surface is shown in Figure 4.1. While the double layer capacitance forms across the metal surface at electrode-electrolyte interface, in the case of pseudocapacitance component the capacitive layer forms across the adsorbed oxygen containing ads-species of metal surface. The cyclic scan shows oxidation/reduction plateaus at the positive anodic potentials and a featureless constant anodic/cathodic current flow at lower potential region. This indicates that double layer charging became dominant in the lower potentials of the cyclic scan and the adsorption process occurred significantly at higher potential. Since the characteristic features in the voltammogram are well resolved. It has the advantage of separating out the charge corresponding to the double layer component and the pseudocapacitive component in the oxidation/reduction region. The electrochemical charging or discharging of the double-layer capacitance arise at all electrodes/electrolyte interfaces due to electron/ion charge separation across the interface and voltage dependent solvent-dipole orientation in the electrode/electrolyte interface [19].

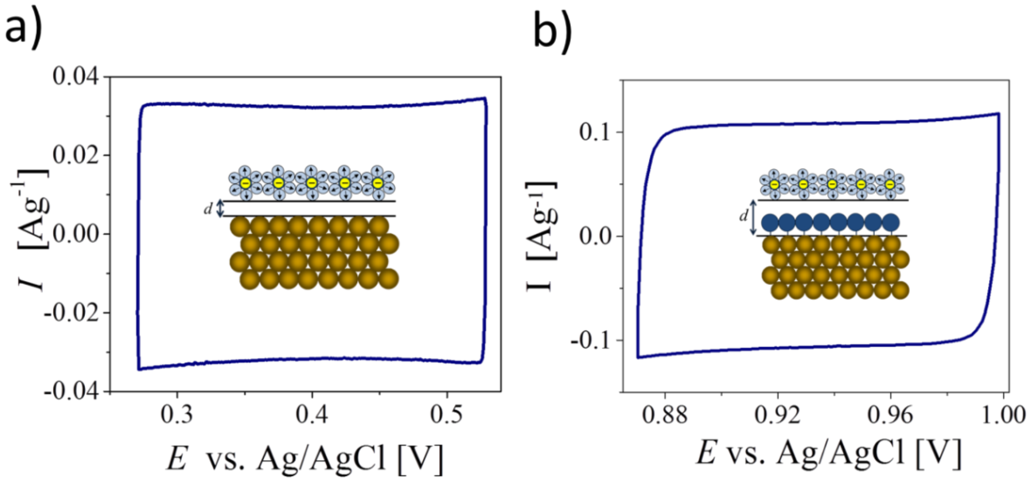

Fig. 4.2 Room temperature cyclic voltammograms CVs of specific current I versus electrode potential E versus pseudo Ag/AgCl electrode for Au in two distinct capacitive behavior a) double layer capacitance and b) pseudo-capacitance. Insets figures 4.2 a) and b) shows the double layer formation on two distinct surface states.

The typical CV behavior for Au corresponding to the double layer charging and pseudocapacitance charging is shown in Figure 4.2 a) and b) respectively.

4.2.2. Cyclic voltammetry during reduction sweep

It may be worth to note that the open circuit potential (OCP) value obtained on as-dealloyed np- Au is ~0.85V versus Ag/AgCl pseudo reference electrode. It is roughly 600 mV higher in the positive anodic potential than that obtained on polycrystalline planar Au electrode [121]. It indicates that the as- dealloyed np- Au contains considerable amount of adsorbed species that are retained in the nanoporous structure during the dealloying process. To remove the adsorbed species, the as- dealloyed np- Au is immersed in $HClO_4$ and potentially cycled successively in a wider potential interval, between -0.3 and 0.9 V, at a scan rate of 1mV/s. This cyclic voltammetry reduction sweep helps to attain clean metallic Au surface [cf. Figure 4.3 a)]

Figure 4.3 displays the time-dependent changes in the cyclic voltammograms for as- dealloyed np- Au samples in 0.1M $HClO_4$ electrolyte. Twenty one successive cyclic current I versus E scans are depicted in the Figure 4.3 a). The cyclic voltammograms showed the electrochemical characteristic features of Au, such as plateaus corresponding to the adsorption and desorption of oxygen containing species at the positive end (ca. 0.5 – 0.9 V) and a constant current passed double layer interval (between - 0.3 and 0.5 V) for Au surfaces after the first broad reduction peak in the cathodic scan. The start potential E_s for the cyclic scans displayed in Figure 4.3 a) is close to the open circuit potential (OCP) value 0.85 V versus Ag/AgCl pseudo reference electrode for the as- dealloyed np- Au sample. Figures 4.3 b) and 4.3 c) show the changes in applied potential E and the net charge transferred δQ_n during the twenty one successive potential cycles.

On assuming the concentration of oxygen containing adsorbed species in as-dealloyed np- Au to be virtually equal to zero after the successive cyclic scans between -0.3 and 0.9 V, we determine the net charge transferred that corresponds to the complete desorption of adsorbed oxygen containing species from the transferred cumulative charge $\delta Q_{c(1\text{-}21)}$ estimated from δQ_n versus t plot [cf. Figure 4.3 c)]. Figure 4.3 d) shows δQ_c value as a function number of cyclic scans. It is seen that the $\delta Q_{c(1\text{-}21)}$ value reached 3.23 C. This observation offers an opportunity to validate the reduction process involved during the transformation from as- dealloyed np- Au surface to reduced np- Au surface. Now, it is worthwhile to comment upon the possibility of transformation from as- dealloyed np- Au to reduced np- Au during the electrochemical reduction. Such a process is expected to proceed by the gain of one electron or more than one electron per surface atom. To gain insight into this scientifically sensitive issue, we analyze the charge δQ_{diss} corresponding to the dealloying current I_{diss} for Ag dissolution and the cumulative charge δQ_c transferred from each cyclic scan.

The dealloying current I_{diss} measured during Ag leaching out from the alloy $Ag_{75}Au_{25}$ is found to decrease exponentially with dealloying time t. This decreasing trend can be understood, as there is a continuous removal of Ag atom flux from the alloy $Ag_{75}Au_{25}$ with time. The dealloying behavior observed is very similar to the previous experimental observations and theoretically simulated reports [19]. If the current I_{diss} measured during the dealloying event is solely due to electrochemical Ag oxidation reaction $Ag^0 \rightarrow Ag^+ + e^-$, then the net charge δQ_{diss} value of 12.76 C determined from I_{diss} versus t plot, using the relation, $Q = \int I.\, dt$, should provide the information about the number of Ag atoms removed from the alloy $Ag_{75}Au_{25}$ of mass 16.5 mg. With 55.86 x 10^{20} Ag atoms present in one gram, the amount of Ag atoms N_{Ag} removed from the original alloy $Ag_{75}Au_{25}$ can be calculated. As compared to δQ_{Ag} value of 9.16 C obtained from the amount of Ag atoms dissolved N_{Ag} by the oxidation reaction $Ag^0 \rightarrow Ag^+ + e^-$, the net charge δQ_{diss} value of 12.76 C, determined from the dissolution current I_{diss} is rather large having an extent close to 35 %. This implicates that the net dissolution charge

δQ_{diss} is a function of two different variables: the charge δQ_{Ag} corresponding to the amount of dissolved Ag atoms N_{Ag} and the charge δQ_{Oads} corresponds to the amount of oxygen containing O_{ads} species present in as- dealloyed np- Au. Therefore, the charge that corresponds to the O_{ads} species present in as- dealloyed np- Au may be estimated as, $\delta Q_{\mathrm{Oads}} = \delta Q_{\mathrm{diss}} - \delta Q_{\mathrm{Ag.}}$ The presence of O_{ads} species in as- dealloyed np- Au is originally discussed by Wang et al. [110], Zeis et al. [30], and Wittstock et al. [11].

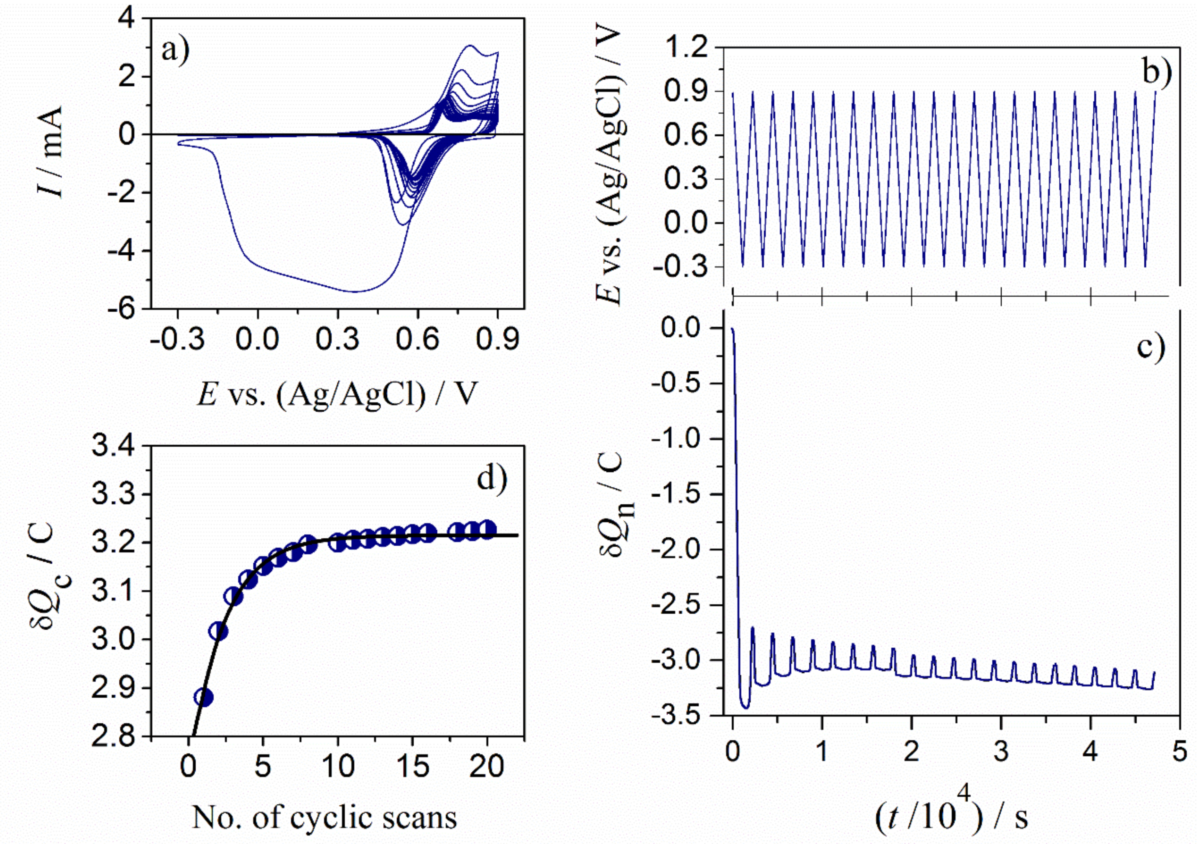

Fig. 4.3 Results of electrochemical reduction process in as- dealloyed np- Au. a) Twenty one successive cyclic voltammograms of as- dealloyed np- Au recorded in a wider potential interval -0.3 to 0.9 V at a scan rate of 1 $\mathrm{mVs^{-1}}$. b) and c) Changes in applied cell potential E versus Ag/AgCl and net charge δQ_n transferred during the twenty one successive scans of figure a), respectively. Since the charge δQ_n transferred in the first cathodic scan is much higher the charge values in the subsequent oxidation/reduction scans are not balanced to $\delta Q_n = 0$ in the y-axis. d) Cumulative charge δQ_c transferred at the end of each successive reduction scan.

By inspection of the charge values obtained from the dealloying and the reduction events, it is seen that the estimated charge δQ_{Oads} value 3.6 C corresponding to the O_{ads}

species present in as- dealloyed np- Au sample is nearly equal to the measured charge $\delta Q_{c(1\text{-}21)}$ value 3.23 C that corresponds to complete reduction of O_{ads} species in reduced np- Au. As a verification of reproducibility, similar experiments were performed on three more samples in identical experimental conditions. The consistency in the results obtained from trail experiments strongly suggests that oxygen containing species in the electrolyte are coupled with all the diffused Au atoms originally from the alloy phase during the evolution of nanoporous Au architecture. Its reduction during the transformation from as- dealloyed np- Au surface state to reduced np- Au surface state is mostly governed by one electron transfer process.

It is noteworthy to mention that as shown in Figure 4.3 c) the charge δQ_n transferred in the first cathodic scan, is much more than the net charge transferred in the remaining cyclic scans. This clearly indicates that majority of the adsorbed O_{ads} species in as- dealloyed np- Au get desorbed during first reduction scan. The current *I* versus potential *E* behavior depicted in 2 - 21 cycles of Figure 4.3 a) are typical for surface evolution with systematic increase in ligament coarsening. The cumulative charge $\delta Q_{c(2\text{-}21)}$ corresponding to the reduction reaction on ligament surfaces of np- Au during the successive cyclic scans 2 to 21 gives 0.34 C for a 6.3 mg sample. For the value $\delta Q_{c(2\text{-}21)}$ = 0.34 C, the coarsened surface area is calculated as $\alpha_c = \delta Q_{c(2\text{-}21)} N_A/Fd_s$. N_A is the Avogadro’s number, F denotes Faraday constant and d_s is the areal density of surface atoms. This density is 1.53×10^{19} atoms m^{-2} for fcc metals. It gives 22.5 m^2 g^{-1}. As it was previously mentioned majority of as- dealloyed np- Au containing a significant amount of O_{ads} species gets desorbed during first reduction scan. A close inspection of Figure 4.3, suggests that the coarsened behavior in as- dealloyed np- Au during the first cathodic scan is not clearly understood since the amount of desorbed O_{ads} species that contributes to modify the porous-ligament surface structure is exactly not known. Due to these facts, it is difficult to quantify the true coarsened surface area which relates to the as- dealloyed np- Au to reduced np- Au transformation.

The present results are discussed on the basis of established phenomenology of oxidation/reduction of metals as reported in Ref. [122]. We safely assume that the electrochemical reduction of positively charged metal surfaces recovers to pure metal surfaces. The current indicative of the transformation of positively charged metal surfaces to the reduced clean metal surfaces involve rearrangement of surface metal atoms [123] since the electrode-electrolyte interface inevitably try to bring in equilibrium. This strongly suggests that, when the cell potential sweeps in more negative in the cathodic scan, the diffusivity of Au atoms at the pore surfaces became more effective which initiates ligament coarsening. To this, our experimental sequence aims towards investigating as- dealloyed np- Au and reduced np- Au surfaces in their double layer potential region to determine their surface area value.

4.2.3. Double layer capacitance ratio method

Electrochemical double layer capacitance ratio method was used to measure the absolute surface area of nanoporous metal samples. In the electrochemical double layer interface, the net charge transferred across the electrode surface occurs mostly by the coupled influence of diffusion of ions in the electrolyte and electrostatic forces. Cyclic voltammetry (CV) at different scan rate, υ, were recorded in the potential region where dominantly the double layer charging taking place at Au electrode. The mean current, I_{mean}, was plotted as a function of scan rate is shown in Figure 4.4.

The potential δE developed at the double layer interface changes linearly with time for a constant current I flow, i.e.

$$\delta Q = \int I . \delta t \qquad (4.1)$$

and therefore double layer capacitance C_{dl}

$$C_{dl} = \frac{\delta Q}{\delta E} \tag{4.2}$$

It can be expressed as,

$$C_{dl} = \frac{1}{\upsilon}\frac{\delta Q}{\delta t} = {I_{mean}}/{\upsilon} \tag{4.3}$$

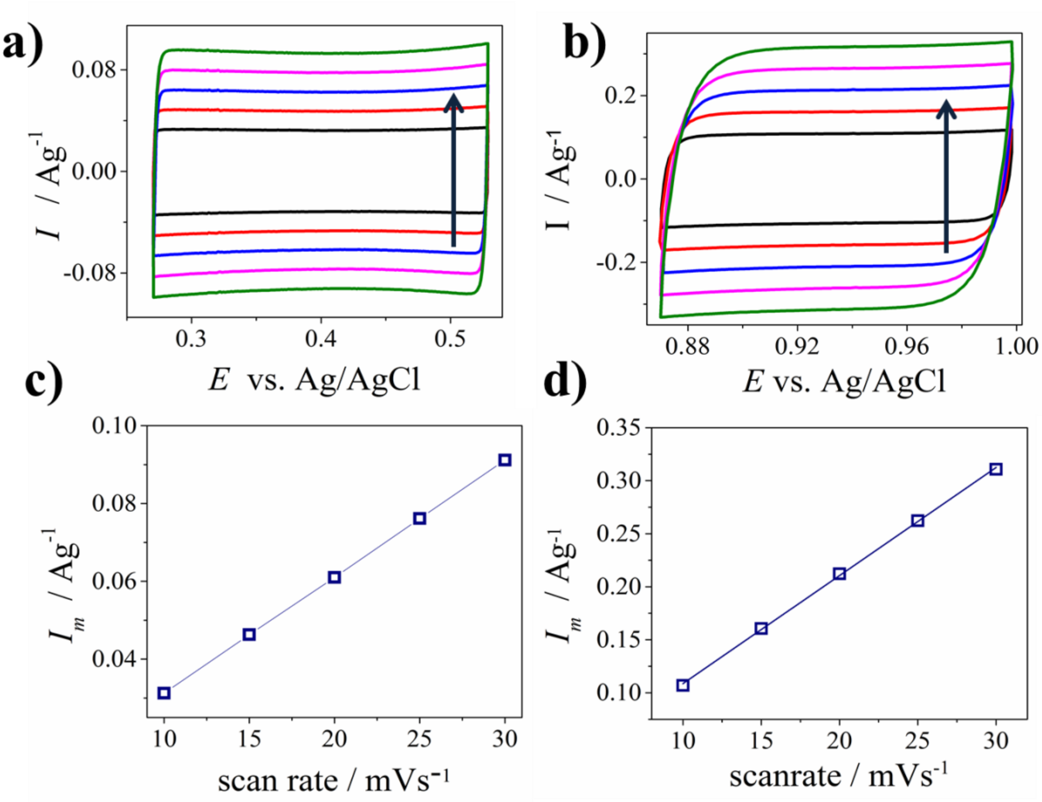

Fig. 4.4 Room temperature cyclic voltammograms CVs of specific current *I* versus electrode potential *E* versus pseudo Ag/AgCl electrode for Au in two distinct capacitive behavior a) double layer capacitance and b) pseudocapacitance at different scan rates 10 – 30 mVs^{-1}. Mean specific current I_m obtained from the CVs of c) double layer capacitance and d) pseudocapacitance with function of scan rate. Arrow indicates the increasing of scan rate.

The double layer capacitance value can be easily obtained from the analysis of cyclic current *I* versus potential *E* scans. Figure 4.4 shows a typical double layer charging and discharging behavior of metal electrode and oxygen ads- species (OH$^-$) covered metals electrode in an aqueous acidic electrolyte.

Since , Au has two different surface states such OH^- covered and reduced clean metallic, the surface area of Au can be obtained using the Jellium model [32]. This corresponds to capacity of 40μF/cm^2 in the case of double layer charging and 20μF/cm^2 in the case of pseudo double layer charging for having surface atom density of 1.5 x10^{15}/cm^2.

Specific surface area, α_m, is calculated from dividing surface area (*SA*) by sample mass, m.

Specific surface area,

$$\alpha_m = SA/m \qquad (4.4)$$

4.2.4. Determination of Surface area of np- Au using adsorption methods

4.2.4.1. OH^- adsorption/ desorption method using Cyclic Voltammetry

Adsorption/desorption of oxygen ads-species (OH^-) is one such method to determine surface area by adsorption of the metal electrode [58,113]. If OH ad-layer (OH_{ads}) forms a monolayer on the electrode surface with intermediate formation of one electron transfer product of $M(OH_{ads})$ by a charge transfer reaction,

$$OH^- + M \leftrightarrow M - OH_{ads} + e^- \qquad (4.5)$$

then the specific surface area will be,

$$\alpha_m = \frac{n_a N_A}{D_s} \qquad (4.6)$$

here, $n_a = \frac{\delta Q_{ads-de}}{F}$

where, n_a is the amount of oxygen adsorption in the monolayer, *F* is the Faraday constant, N_A denotes Avogadro's number, D_s denotes density of surface atoms, $\delta Q_{ads\text{-}de}$ is the magnitude of charge transfer. Cyclic voltammetric *I-E* curve for pure Au electrode in 1M $HClO_4$ electrolyte recorded at room temperature is shown in Figure 4.5.

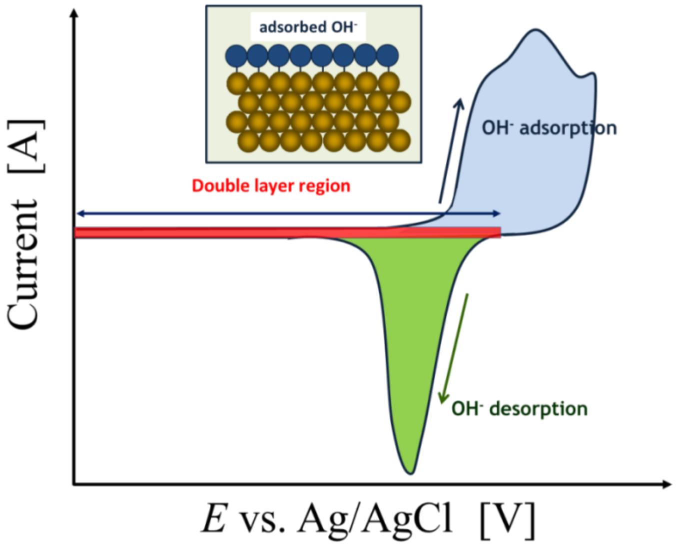

Fig. 4.5 Room temperature cyclic voltammetry for Au in $HClO_4$. A typical voltammogram for Au in a wider potential interval showed features of OH adsorption/desorption reaction and double layer charging.

The magnitude of charge transfer can be obtained from the following expression,

$$\delta Q_{ads-de} = \int I.\delta t \qquad (4.7)$$

and it can rewrite as,

$$\delta Q_{ads-de} = \frac{1}{\upsilon}\int I.\delta E \qquad (4.8)$$

The $\delta Q_{ads\text{-}de}$ can be calculated by integrating the net charge transferred. It is worth noting that the capacitive current from double layer region extends over the whole potential window. Hence the exact contribution of charge corresponding to OH^- adsorption/ desorption can be calculated as,

$$\delta Q_{ads-de} = \frac{1}{\upsilon}\int I.\delta E - \delta Q_{dl} \qquad (4.9)$$

where δQ_{dl} is associated to double layer capacitive processes in the OH^- adsorption/ desorption region.

4.2.4.2. Adsorption isotherm based Brunauer Emmet Teller (BET) method

The specific surface area is determined by physical adsorption of gas or vapor at a definite pressure in a closed container at a given temperature [116,124]. Physical adsorption results from relatively weak forces (Vander Waals force) between adsorbate gas and adsorbent surface of the sample. This determination is usually carried out at the temperature of liquid nitrogen. At low pressure, a monolayer of the gas is formed on the surface and as pressure increases, excess gas is adsorbed and it forms multilayers. The adsorption phenomenon follows the adsorption isotherm equation,

$$\frac{1}{\left[V_a\left(\frac{P_o}{P}-1\right)\right]}=\frac{C-1}{V_mC}\left(\frac{P}{P_o}\right)+\frac{1}{V_mC} \tag{4.10}$$

Where P/P_o is the relative pressure, C is the constant related to the enthalpy of adsorption of adsorbate gas on the sample, V_a is the volume of gas adsorbed at standard temperature and pressure (STP) and V_m is the volume of adsorbed gas at STP to produce an apparent monolayer on the sample surface. The values of slope and intercept from the equation 4.10 are used to calculate the monolayer adsorbed gas. From the values of V_m *(1/ (slope + intercept))* and *C ((slope/intercept) +1)*, the specific surface area, α_m, (m^2/g) is calculated by the equation,

$$\alpha_m=\frac{V_mN_a}{m*22400} \tag{4.11}$$

Where N_a is the Avogadro no. (6.023×10^{23} mol^{-1}), m is the mass of the sample. Thermo Scientific Surfer gas adsorption porosimeter (Thermo Fisher Scientific S.p.A) was used to measure the specific surface area.

4.3. Experimental details

The electrochemical experiments were performed in a commercial potentiostat (PGSTAT 302N, Metrohm Autolab e.v.). All electrochemical experiments in this study were performed under potential control using Ag/AgCl pseudo reference wire electrode.

There is a shift of -198 mV to the standard Ag/AgCl/3M KCl electrode and -398 mV with respect to the standard hydrogen electrode *SHE*. The latter study also used the scanning electron microscopy technique to investigate the evolution of surface morphology of the np- Au samples. ImageJ software was used to analyze the SEM images of the np- Au samples from which the ligament size *d* was obtained by averaging the diameter of fifty selected ligaments.

The temperature dependent electrochemical double layer experiments on as-dealloyed np- Au and reduced clean metallic np- Au samples were carried out in constant current passed anodic/cathodic regions around the cell open circuit potential (OCP) in a temperature interval of 298 – 363 K. Open circuit potential is the potential difference that develops in a cell when potential applied to the cell is disconnected. The temperature was controlled using a bath thermostat having an accuracy of ± 0.2 K shown in Figure 4.6.

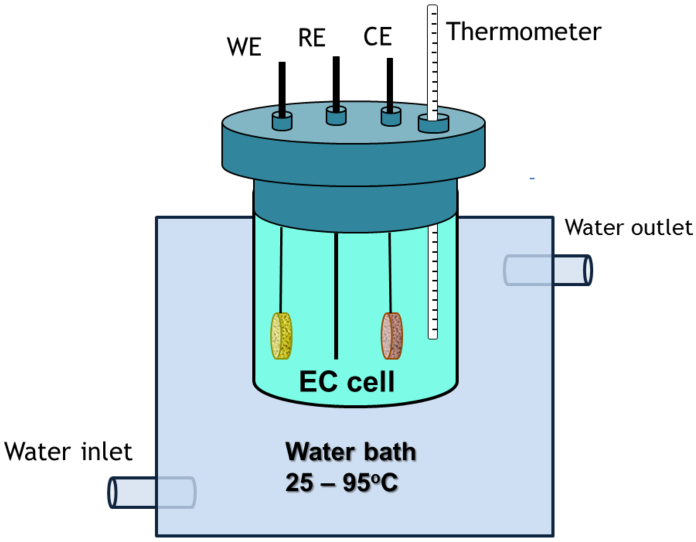

Fig. 4.6 Schematic of Electrochemical cell in water bath set-up. WE is np- Au, RE is Ag/AgCl wire electrode and CE is porous gold of surface area larger than the WE. Cell temperature was monitored by using a glass thermometer.

To remove the adsorbed species that are retained in the as- dealloyed np- Au and for obtaining characteristic electrochemical features of clean Au surfaces, the as-dealloyed np- Au immersed in $HClO_4$ was potential cycled successively in a wider potential interval, between - 0.3 and 0.9 V, at a scan rate of 1 mVs^{-1}.

BET surface area measurements were carried out on two samples of as- dealloyed np- Au having masses of 239 mg and 400 mg. The nitrogen adsorption/desorption isotherms were recorded on these samples after degassing the samples at temperatures below 523 K. Degassing treatment under conditions of dynamic vacuum is a pre-requisite for creating clean high vacuum environment prior to acquisition of nitrogen adsorption isotherms at 77 K. Thermo scientific surfer gas adsorption porosimeter (Thermo Fisher Scientific S.p.A) was used to record the nitrogen adsorption/desorption isotherms. The BET surface area results were obtained from the lower limit in initial adsorption isotherms ($0.05 < p/p_0 < 0.35$) where the coverage of nitrogen on the free surface of as- dealloyed np- Au extends only to one monolayer [117].

4.4. Results and Discussion

4.4.1. Double layer voltammetry on different surface states of np- Au

Double layer charging/discharging behavior of different surface states such as reduced and as- dealloyed np- Au in $HClO_4$ electrolyte is summarized in Figure 4.7. The reduced np- Au state from as- dealloyed state is achieved by cyclic voltammetry reduction sweep process (c.f. Figure 4.3). Figures 4.7 a) and b) shows the cyclic voltammograms, recorded on reduced np- Au state in 0.1M $HClO_4$ and 1M $HClO_4$ in the capacitive potential region at different scan rates. The cyclic scans in Figures 4.7 a) and b) are recorded in the constant current passed region centered around their OCP values 0.27 and 0.34 V, respectively. It is seen that the voltammetry curves displayed in Figures 4.7 a) and b) are symmetric in terms of charge balance in the anodic and in the cathodic scans. In a similar way the pseudocapacitance value can also be obtained for as- dealloyed state in 1M $HClO_4$ in a potential interval $0.84 < E < 1$ V as shown in Figure 4.7 c). This is around its open circuit potential (OCP) value of 0.85 V versus Ag/AgCl pseudo reference electrode. As indicated in the experimental section, the dependence of OCP value to the surface state of polarizable electrodes seems to be particularly noteworthy since the electrochemical parameters can alter electrode surface properties. Similar to the Figures 4.7 a) and b), the areas under the anodic and cathodic scans in Figures 4.7 c) is equal.

The pronounced rectangular shaped specific current i versus potential E loops appearing in Figure 4.7 c) is indicative of the fact that the adsorbed oxygen containing species in as- dealloyed np- Au during electro-corrosion of the $Ag_{75}Au_{25}$ alloy remain in place during the cyclic scans in the potential interval $0.84 < E < 1$ V. Jin et al. also reported that as- dealloyed np- Au surfaces are covered with oxygen containing adsorbed species which is consistent with our present observations [100]. On considering the weakly bonded oxidative species on the pore surfaces in as- dealloyed np- Au, the electrochemical charge transfer process across as- dealloyed np- Au can be stated to be mostly pseudo-capacitive [89] which is schematically shown in Figure 4.1.

Their square shape appearance and absence of features corresponding to reversible surface redox reactions point to the dominant contribution of equilibrium capacitive charging. Cyclic voltammetry (CV) at different scan rate ν, were recorded in the potential region where the double layer charging dominant process taking place at Au electrode. The mean specific current, i_m, was plotted as a function of scan rate. It is seen that the current value in both anodic and cathodic sweeps in the cyclic scans increases with the scan rate ν and the variation of mean specific current i_m, is found to be a linear function with ν. Figures 4.7 d) - f) display the result of mean specific current i_m of the constant current passed in the anodic and cathodic scans for reduced and as- dealloyed np- Au samples as a function of measurement scan rate ν.

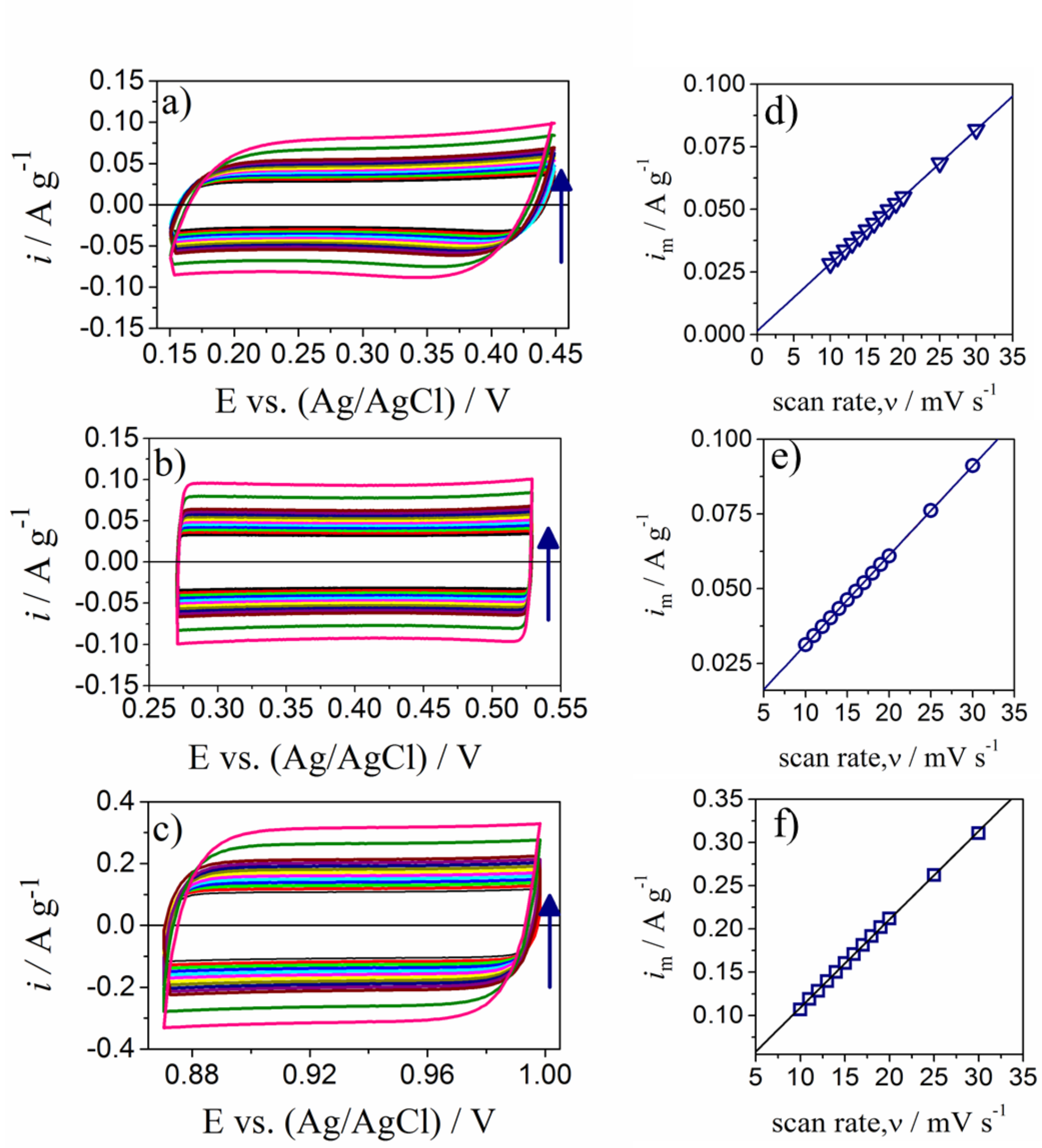

Fig. 4.7 Room temperature cyclic voltammograms CVs of specific current *i* versus electrode potential *E* versus pseudo Ag/AgCl electrode for np- Au in two distinct surface states, reduced and as dealloyed recorded in their double layer region at different scan rates 10 – 30 mVs^{-1}. a), b) CVs for reduced np- Au in 0.1M $HClO_4$ and 1M $HClO_4$, respectively c) CVs for as- dealloyed np- Au in 1M $HClO_4$ [91]. It is worth noting that the absolute *i* value increases as the scan rate increases in all the sub Figures. Mean specific current i_m obtained from room temperature CVs with scan rates *v*; the results for d) reduced np- Au in 0.1M $HClO_4$ and e) reduced np- Au in 1M $HClO_4$ and f) as- dealloyed np- Au in 1M $HClO_4$.

Figures 4.7 d) - f) shows i_m versus scan rate curves obtained from the room temperature cyclic voltammograms depicted in Figures 4.7 a) - c). Figure 4.7 d) and e) represent the results for reduced np- Au in 0.1M $HClO_4$ and 1M $HClO_4$ and Figure 4.7 f) represent the results for as- dealloyed np- Au in 1M $HClO_4$. It is seen that all the three i_m versus ν curves in Figure 4.7 d-f) are linear. As the quantity of double layer charge δQ_{dl} transferred across the electrode surface is directly proportional to the surface atoms density, the value of specific capacitance C_S for the np- Au samples can be determined by dividing the slope obtained from the linear regression of i_m on the variable ν in Figures 4.7 d) - f) by mass m of the sample. In order to verify, whether the determined surface area value in np- Au samples is reasonable, the cyclic voltammetry studies were performed on a planar Au foil (purity 99. 99%) in its double layer dominant potential region. The specific-mass surface area α_m value for planar Au obtained from the analysis of the cyclic voltammograms yields 2.725 x 10^{-4} m^2g^{-1}, which is in close agreement with its geometrical surface area α_g having a value of 2.688 x 10^{-4} m^2g^{-1}. The consistency in the data between α_m and α_g values for planar Au emphasizes the validity of double layer capacitance measurement method for the purpose determination of surface area for nanoporous Au samples.

4.4.2. Evolution of specific-mass surface area with temperature

Temperature dependent specific-mass surface area α_m value for as- dealloyed np- Au and reduced np- Au samples has been determined from the specific capacitance, C_S values. The microstructure results are discussed in chapter 3 reveals that nanoporous Au is highly sensitive to the surrounding temperature. Thermal effects are therefore important in the design and use of nanoporous metals at elevated temperatures. The results obtained are summarized in Table 4.1 and in Figure 4.9. It must be mentioned that the specific surface area, α_m value for as- dealloyed np- Au is significantly larger compared to that obtained for reduced np- Au. Here, it is important to note that, there is a systematic decrease of true surface area of np- Au during desorption of oxygen containing adsorbed species in as- dealloyed np- Au, inferred from Figure 4.3.

Based on the above results and the knowledge acquired from the literature, it is emphasised that in an aqueous electrochemical environment, the diffusivity of Au atoms in oxidized Au surface is lower as compared to that of a reduced clean Au surface [100]. This phenomenon is consistent with electronic theory which explains that the solid surfaces exhibit different surface states in terms of electronic screening. Let us consider a positively charged dipole covered metal surface with weak electronic screening. The bond strength between the surface metal atoms is expected to decrease due to the reduction in conduction electron density. In such a scenario, the excess charge that accumulates at the electrode surfaces redistributed towards the inner bonds and populates it into the bonding/anti-bonding orbital [122]. This supports the notion that the highly efficient electronic screening on clean metal surfaces tends to increase surface diffusivity as well as bond strength among surface metal atoms [122,125].

While the above arguments lend strong support to the notion that the capacitive charging behavior in np- Au with different surface state can be understood in terms of their surface diffusivity, it may be worthwhile to find out the variations of the specific capacitance C_S and the specific-mass surface area α_m values in as- dealloyed and reduced np- Au samples with temperature. Cyclic voltammograms were recorded on as- dealloyed np- Au and reduced np- Au samples at various temperatures in the temperature range 298 - 363 K in their double layer potential region. It must be mentioned that the temperature dependent double layer capacitance results are discussed. This discussion intends neither to elucidate the mechanism involved in the electrochemical potential variations at the double layer interface nor to verify the double layer theories. The investigations are rather directed towards unraveling the variation of important surface parameters like specific capacitance C_S and specific-mass surface area α_m, in as- dealloyed and reduced np- Au samples with temperature. Figures 4.8 a) – c) show the i_m versus scan rate curves for as-dealloyed np- Au in 1M $HClO_4$, reduced np- Au in 1M and 0.1M $HClO_4$ electrolytes at various temperatures. The symbols □, ■, ◇, ▼, ✶, ○ in the Figures 4.8 a) – c) identify the measurement temperatures 298, 323, 333, 343, 353, 363 K, respectively.

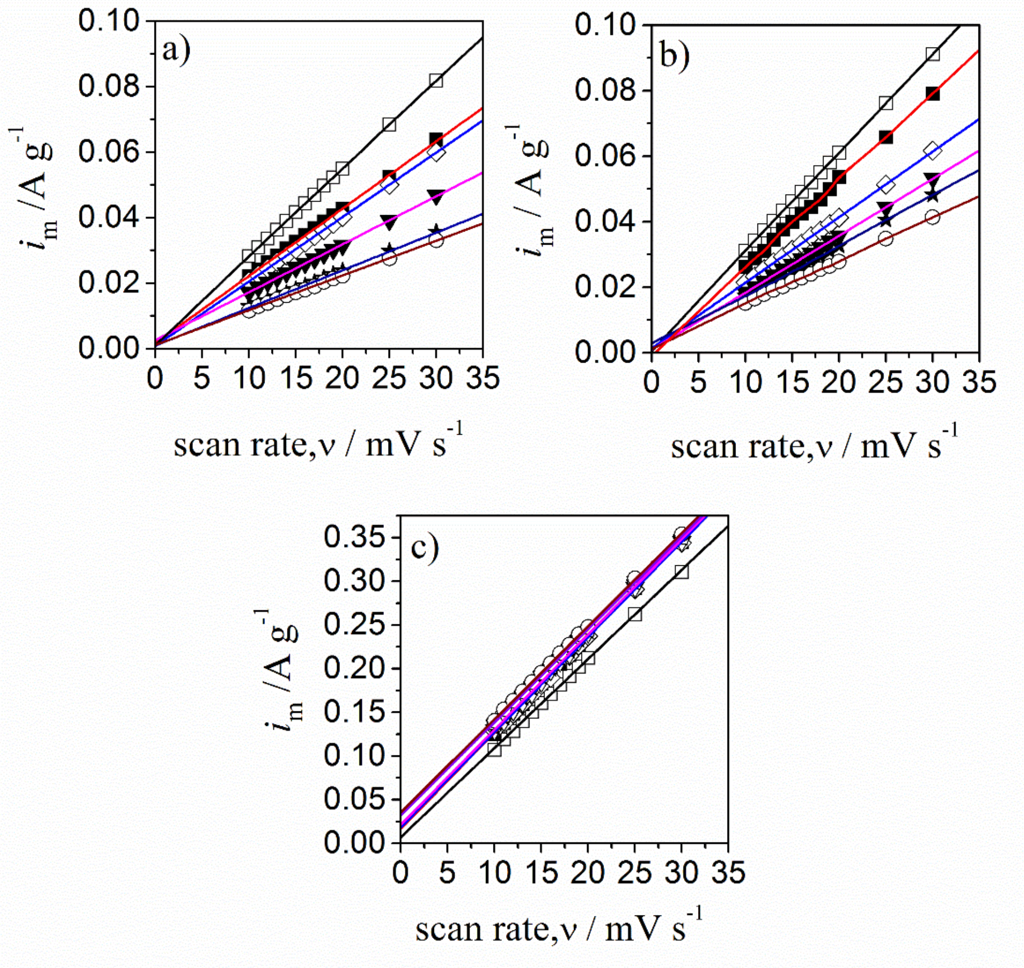

Fig. 4.8 Mean specific current i_m obtained from the cyclic voltammograms (CVs) for reduced np- Au and as- dealloyed np- Au in $HClO_4$ at various temperatures. (a), (b) Mean specific current i_m versus scan rate ν results for reduced np- Au in 1M $HClO_4$ and 0.1M $HClO_4$, respectively, at different temperatures below 363 K. (c) Mean specific current i_m versus scan rate ν results for as- dealloyed np- Au in 1M $HClO_4$ at various temperatures below 363 K. The symbols □, ■, ◇, ▼, ✶, ○ in the Figures a) – c) indicate the measurement temperatures 298, 323, 333, 343, 353, 363 K, respectively.

Figures 4.9 a) and b) show the variations of specific capacitance C_S value in logarithmic scale and specific-mass surface area α_m with reciprocal temperature, respectively. The symbols ▽, ○, □ in the Figures represent results for reduced np- Au in

0.1M $HClO_4$ reduced np- Au in 1M $HClO_4$ and as- dealloyed np- Au in 1M $HClO_4$, respectively. It is seen that ln (C_S) and α_m data for reduced np- Au samples decrease with increase in measurement temperature. This decreasing trend is consistent with the previous reports on temperature dependent variations of double layer capacitance in metal surfaces in contact with aqueous electrolytes [126]. No such noticeable temperature dependent variation in ln (C_S) and α_m data was observed for as- dealloyed np- Au sample.

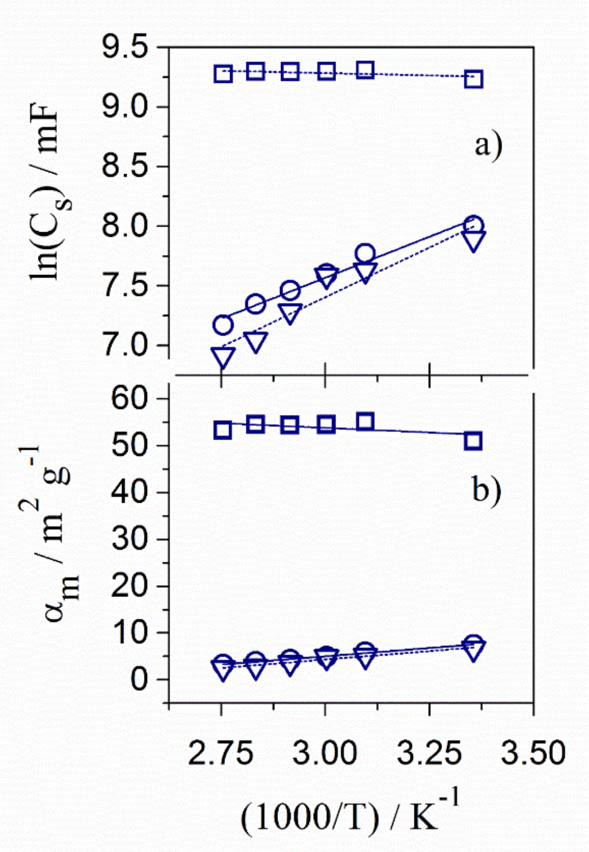

Fig. 4.9. Variations of (a) specific capacitance C_S and (b) specific-mass surface area α_m for np- Au in $HClO_4$ electrolyte with reciprocal temperature. The symbols ▽, ○, □ in the sub Figures (a) and (b) represent the results for reduced np- Au in 0.1M $HClO_4$ and reduced np- Au in 1M $HClO_4$ and as-dealloyed np- Au in 1M $HClO_4$ respectively

Table 4.1 Results of ligament diameter d, specific capacitance C_S, specific-mass surface area α_m, geometrical surface area αg for as- dealloyed np- Au in 1M $HClO_4$ and reduced clean metallic np- Au samples in 0.1M and 1M $HClO_4$, respectively, at room temperature.

Sample details	***d* (nm) from SEM**	**C_S (mF) (expt.)**	**α_m (m^2 g^{-1}) (expt.)**	**α_g (m^2 g^{-1}) (model)**
as- dealloyed np- Au 1M $HClO_4$	5 ± 1	10190	51.16	26.5
reduced np- Au 0.1M $HClO_4$	20 ± 2	2680	6.69	6.63
reduced np- Au 1M $HClO_4$	19 ± 2	2990	7.67	7.72

4.4.3. BET surface area in np- Au

Figure 4.10 a) shows two numbers of nitrogen adsorption/desorption isotherms recorded on a 400 mg as- dealloyed np- Au sample. These isotherm curves were obtained after degassing the sample for 2 hrs at 298 (indicated by black line) and at 323 K (indicated by navy blue line). The closed and open circles in the isotherms represent adsorption and desorption branches, respectively. The average ligament diameter of these samples determined from the analysis of SEM images is 5 ± 1 nm and 5.5 ± 2 nm, respectively. The BET surface area characterization shows the isotherms obtained are of the type IV according to the classification scheme of International Union of Pure and Applied Chemistry IUPAC. It is seen that the adsorption curve in these isotherms terminates almost at a relative pressure value p/p_0 of equaling-unity. This indicates the complete filling of nitrogen adsorbed atoms inside the pore capillaries. The BET surface area in np- Au was deduced from the initial linear part of the isotherms ($0.05 < p/p_0 < 0.35$). The slope and the intercept values obtained from the respective p/V_{ads} (p_0-p) versus p/p_0 linear curves are shown in Figure 4.10 b). These were used for the determination of BET surface area.

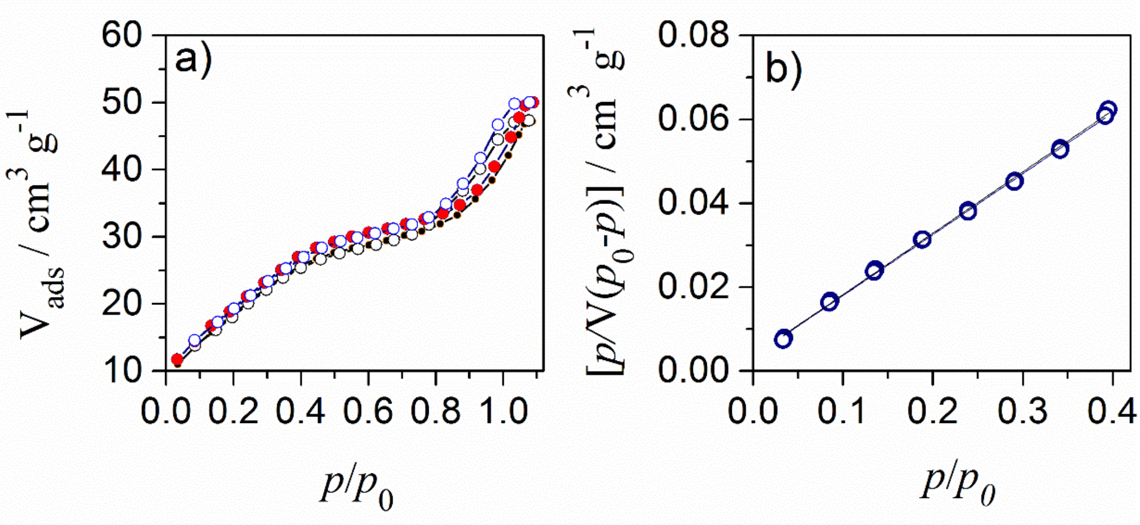

Fig. 4.10 a) Two numbers of nitrogen adsorption/desorption isotherms recorded on a 400 mg as- dealloyed np- Au. The closed and open circles in the isotherm curves represent the adsorption and desorption branches, respectively. b) Linear part of the low relative pressure nitrogen adsorption curves obtained from the isotherms in sub figure (a). The slope and intercept obtained from the best linear fit of the data as shown in the Figure were used to determine the BET surface area.

4.4.4. Geometrical and specific-mass surface area with ligament diameter

We follow an analytical approach to verify the specific-mass surface area α_m in np- Au samples by combining the geometry of porous - ligament assembly coupled with the ligament diameter *d*. We used a ball–stick model [127] for the determination of the geometrical surface area, α_g of porous – ligament network assembly in np- Au. A drawing as shown in Figure 4.11 provides a schematic view of the geometrical ball-stick (B-S) model. With this configuration, we calculate the geometrical surface area α_g for 30 % dense Au structure from the known material density 19.3 g cm^{-3} and from the surface area A_g for single ball-stick structure,

$$A_g = 4\pi r^2 + 3(2\pi rl + 2\pi r^2) + 24\left(\frac{rx}{2}\right) \tag{4.12}$$

R denotes radius of the spherical node. *l* denotes the length of the ligament and it is equal to *L-2R*. *r* is the radius of the ligament and *x* is the area under the node-ligament interconnected. The first, second and third terms in the right hand side of the equation corresponds to the area of spherical node and area of ligament region which shares each node and area of curved ligament-node in interconnected region. The important geometrical control parameters in nanoporous metals viz number of ligament interconnects, ligament diameter and aspect ratio of the ligaments (ratio of ligament length l to ligament diameter d) were adjusted for a constant ratio of ligament radius to node radius √(2/3) to find the matching geometrical surface area α_g to the experimentally measured specific-mass surface area α_m. We find from the analysis that the specific-mass surface area α_m and the geometrical surface area α_g values converge closely for the ligament aspect ratio l/d value of 1.33 and in a sharing of each ligament with two nodes.

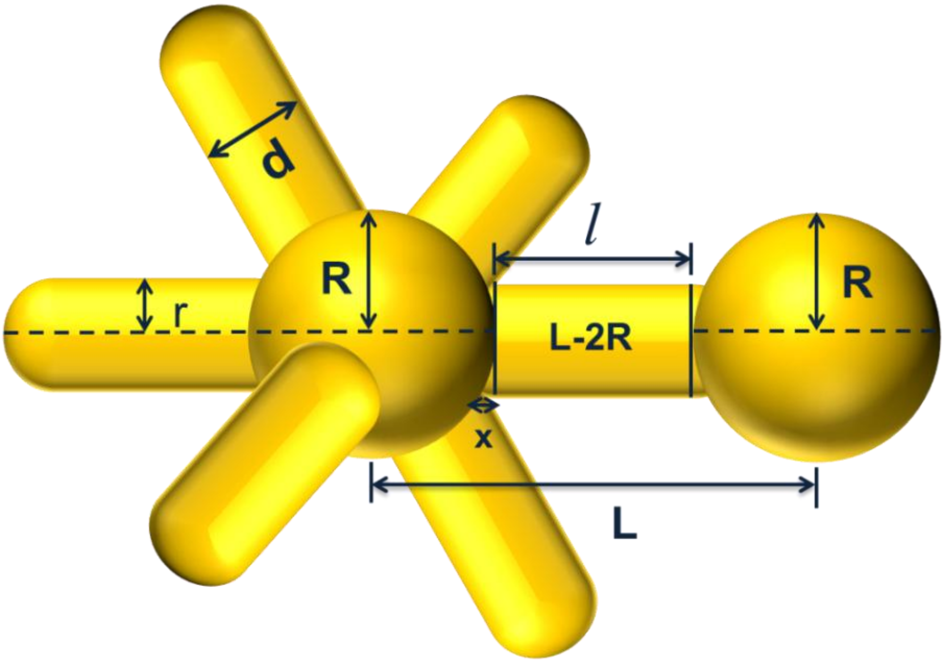

Fig. 4.11 Schematic view of a single ball-stick structure. R denotes radius of the spherical node. $l = L\text{-}2R$ is the length of ligament that touches node surface. L is the length of ligament from the centre of two interconnected nodes. r $(= d/2)$ is the radius of ligament. x is the area under the node-ligament interconnects which is equal to $(1\text{-}1/\sqrt{3})\ R$.

Figure 4.12 a) shows the evolution of microstructure in as- dealloyed np- Au and reduced np- Au at various temperatures. The left column in the figure represents the SEM images for the as- dealloyed np- Au and the right column in the figure represents the SEM images for reduced np- Au samples. The SEM images of as- dealloyed and reduced np- Au samples were taken after the double layer experiments at various temperatures. It is seen that the SEM images for all the heat-treated np- Au samples show the characteristic nanoporous microstructure of bicontinuous interpenetrating pores and ligaments [2]. The changes in the ligament diameter *d* with heat treatment were obtained from the analysis of SEM images and the results are shown in Figure 4.12 b).

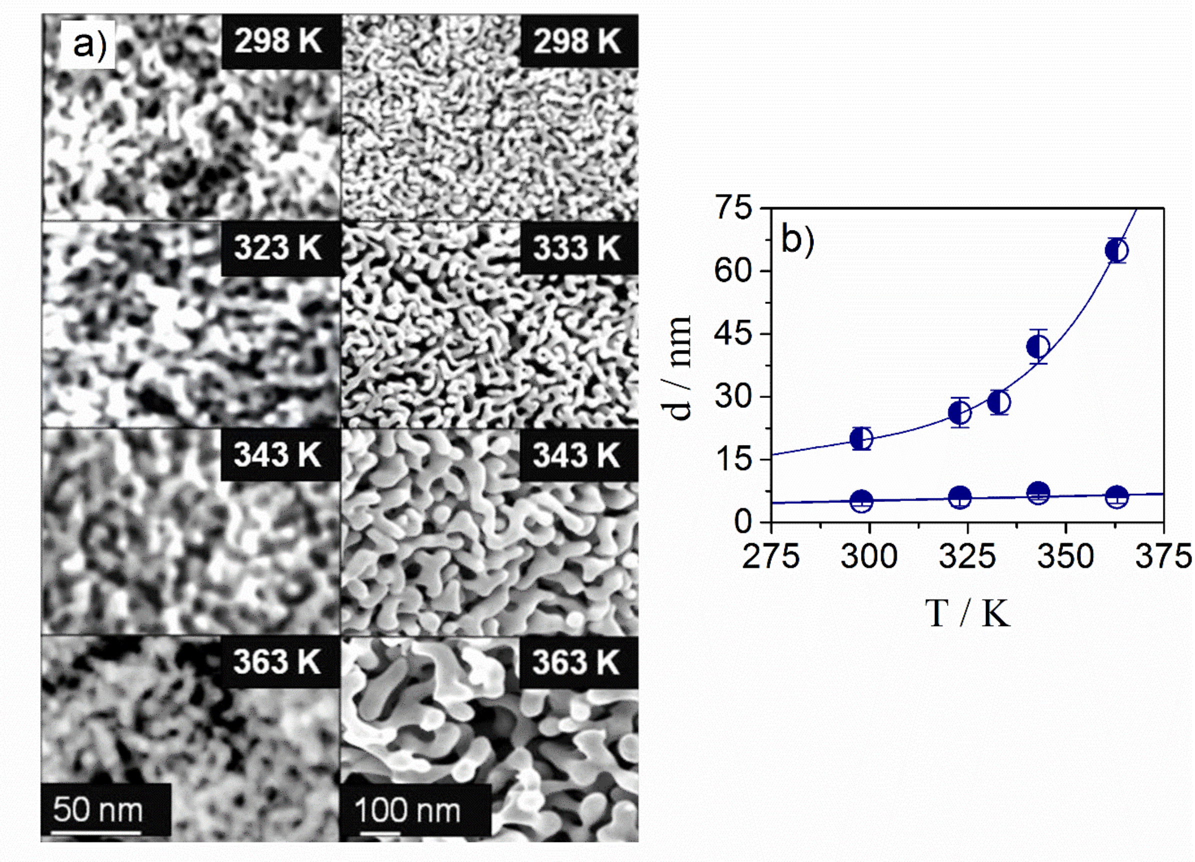

Fig. 4.12 a) Evolution of ligament-porous microstructure in as- dealloyed np- Au (images in left column) and reduced clean metallic np- Au (images in right column) at various temperatures below 363 K. b) Results of temperature dependent variations of ligament diameter *d* in reduced np- Au (symbol ◐) and in as- dealloyed np- Au (symbol ◒) samples obtained from the analysis of SEM images.

Since the structure size is a fundamental surface parameter and enables one to determine the surface area of solids, we plotted the specific-mass surface area α_m and geometrical surface area α_g data for both as- dealloyed and reduced np- Au samples as a function of ligament diameter *d* as shown in Figure 4.13. The symbols ◓ and ◐ in the Figure 4.13 represent the specific-mass surface area α_m for as- dealloyed and reduced np- Au samples, respectively. The continuous solid line represents their geometrical surface area α_g obtained using the ball-stick model. The results summarized in Figure 4.13 suggest that irrespective of different nature of the surfaces (as- dealloyed or reduced) the specific-mass surface area α_m and the geometrical surface area α_g values increase with the inverse size of ligament diameter. This behavior [cf. Figure 4.12] is found to be similar to the size dependent surface area results reported for other nanocrystalline and nanostructured materials [128]. Figure 4.13 contains also the BET surface area results on two as- dealloyed np- Au samples of mass 239 mg and 400 mg (indicated by symbols ☆ and ⊕, respectively). In addition, the BET surface area results on three different np- Au samples [1,96] (indicated by symbol ⊡) are also shown in the Figure 4.13.

According to the literature reports, oxidation process in clean metal – electrolyte interface consists of two successive charge transfer steps with intermediate formation of one electron transfer product of M $(OH)_n$ by a charge transfer reaction, $OH^- + M \leftrightarrow M - OH_{ads} + e^-$ [114,129]. Since simultaneous transfer of two electrons being unlikely during the formation of electrochemical surface oxidation on clean metals, we have resorted to use adsorption/desorption of OH_{ads} species based on electrochemical cyclic voltammetry for further validation of the np- Au ligament size dependence of surface area. Adsorption/desorption of OH_{ads} on the pore surfaces in reduced np- Au was carried out by recording the cyclic voltammetry scan between 0.3 and 0.95 V at different temperatures below 363 K to determine the net charge $\delta Q_{OH(ads\text{-}de)}$ transferred with temperature. This charge transfer corresponds to OH adsorption/desorption reaction in reduced np- Au having ligament diameter *d*. For estimating the magnitude of charge transfer $\delta Q_{OH(ads\text{-}de)}$, the current due to pure electrostatic charging that extends over the electrode surfaces during the adsorption/desorption processes is subtracted from the total current passed across reduced np- Au. The adsorption/desorption of OH_{ads} species on Au surface being an one electron process [114], the magnitude of charge transfer $\delta Q_{OH(ads\text{-}de)}$ could be successfully used to obtain specific-mass surface area α_m of 10.4 mg reduced np- Au. The symbol ► in Figure 4.13 represents the specific-mass surface area α_m of reduced np- Au determined using the cyclic voltammetry results of OH adsorption/desorption events as a function of ligament diameter *d*.

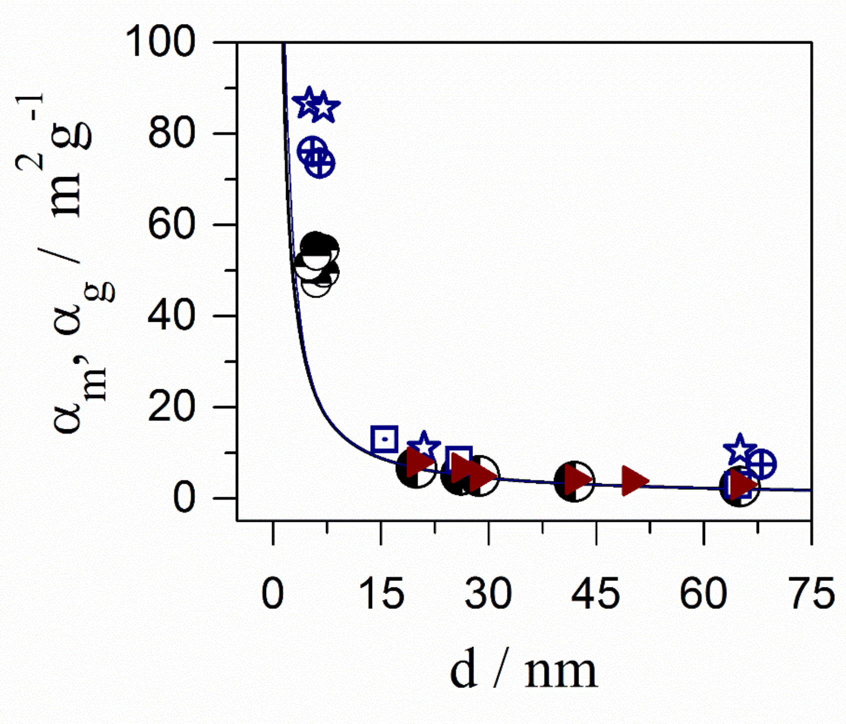

Fig. 4.13 A plot of specific-mass surface area α_m and geometrical surface area α_g versus ligament diameter *d* for np- Au. The symbols ◓ and ◐ and the continuous solid line represent the specific surface area α_m for as- dealloyed, reduced np- Au samples and the geometrical surface area α_g obtained using the ball-stick model, respectively. The symbols ☆ and ⊕ represent the BET surface area data on 400 mg and 239 mg as- dealloyed np- Au samples degassed in a dynamic vacuum at 273, 328, 383 and 523 K. The symbol ⊡ represents the BET data of np- Au reported in the literature [1, 40]. The symbol ► represents the specific-mass surface area of a reduced np- Au sample obtained from the process of adsorption/desorption of OH_{ads} species on pore surfaces in reduced np- Au.

It is shown in Figure 4.13 that the BET surface area value in np- Au decreases with ligament diameter d and the decreasing trend is found to be similar to the variation of α_m obtained from the capacitance ratio method. However, the surface area values obtained from these two methods deviate significantly for ligament diameter below 15 nm. A systematic study of above described and the documented literature report [115] suggests that the discrepancy in the surface areas obtained from BET and double layer capacitance methods for smaller ligament dimensions (below 15 nm) must be due to experimental uncertainty in the measurements. The most plausible explanation for this inconsistency in the specific-mass surface area values below the ligament diameter 15 nm could be due to the generation of micro cracks due to mechanical stress [51,96]. For np- Au samples with ligament diameter beyond 15 nm, the α_m values obtained from all the three experimental methods overlap with the geometrical surface area α_g results (cf. Figure 4.13). The consistency with the geometrical ball-stick model and comparable α_m values exhibited at ligament dimensions beyond 15 nm confirm that ligament-pore microstructure and chemical surface state in np- Au are important control parameters needed for quantifying specific surface area of np- Au architecture. This architecture consists of continuous interpenetrating Au ligament networks that yield a three-dimensional porous structure.

Here, it is worth mentioning that the temperature dependent capacitance (cf. Figure 4.9) of as- dealloyed np- Au with oxygen containing adsorbed species shows distinctly different trend on compared to reduced np- Au surfaces, with respect to charge development at the Au-electrolyte interface. This difference in the temperature dependence of specific capacitance C_S behavior for as- dealloyed and reduced Au surfaces is one of the possible diagnostic tools to understand the effect of oxygen adsorbed species at the metal-electrolyte interfaces to the modified materials properties.

4.5. Conclusions

In summary, we demonstrate that the electrochemical double layer capacitance ratio method accurately determines the temperature dependent variation of specific capacitance C_S and specific-mass surface area α_m in nanoporous Au in its two distinct surface states, as dealloyed and reduced clean metallic. It is interesting to note that the serendipitous property in as- dealloyed np- Au does not change its C_S and α_m values, suggesting that the adsorbed oxygen containing species are weakly bonded with Au during the evolution of nanoporous architecture with temperature. This phenomenon in the pore surfaces prevents ligament coarsening upon heating. This observation is in contrast to the pronounced ligament coarsening with temperature that exists on reduced clean metallic np- Au. Though the as- dealloyed np- Au samples can have pronounced anti-coarsening effect with temperature, an in-depth theory and experimental knowledge on temperature dependent coarsening phenomenon in nanoporous Au in the presence of different dipole interactions is essential to promote np- Au materials for high temperature catalytic and energy conversion applications.

Chapter 5

Positron diffusion behavior in nanoporous Au

Positron annihilation spectroscopy is an applied nuclear physics non-destructive experimental technique to study the vacancy like defects (atom fraction of 10^{-7}-10^{-4}) and micro voids in solids. Positron lifetime, Doppler broadening line shape measurements, angular correlation of annihilation photons are the three major techniques available in this positron annihilation spectroscopy studies. The positron lifetime is commonly used to study the open volume type of defects in materials. Low energy positron beam Doppler broadening spectroscopy technique is used to study open volume defects distributed in near surface region (<1µm). In this chapter evolution of defects during the formation of nanoporous Au and its annealing behavior will be discussed using the low energy positron beam Doppler broadening spectroscopy technique. Study of nanoporous metals like np- Au using the positron annihilation spectroscopy offers an opportunity for understanding the positron interaction with defects in the nanoporous Au assembly.

5.1. Introduction

As discussed in the previous chapters, np- Au has two-phase microstructure consisting of interpenetrated nanometer sized metallic Au ligament networks with three-dimensional continuous pores [2,5,14]. The three dominant interests which motivate me to study the positron annihilation in np- Au are as follows. First, to understand the mechanism for the evolution of bi-continuous open pore structures with ligaments of nanometric dimensions during the electrochemical dissolution process and how these structures coarsen with thermal annealing [3]. An understanding of this will help in tailoring the nanoporous morphology through additional alloying elements or thermal annealing. Second, to find the effect of open volume defects such as vacancy and stacking fault tetrahedra (SFT), that are retained inside the ligaments during electrochemical dealloying [130], to the positron diffusion in the nanoporous Au ensemble [21]. To find the mechanism of coarsening and positron interactions in the np- Au ligaments, low energy positron beam measurement studies have been carried out. Third, despite progress has already been made on the investigations of positron diffusion behavior in dense metallic solids [131,132], no exact results have been reported on the positron diffusion behavior in nanoporous metallic counterparts.

It is the purpose of the present chapter to explore the role of defects, if any, on the evolution of nanoporous Au morphology using positron lifetime experiments and the positron diffusion behavior in np- Au with ligament diameter using low energy positron beam Doppler broadening spectroscopy.

5.2. Experimental procedure

The synthesis procedure for np- Au was discussed in chapter 2. In brief, the np- Au samples used for the study were made by electrochemical dealloying of arc melted $Ag_{75}Au_{25}$ binary alloy [3,20]. Disc shaped np- Au samples with dimensions ~ 1.5 cm in diameter and ~ 0. 2 cm in thickness were used for this study. The positron annihilation spectroscopy has been widely used to study vacancy, micro-void and grain boundary defects in metallic materials [133,134]. The analysis of low energy positron beam experiments in terms of positron diffusion length and positronium fraction, $f_{3\gamma/2\gamma}$ provides an opportunity to obtain insight on the positron behavior in nanoporous Au and depth-wise defect distribution in Au ligament - pore network. Low energy positron beam experiments were performed on np- Au as a function of annealing temperature. Positrons are produced in an encapsulated 50 mCi ^{22}Na radioactive source and moderated in a thin (thickness ~1 μm) single crystal W(100) foil in transmission geometry [135]. The positron beam diameter collimated for implantation on the samples was 8 mm. In order to investigate the positron annihilation at various positron incident energies and to identify the defect environment as a function of sample depth, Doppler broadening line shape spectra were recorded with the variation of positron beam energy in the range 0.2 - 15 keV. High-purity Ge detector having an energy resolution of 1.4 keV at 662 keV gamma line of Cs^{137} was used for the data collection.

5.3. Determination of positron diffusion length

5.3.1. Positron trapping model

Positrons capture in open-volume defects during diffusion in the material, is used to demonstrate in the simplest trapping model [24]. After thermalization process, the diffused positron may annihilate in the defect-free bulk of the samples with the annihilation rate λ_b. If the concentration of the open-volume defect is sufficiently high, a certain fraction of positrons diffuse through the samples may be trapped in the defects with the trapping rate κ_d. The rate equations used in the positron trapping model are described in chapter 2. It is considered that the positron capturing process occurs only after thermalization and the trapped positron does not detrap from the defects. This assumption satisfies for open-volume defects [133]. Concentration of open volume defects calculated by positron diffusing through sample and trapped with the trapping rate, κ_d.

$$\kappa_d = \mu_d C \tag{5.1}$$

where μ_d is the specific trapping coefficient and C is the defect concentration.

The scheme of positron trapping model is shown in Figure 5.1. When using two state trapping model for the data analysis, the first lifetime component τ_1 equals to the bulk lifetime τ_b minus the contribution from trapping rate κ. The second lifetime can then be allocated to a defect with the lifetime τ_d. In more complex materials more than one kind of defect can be expected. Figure 5.1 is shown positron trapping model with two distinct defect states. If the bulk lifetime cannot be separated numerically from one of the defect lifetime, then the following cases can be distinguished according to Hautojarvi [64].

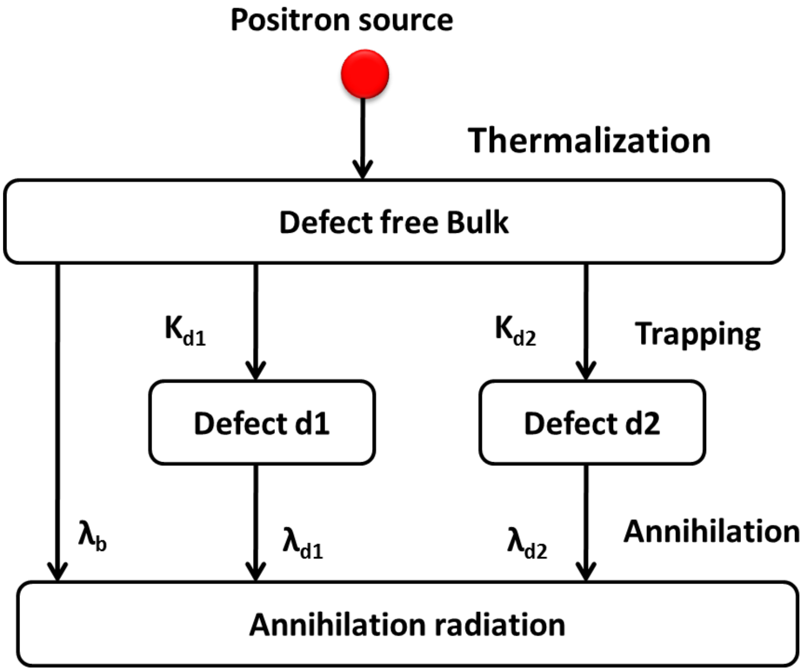

Fig. 5.1 Scheme of the two state positron trapping model with more than one defect type. After Thermalization, the positron may annihilate from the defect-free bulk with the annihilation rate λ_b. Alternatively they may be trapped in the defect with the trapping rate κ_d and annihilate with the smaller annihilation rate λ_d.

(1) For saturation defect where no positron in free state can be detected, all positrons annihilate in a defect (trapped state). The trapping rate is given by,

$$\frac{\kappa_1}{\kappa_2} = \frac{I_{1exp}}{I_{2exp}} \tag{5.2}$$

I_{1exp} and I_{2exp} are the intensities of resolved lifetime components τ_{1exp} and τ_{2exp} respectively obtained from experiment. κ_{d1} and κ_{d2} are trapping rates for two types of defects

(2) If τ_{1exp} consists of two lifetime components (bulk and one defect) and τ_{2exp} is well separated. This is the case when simultaneously point defects and defect clusters exist. The lifetime components are given by

$$1/\tau_1 = \lambda_b + \kappa_{d1} + \kappa_{d2} = \lambda_1 \tag{5.3}$$

$$1/\tau_2 = 1/\tau_{d1} = \lambda_2 \tag{5.4}$$

$$1/\tau_3 = 1/\tau_{2exp} = 1/\tau_{d2} = \lambda_2 \tag{5.5}$$

With intensities

$$\boldsymbol{I_1 = 1 - I_2 - I_3} \tag{5.6}$$

$$I_2 = \frac{\kappa_{d1}}{\lambda_b - \lambda_2 + \kappa_{d1} + \kappa_{d2}} \tag{5.7}$$

$$I_3 = I_{2exp} \tag{5.8}$$

And trapping rates will be

$$\kappa_{d1} = \frac{\tau_{1exp}(\lambda_b - I_3\lambda_3) - I_{1exp}}{\tau_2 - \tau_{1exp}} \tag{5.9}$$

$$\kappa_{d2} = \frac{I_{2exp}}{I_{1exp}}(\lambda_b - \lambda_3 + \kappa_{d1}) \tag{5.10}$$

Positron diffusion length L_+ is calculated from the above trapping model findings. The positron diffusion length is limited due to the finite lifetime of positron in defect-free bulk, τ_b

$$L_+ = \sqrt{\tau_b D_+} \tag{5.11}$$

In the presence of defects in as- dealloyed nanoporous Au, the positron trapping rate, κ_d was taken into account, resulting in the effective positron diffusion length L_{eff} , will be,

$$L_{eff} = \sqrt{\frac{D_+}{\lambda_b + k_d}} \tag{5.12}$$

where D_+ is the positron diffusion coefficient, λ_b is the positron annihilation rate in defect free state site and κ_d is the positron trapping rate in defect site.

5.4. Results and Discussion

Figure 5.2 shows typical microstructure results for np- Au with different ligament sizes. Scanning electron microscopy (SEM) was used to examine morphology evolution subsequent to different stages of ligament coarsening. Figures 5.2 a) – e) show the SEM images made on few selected nanoporous Au samples heat treated at a prescribed temperature in the range 298 - 1073 K. Figure 5.2 f) shows the mean ligament diameter d versus annealing temperature obtained from the analysis of the SEM images using the software ImageJ. It is seen that the ligament diameter increases with annealing temperature. The evolution of microstructure, e.g. ligament diameter d with coarsening, as summarized in the Figure 5.2 is important parameter since the present study correlates the positron diffusion limited processes in np- Au with ligament diameter d.

Results obtained from the microstructure investigations revealed that the ligament-pore network assembly in np- Au is monolithic [20,130]. In this skeletal monolithic framework, it becomes important to understand the variation of positron diffusion length L_{eff} with ligament diameter d as the annealing temperature increases.

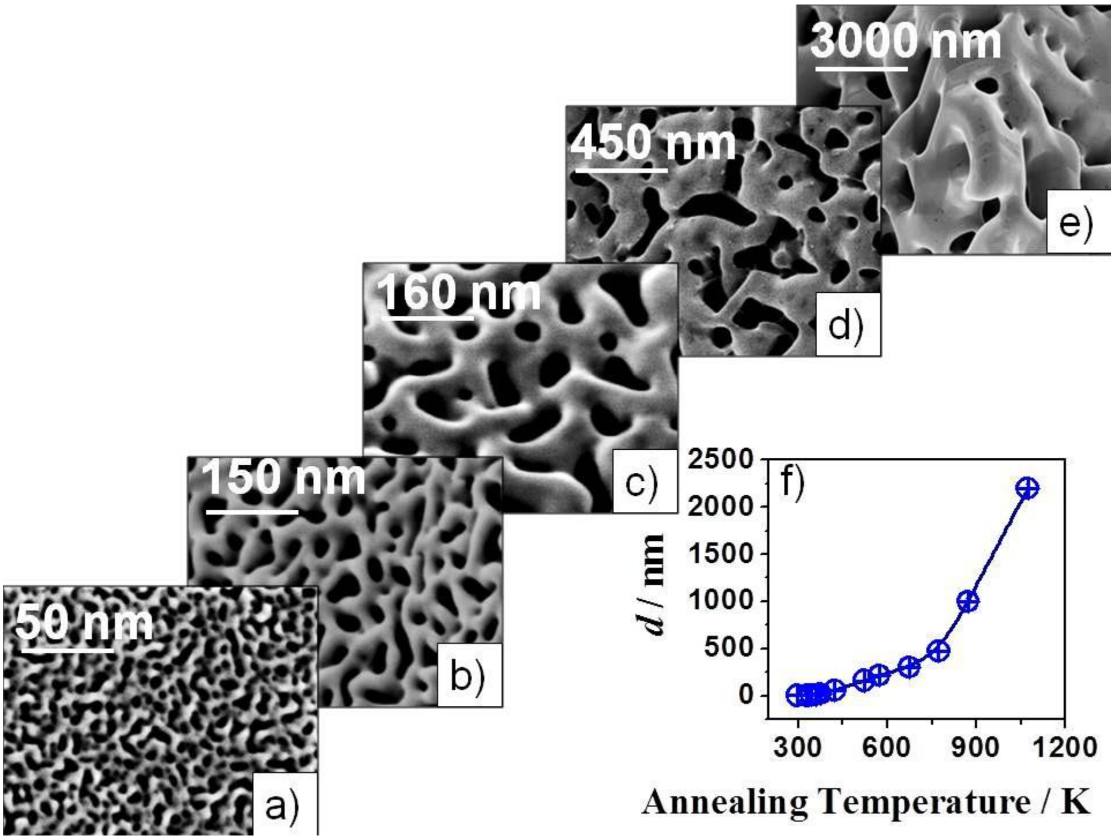

Fig. 5.2 Scanning electron microscopy results of np- Au with temperature treatment. The as- dealloyed np- Au samples were heat treated at various temperatures. a) 298 K, b) 398 K, c) 428 K, d) 523 K, e) 873 K. f) The mean variation of ligament diameter *d* for np- Au with annealing temperature.

5.4.1. Low energy positron beam Doppler broadening spectroscopy measurements

Positron lifetime results in as- dealloyed np- Au reported in ref. [3] have identified two lifetime components with values τ_1 ~ 209 ps and τ_2 ~ 439 ps. The lifetime τ_1 is associated with the annihilation of positrons in vacancies present in the ligaments and the lifetime τ_2 corresponding to the annihilation of positrons at the ligament-pore interface. It was shown that these lifetime values in np- Au change systematically with annealing temperature, and in particular, the lifetime value corresponding to the annihilation at the ligament-pore interface shows signature of ligament instability [3,136]. In the following, we try to understand the implications of the above changes in lifetime parameters on the evolution of the morphology of np- Au with annealing. In the present study, we have carried out low energy positron beam experiments to investigate the evolution of defects, associated with the change in morphology of np- Au with annealing temperature. It must be mentioned that from a measurement of the Doppler broadened line shape parameter as a function of the incident positron energy, S(E_P), one is able to obtain information on the evolution of open volume defects with annealing temperature. Further, the S(E_P) variation is also amenable to extract information on the diffusion length of the positron in the medium, that is sensitive to the presence of defects [7]. Thus, in the present study, we follow the variation of the defect sensitive S - parameter and also estimate the variation of positron diffusion length to obtain insight on the evolution of defects with temperature in np- Au.

Figure 5.3 a) shows the typical positron beam Doppler broadening spectra for incident positron beam energy of 15 keV, obtained in as-prepared np- Au (symbol ○) compared with those in annealed at 473 K (symbol Δ) and 1073 K (symbol □) and defect free bulk Au (symbol *). It is seen in the Figure 5.3 a) that dominant changes that occur in the Doppler broadening spectra are at low momentum region where positron wave function in the localized vacancy state has a greater overlap with that of valence electrons. To understand the significance of the changes in the Doppler broadening spectra at lower momentum region, the peak line shape parameter (S - parameter) was estimated and plotted as a function of incident positron beam energy E_P as shown in Figure 5.3 b). S - parameter is defined as the ratio of counts in the central energy E_γ region of 511± 1 keV to the total counts under the peak energy E_γ range of 511± 10 keV.

The dependence of line shape S - parameter with positron beam energy E_P can be obtained from the fitting of data with sequence of different homogeneous layers using VEPFIT program [77]. The relative change in S - parameter values of np- Au with temperature annealing conveys information about defects contributing for positron trapping or positron annihilation sites $S(E_P) = \Sigma f_i(E_P)S_i$, where f_i is the fraction of positron annihilation in layer *i* and S_i is its characteristic S – parameter [7].

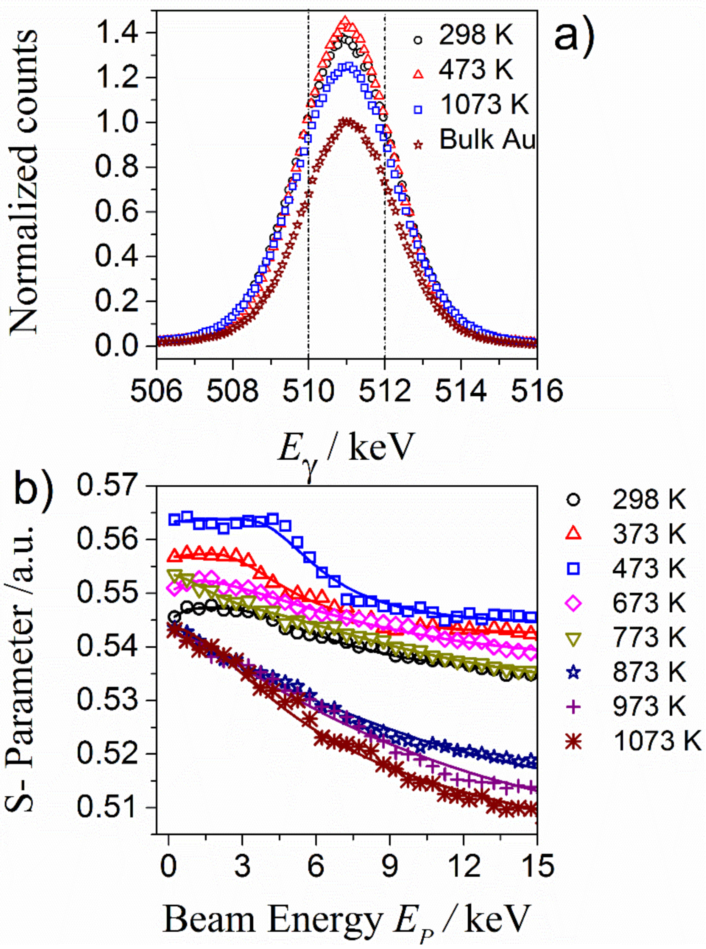

Fig. 5.3 a) shows the typical positron beam Doppler broadening spectra recorded at a beam energy of 4 keV in as-prepared np- Au (symbol ○) compared with those in annealed at 473 K (symbol Δ) and 1073 K (symbol □) and defect free bulk Au (symbol *). S - parameter is defined as the ratio of counts in the central energy E_γ region of 511± 1 keV to the total counts under the peak energy E_γ range of 511± 10 keV. Figure 5.3 b) shows the measured positron annihilation line shape S - parameter versus incident positron beam energy E_P for np- Au annealed at various temperatures. The dependence of line shape S - parameter with incident positron beam energy E_P is analyzed using the standard VEPFIT code [77].

Since the microstructure of np- Au comprises of an ensemble of three-dimensional interconnected nanometer sized interpenetrating ligament network with interconnected free volume, we used the frequently applied layer model [77] for the analysis of S(E_P) curves, depicted in Figure 5.3 b). Best fitting of the S(E_P) curves was achieved with two-layer component, with the first layer corresponding to annihilations in the near surface region and the second layer corresponding to the bulk of the np- Au. The solid lines in Figure 5.3 b) are the fits to the experimental data. In an attempt to understand the atomistic process involved in the variation of S - parameter with annealing temperature, we also include in Figure 5.4, the salient results from our earlier positron lifetime measurements [3]. Associated low energy momentum annihilation fraction with vacancies and voids in metallic systems is well established [137,138].

In Figure 5.4 a), we show the variation of the S - parameter value corresponding to the annihilations from the second layer, with annealing temperature. Owing to the lower momentum of positron annihilation in open volume defects [139,140], the increase in S - parameter with annealing below 473 K indicating that the vacancies that are originally present in the as- dealloyed np- Au start migrating and form a vacancy clusters/voids. In order to understand these results, we take the support of our earlier investigations on the variation of positron lifetime parameters with annealing temperature [3], and these are summarized in the bottom panel of Figure 5.4 a). The initial increase in S - parameter, as also the concomitant variation of $\tau_{2,}$ with annealing upto 473 K may be attributed to the growth of vacancy clusters arising due to the aggregation of thermally migrating vacancies, as this also coincides with the stage corresponding to a decrease in lifetime τ_1 with annealing temperature. Indeed the presence of encased voids in the ligament bulk and near to the proximity of ligament interconnects was reported in high resolution transmission electron microscopy studies on as- dealloyed np- Au [5]. It may be mentioned that early resistivity measurements on quenched Au – Ag alloys [141,142] have also indicated annealing of vacancies in this temperature with a migration energy of 0.85 eV. In support of the formation of vacancy clusters, we also present the results of TEM experiments on as- dealloyed np- Au, annealed at 363 K. HRTEM (LIBRA 200FE Zeiss) was used to obtain the TEM micrographs. The ligament structure can be discerned in low resolution micrograph shown in Figure 5.4 b), and the high resolution image in Figure 5.4 c), shows triangular contrast of ~ 3 nm, associated with stacking fault tetrahedra (SFT) defect structure [143]. It is seen that these SFTs are present in proximity to ligament interconnects.

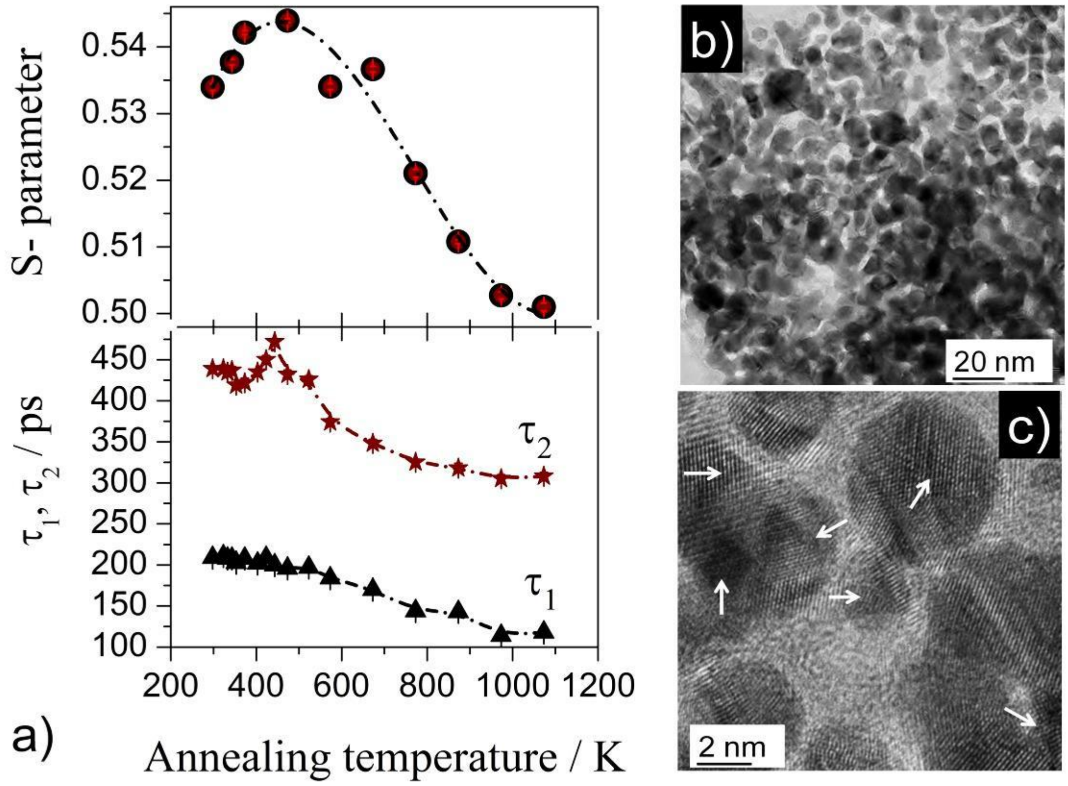

Fig. 5.4 a) Positron beam Doppler broadening S - parameter in np- Au (symbol ●) as a function of annealing temperature. Our earlier positron lifetime values τ_1 (symbol ▲) and τ_2 (symbol *) in np- Au with thermal annealing reported in Ref. [3] are shown in the bottom panel of the figure. Error bar values are within the width of the data points. Lines with short dash dot as shown in the curves are guide to eye. b) Low magnification TEM image of 363 K annealed np- Au. c) High resolution atomic resolution image taken from the selected area in sub figure b) showing an image of about 3 nm sized SFTs, identified by arrows.

When the annealing temperature exceeds 473 K, both S - parameter and lifetime τ_2 start decreasing [cf. Figure 5.4 a)]. It must be mentioned that in the annealing temperature interval (473 – 1073 K) at which the S- parameter decreases is in the temperature region where the variation of ligament diameter *d* becomes faster [cf. Figure

5.2 a)]. It is noted that this rapid decrease in the S - parameter and lifetime τ_2 coincides with the rapid increase in the ligament diameter [cf. Figure 5.2 a)] in the temperature range from 473 to 1073 K.

The above results on the annealing out of defects, associated with the rapid growth of ligaments, is in support of the large scale kinetic Monte Carlo simulations carried out by Erlebacher [136], that has indicated that the coarsening of ligaments involve complex changes in topology associated with the reduction of genus via both ligament pinch-off and void formation. Closure of the pores is also occurred partially in this annealing interval due to the creation of inter-ligament contacts [cf. Figure 5.2 c)]. These observations are close agreement with our previously reported ligament coarsening studies on np- Au which indicated that defects present in the ligaments play an important role for ligament coarsening [3,127].

In addition to obtaining the defect sensitive Doppler broadening line-shape parameter, S, the low energy positron beam experiments also provide an opportunity to evaluate the positron diffusion length that is influenced by the presence of defects. The effective positron diffusion length L_{eff} was extracted from the layer fittings of S(E_P) plot using the VEPFIT code [77]. Figure 5.5 a) shows the effective positron diffusion length L_{eff} values in np- Au as a function of annealing temperature**.** It is seen that initially there is a marginal decrease in the L_{eff} value up to 473 K, followed by a rapid increase as the annealing temperature increases, and finally reaches the value corresponding to annealed Au, viz., 120 nm, as indicated by the dotted line. The positron diffusion length in annealed Au was estimated using the relation $L_+ = \sqrt{D_+ \tau_b}$, where τ_b is the positron annihilation lifetime in annealed Au, and D_+ is the positron bulk diffusivity in Au at room temperature [144]. The variation of positron diffusion length with annealing temperature, shown in Figure 5.5 a), is consistent with the variation of S - parameter and lifetime [cf.

Figure 5.4 a)] in that it arises due to an initial growth of vacancy clusters upto 473 K, followed by their break up with the increase of annealing temperature.

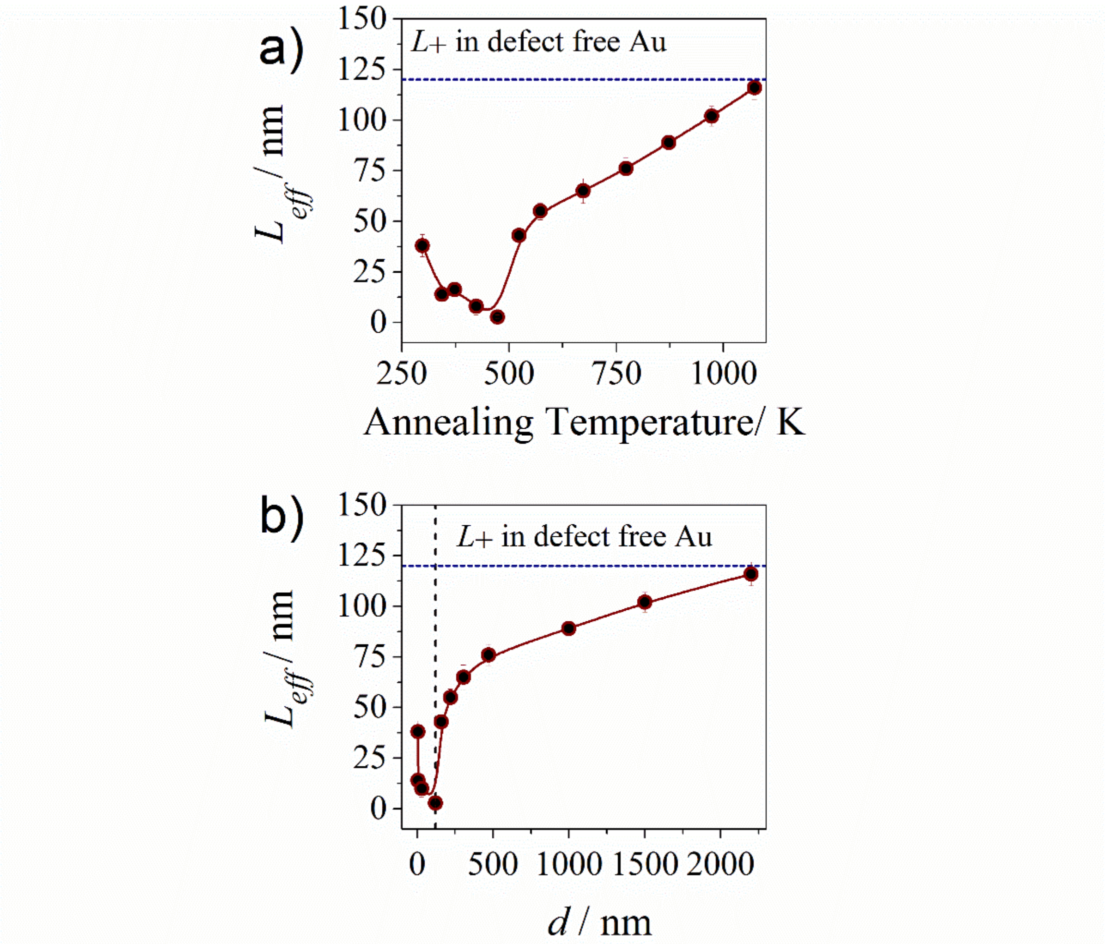

Fig. 5.5 a) Variation of positron effective diffusion length L_{eff} in np- Au as a function of annealing temperature. b) Variation of positron effective diffusion length L_{eff} in np- Au with ligament diameter *d*. The initial decrease changes to an increase for ligament diameters greater than the positron diffusion length in bulk, indicated as a vertical dashed line. Solid line as shown in sub figures a) and b) are guide to eye. Dotted line at L_+ =120 nm in sub figures a) and b), corresponds to the estimated positron diffusion length, $L_{+,}$ in bulk defect free Au.

Apart from providing results in support of the S - parameter variation on the evolution of defects with annealing temperature, the analysis of the low energy positron beam experiments in terms of the positron diffusion length provides an opportunity to obtain insight on the positron behavior in np- Au of varying diameter. This is presented in the following. In Fig, 5.5 b), we plot the variation of $L_{eff,}$ as a function of ligament diameter, using the results on the variation of ligament diameter with temperature from SEM measurements, as shown in Figure 5.2. In Figure 5.6, we plot the variation of L_{eff} with d on a logarithmic scale. It is seen that the positron diffusion length scales with ligament diameter d with a power law dependence $L_{eff} \propto d^{1/3}$. Also shown in Figure 5.6 is the positron diffusion length obtained from the lifetime data of Ref. 2 using the relation $L_{eff} = \sqrt{D_+/(\kappa+\lambda)}$, where κ is the defects trapping rate and λ is the annihilation rate of defects [70]. This is obtained by applying the two stage trapping model to the variation of τ_1 [cf. Figure 5.4 a)], as it straddles between 209 ps and the annealed value 116 ps.

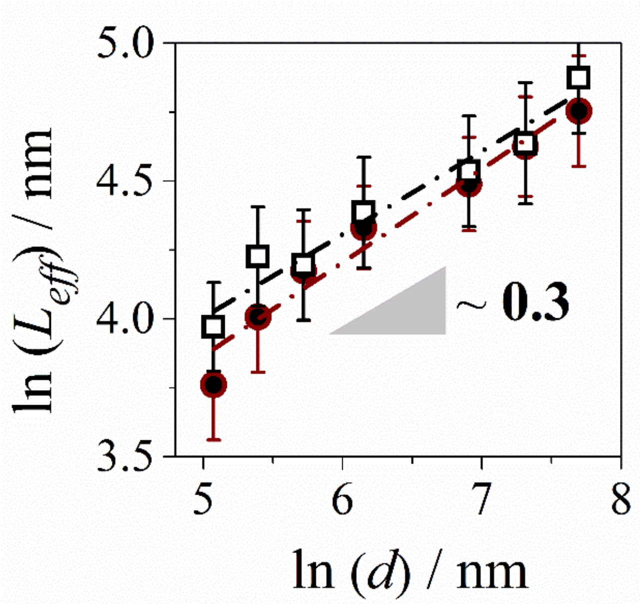

Fig. 5.6 Plot of ln (L_{eff}) versus ln (d) for np- Au obtained from Doppler broadening line shape measurement data (symbol ●) and from lifetime measurement data corresponding to average of vacancy and vacancy cluster/void defects (symbol □). Straight dash dot lines are best linear fit of the relation between L_{eff} and d with a slope of 0.3.

The present experiments on np- Au indicate that the positron diffusion length varies with the physical size of the sample, viz., the diameter of the ligaments, and scales as $d^{1/3}$. Basically, the underlying reason for the increase of the diffusion length, towards the bulk value of 120 nm is the decrease in density of vacancy defects, as the ligament grows with the increase of annealing temperature. The observed exponent of 1/3 can be rationalized as indicative of positron diffusion along the length of the ligaments, based on dimensional arguments, as indicated below. We first note that the positron diffusion length is given by $L_{+} = \left(D_{+}/(\kappa+\lambda)\right)^{1/2}$, where k is the trapping rate proportional to the vacancy concentration C_v, that decreases as the annealing temperature increases. Given that the positron trapping rate at vacancies is given by $\kappa = \mu C_v$, L_+ scales as $(C_v)^{-1/2}$. Assuming that the positron diffusion taking place along the length of the ligaments, the operative defect density controlling the diffusion length is the defects along the length l of the ligament, that is given by $C_v \sim \left(1/d^2 l\right)^{1/3}$, that in turn leads to $L_{+} \sim d^{1/3}$. Thus, the observed $d^{1/3}$ behavior of the positron diffusion length is indicative of one-dimensional diffusion along the ligament length l. This confining effect of positrons along the ligament length may be due to the confining potential felt by the positron at the surface of Au ligaments in np- Au.

Further support for this one dimensional diffusion of positrons in np- Au is obtained from the measurements of positronium fraction, as presented below. Information on positron diffusion in the medium can also be obtained in a low energy positron beam experiments by looking at the spectral signatures for three photon annihilations from positronium, which forms at the entrance surface by the back diffusion of impinging positrons. The fraction of impinging positrons that diffuse back to the entrance surface and annihilate as a positronium can be estimated from the measurement of the relative fraction, *f*, of the 3γ/2γ yields [139]. Figure 5.7 shows the 511 keV gamma-ray spectra region which is used for estimating of the positronium fraction, 3γ/2γ. *Z* is the total energy spectra counts and *P* is the photo peak energy spectra counts

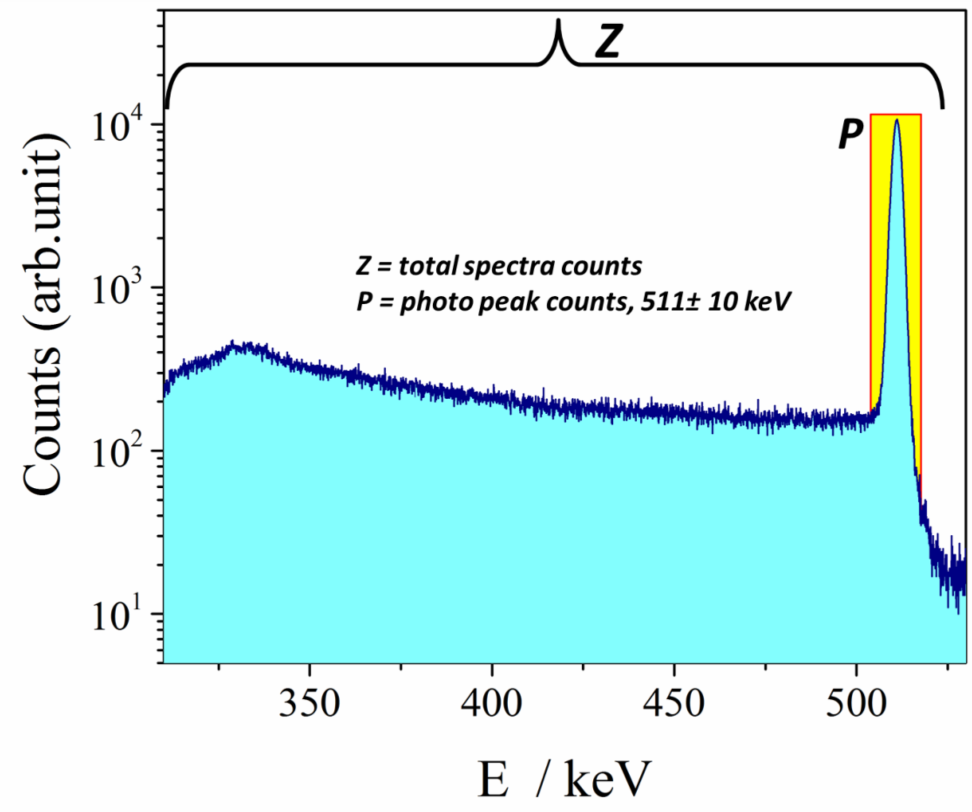

Fig. 5.7 The 511 keV gamma-ray spectrum measuring using HpGe detector. The region used for calculation of the positronium fraction. Z is the total energy spectra counts and P is the photo peak energy spectra counts.

We have monitored the positronium fraction f in all annealed np- Au samples by the analysis of γ-ray energy spectra according to the relation $f = (Z - P)/P$, where P is the peak counts from the Doppler broadened two gamma annihilation spectrum at 511 ± 10 keV, and Z is the integrated counts in the total annihilation gamma ray energy spectrum, corrected for Compton scattering and other background signals [7,70].

The results of the variation of $f_{3\gamma/2\gamma}$ with E_P are presented in Figure 5.8, for np- Au samples, annealed at various temperatures. It is seen that the variation of $f_{3\gamma/2\gamma}$ with E_P is nearly the same for all samples, including in a defect-free Au foil. The interesting observation is that the positronium fraction is same for all samples with diameters varying over a wide range, from a few nm to 2500 nm [cf. Fig 5.2], suggests that diffusion of positron is along the length of the ligaments. For otherwise, in np- Au having diameters, less than the bulk positron diffusion length of ~ 120 nm, thermalized positrons would have been emitted from the surface of ligaments, and the results of $f_{3\gamma/2\gamma}$ with E_P in Figure 5.8 would have qualitatively different behaviors for small and larger diameters. This is not seen, and in fact the variation of $f_{3\gamma/2\gamma}$ with E_P is similar, irrespective of the ligament diameter. It is seen that the variation of $f_{3\gamma/2\gamma}$ with E_P is nearly the same for all samples, including the bulk Au which is defect free. Thus, the experiments on the measurement of positronium fraction provide an independent evidence for the one-dimensional diffusion of positrons along the ligaments, and complement conclusion drawn from the scaling behavior, shown in Figure 5.6.

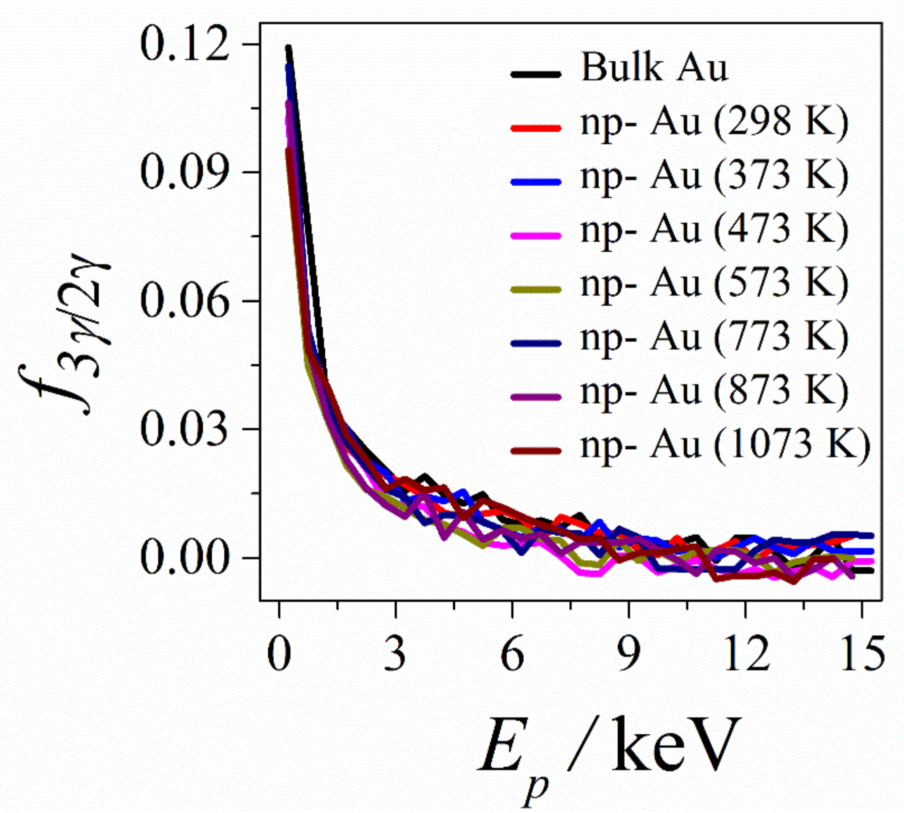

Fig. 5.8 Positronium fraction $f_{3\gamma/2\gamma}$ determined from Doppler broadening S - parameter in different annealed np- Au (color lines) as a function of positron beam energy in the range 0.1 to 15 keV. The measurement temperature was 293 K. The $f_{3\gamma/2\gamma}$ versus E_P behavior obtained for bulk Au is also depicted in the figure for comparison (black line).

5.5. Conclusion

The role of point defects to ligament coarsening process in np- Au and the positron diffusion behavior in nanoporous Au skeletal structure have been studied using low energy positron Doppler beam broadening spectroscopy measurements on np- Au. In low energy positron beam experiments on nanoporous Au, the variation of the defect sensitive Doppler broadening line shape parameter, S, is consistent with the earlier positron lifetime results. The low energy positron beam experiments have also been analyzed to extract the positron diffusion length. The variation of positron diffusion length with temperature correlates with the variation of Doppler broadening line shape S - parameter. The positron diffusion length increases with the ligament diameter, obtained from SEM measurements and scales according to $d^{1/3}$, that points to diffusion of positrons along the length of the ligaments. This is also substantiated by the measurement of positronium fraction, through 3γ/2γ experiments that is seen to be independent of the annealing temperature / ligament diameter.

Chapter 6

Defects correlated mechanical behavior of nanoporous Au using positron annihilation spectroscopy

6.1. Introduction

The microstructure of nanoporous Au (np- Au) is in the form of a skeletal structure consisting of inter-connected nanometer scaled Au ligaments, and three-dimensional continuous pores. This bi-continuous structure has been evolved by a self - diffusion process during the selective dissolution of Ag from a binary Ag-Au alloy phase. It is well known that microstructure in nanoporous Au has a significant effect on the mechanical behavior such as hardness and yield strength, similar to that obtained in ultra-fine grained materials. Several studies have been reported [36,38,40,145] on the deformation mechanism and ligament strength of np- Au based on ligament size and relative density of the Au metal foam. Investigations via experiments revealed that there is a systematic increase in hardness and yield strength with the reduction of ligament diameter and these values approached the theoretical value for a ligament diameter of 5 nm [3]. Li et al. have investigated the mechanical behavior of np- Au with various ligament size using a three-point bending method and reported ligament size driven ductile-brittle transition at smaller dimensions [34]. Mechanical testing of np- Au performed by the most often used nanoindentation technique indicated that although np-Au appears fragile and weak macroscopically, the technique measures the hardness value accurately from the skeletal ensemble of ligaments and pores [40]. The scaling law formulated by Gibson and Ashby [37] have been used extensively to compare the mechanical properties of np- Au obtained by different techniques [39,146].

The mechanical behavior of np- Au obtained from various techniques viz., nanoindenter and axial compression provide the unique information that as the ligament diameter decreases, the hardness and yield strength in np- Au increased. Based on such a data compilation on ligament size dependent yield strength and hardness behaviors in np-Au, it has generally been suggested that ligament diameter is the most important parameter controlling the mechanical behavior of np- Au [145]. In contrast, the present results highlight the fact that as the deformation activity in np- Au is constraining more and more along the ligament with the reduction of ligament diameter, the increased vacancy concentration along the ligament network structure influences significantly for attaining higher ligament network strength. Such a directional motion of vacancy defects is currently of particular interest in recent research. Viswanath et al. have investigated the Hall-Petch exponent of np- Au from the Vickers hardness data and obtained an exponent of *-0.3* with ligament diameter, instead of the scaling exponent α value *-0.5* reported in materials of reduced dimensions such as nanomaterials, thin films and multilayers [8]. This suggests that apart from the ligament diameter in controlling the plasticity in np- Au, the concentration of defects in the ligament networks is also a key parameter in governing its mechanical behavior in np- Au.

Stacking fault tetrahedra (SFT) is the most common type of vacancy clustering defect formed in face-centered-cubic (FCC) metals like Au, Ag, and Cu [107,147,148]. The results obtained from the computational work claimed that SFT is the stable and energetically more favorable defect formed in the metallic ligaments and influences the mechanical behavior of the metal foams [149]. Caro et al. reported that the radiation-induced SFTs act as an obstacle to dislocation motion in np- Au and giving rise to a higher hardness value [150]. Another mechanism reported for the materials strengthening is substitutional solid solution strengthening observed in Au-Fe alloy [151,152]. The effect of solute Fe atoms in the Au-Fe alloy offers greater resistance to dislocation motion. This suggests that the mechanical properties could be easily influenced by Fe^+ ion irradiation [153,154]. In order to understand further about the issue of correlation between the mechanical behavior and strain field of vacancy defects, the np- Au samples were irradiated with Fe^+ ions using the accelerator facility available in our research group and studied the variation of nanoindentation hardness in np- Au and compared with measurements in un- irradiated np- Au and bulk Au. It is seen that the measured nanoindentation hardness scales with the vacancy concentration within the ligaments, as $C_v^{0.5}$, pointing to the interaction of lattice dislocations with vacancy clusters in the skeletal np- Au.

6.2. Experimental procedure

The fabrication of disc-shaped np- Au samples of dimension (15 mm x15 mm x 2 mm) with a pore density of 70% (np- Au density 5.79 g/cc) were achieved by electrochemical dealloying of $Ag_{75}Au_{25}$ alloy as described previously [20]. Similarly, a thin Au foil (purity 99.99%) of thickness few tens of µm and 2 cm diameter was prepared and annealed at 800 ^{o}C in 10^{-6} mbar vacuum. The Au foil and np- Au samples were irradiated with 900 keV Fe^+ ions to 10 dpa (displacement per atom) at room temperature with a fluence of 2×10^{15} ions/cm^2 in a 1.7 MV tandetron accelerator. The corresponding damage profiles were calculated using SRIM 2008 [79] which simulates the damage profile produced by irradiated energetic ions. Depth profile mechanical, and defect studies using nanoindenter and low energy positron beam techniques were carried out for all the samples at room temperature, respectively. Nanoindentation testing was performed using a compact platform Ultra Nanoindentation Tester (M/s Anton Paar, Switzerland) equipped with a three-sided pyramidal diamond (Berkovich) tip with an end radius of 30 nm. The nanoindentation hardness tester provides the hardness values as a function of indenter depth. The details of low energy positron beam experiments and measurement methodology were discussed in chapter 2.4 [21].

Depth-resolved low energy positron beam experiments were performed on irradiated np- Au samples as a function of annealing temperature. The low energy positron beam is derived using a 50 mCi Na^{22} source coupled with W(100) moderator [60]. The low energy positron beam energy was varied in the range of 0.2 to 22 keV with steps of 0.5 keV. The positron annihilation Doppler broadening spectrum was collected with each E_P value using a high purity Germanium (HPGe) detector having resolution of 1.4 keV at 662 keV of Cs^{137}. Depth-wise defect/ defect free sites in np- Au samples can be identified from the analysis of positron annihilation Doppler broadening line shape parameters as a function of positron beam energy.

6.3. Result and discussions

Left panels in Figures 6.1 a) and b) show the typical Fe and vacancy distribution profiles for 900 keV Fe implanted bulk Au and np- Au obtained from the simulation using SRIM 2008 software, respectively. The right panel in the Figures 6.1 a) and b) show the schematic illustration of the plastic region formed in-depth underneath to the Berkovich indenter. In bulk Au sample, the Fe ion distribution and vacancy profile distribution peaks occur at 215 nm and 140 nm, respectively. In the case of np- Au sample, the Fe ion distribution, and vacancy distribution peaks occur at 740 nm and 510 nm, respectively.

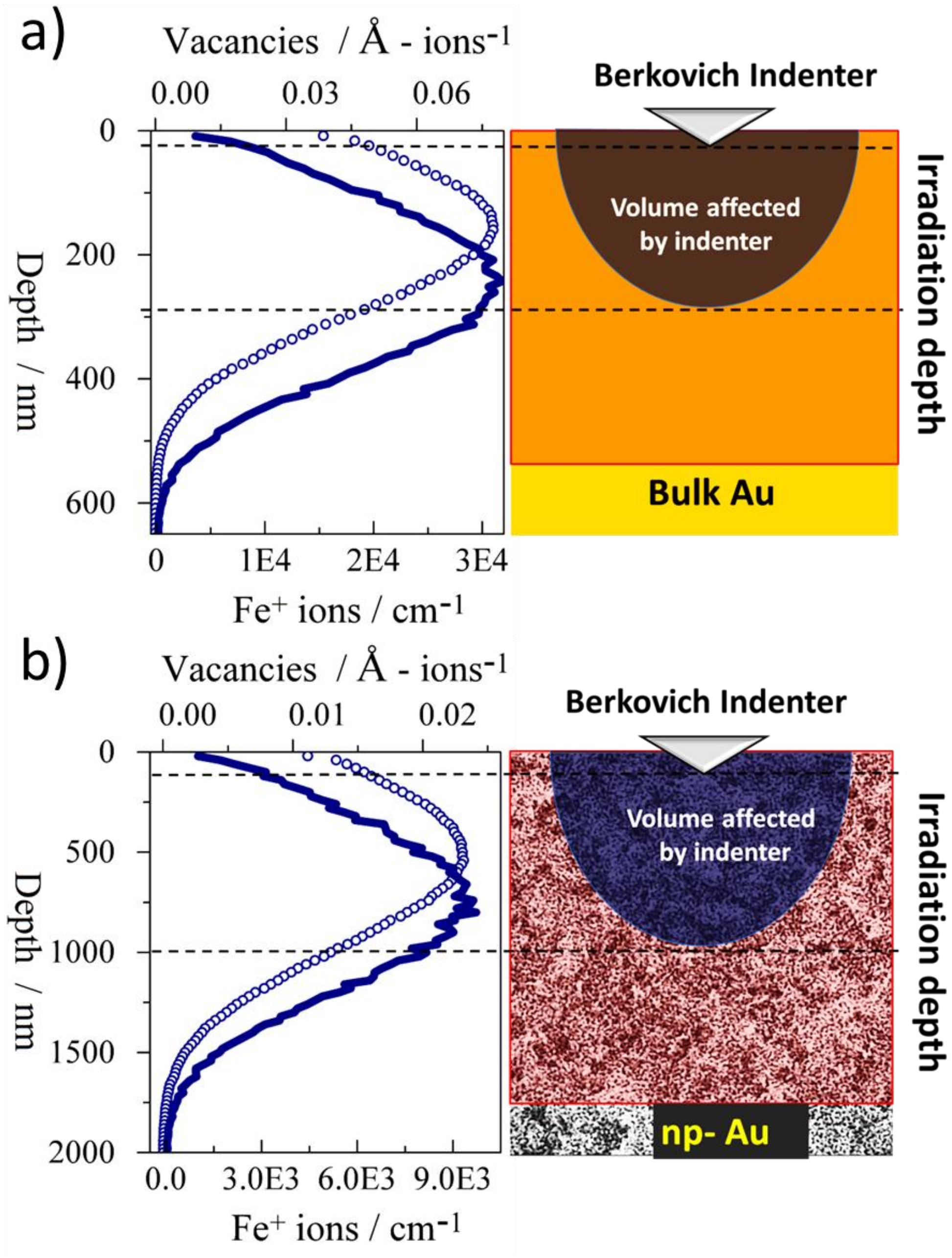

Fig. 6.1 Fe and vacancy distribution behaviors in 900 keV Fe^+ ion irradiated a) bulk Au and b) np- Au. The right panel in the figure illustrates the schematics of plastic region formed underneath to the Berkovich indenter.

Figure 6.2 shows a typical nanoindentation load-displacement (*P*-*h*) curve obtained from the 900 keV Fe^+ ion irradiated np- Au sample using Berkovich tip. The hardness values are obtained using Oliver-Pharr method as discussed in chapter 2.7 (cf. Figure 2.19 b)).

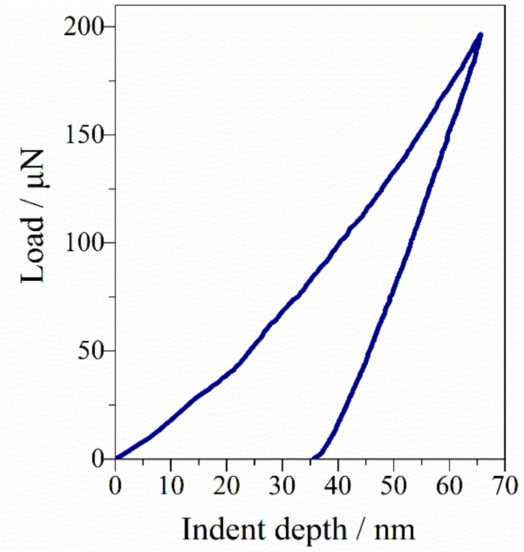

Fig. 6.2 A typical load versus displacement curve (P-h) of 900 keV Fe$^+$ ion irradiated np- Au sample using Berkovich tip

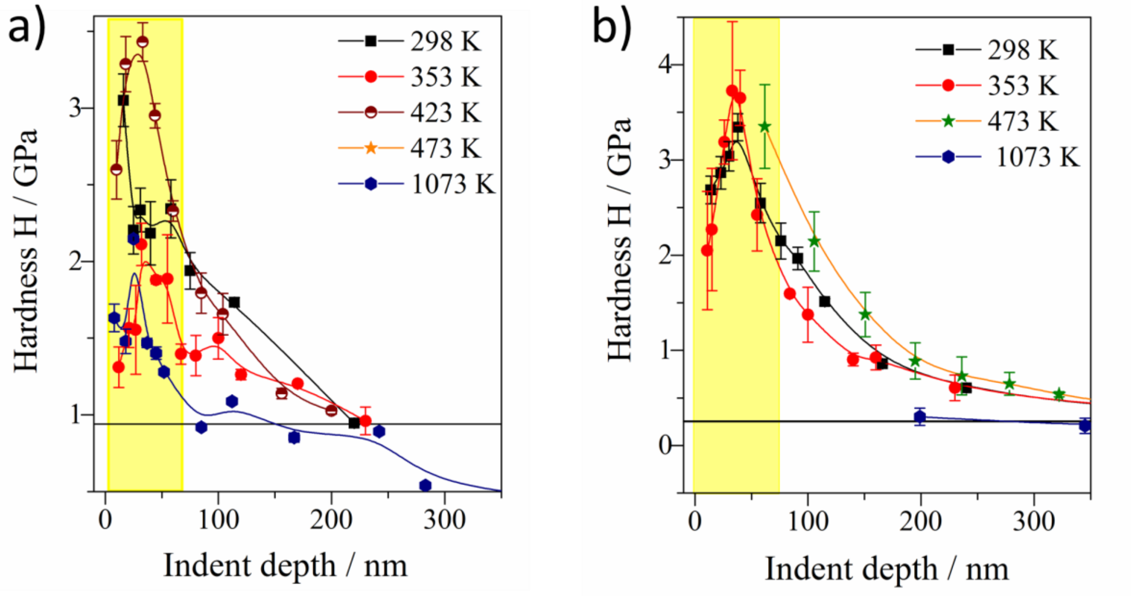

Fig. 6.3 Plots of depth-dependent hardness of Fe$^+$ ion irradiated samples. (a) Irradiated bulk Au (b) irradiated np- Au at various annealing temperatures. Horizontal solid line in both graphs indicates the mean hardness value of un-irradiated samples.

Figure 6.3 summarizes the experimentally measured nanoindentation hardness results for 900 keV Fe$^+$ ion irradiated bulk and nanoporous Au samples. Figure 6.3 a) shows the hardness behavior of Fe$^+$ ion irradiated bulk Au and Figure 6.3 b) shows the hardness behavior of Fe$^+$ ion irradiated np- Au with annealing temperature of range 298 - 1073 K. The horizontal solid line at 0.94 GPa in Figure 6.3 a) and 253 MPa in Figure

6.3 b) corresponds to the measured mean hardness value for bulk Au and as- dealloyed np- Au, respectively. It is seen that there is a significant enhancement in hardness value in Fe^+ ion irradiated bulk and nanoporous Au in comparison to their un-irradiated counterparts. It is worth noting that the indent depth at which the hardness reached a maximum is in the region where the concentration of Fe^+ ions is higher. This strong hardening effect obtained in the Fe^+ ions irradiated Au samples might be related to the population of excess number of vacancies around the localized Fe sites and the associated Fe solute – vacancy interactions.

To understand the reason behind the significant enhancement in hardness at the Fe rich layer, depth-resolved low energy positron beam Doppler broadening spectroscopy experiments were carried out. We have already reported that positron diffusion length L_{eff} scales with ligament diameter d with a power law dependence $L_{eff} \propto d^{1/3}$. It indicates that the thermalized positrons in np- Au are diffusing along the Au ligaments [21]. Since, the positron beam studies help to understand the Fe implanted region, the dependencies of the S - parameter on the positron incident energy E_P for Fe^+ ion irradiated and un-irradiated np- Au and bulk Au were analyzed. The mean implantation depth $\bar{z}$ of the positron for the given energy E_P is calculated [69,70] (the top X-axis) from the equation, $\bar{z} = A{E_P}^n/\rho$ where A = 3.67 mg.cm^{-2}keV^{-n}, n = 1.6 is the empirical constant, and ρ is density of the given sample (5.79 g/cc for 30% dense np- Au and 19.3 g/cc for dense Au).

Figures 6.4 a) and b) shows the dependence of the S - parameter with positron beam energy for the pre and post-irradiated np- Au and bulk Au samples at different annealing temperature, respectively. It is seen from both Figures 6.4 a) and b) that the variation of S-parameter, which is sensitive to lattice defects, with E_P, is different for Fe^+ irradiated samples in comparison to their un-irradiated counterparts. This indicates that Fe implantation enhances the generation of vacancy clusters extending from sample surface to deeper region. This is close to 600 nm for np- Au and 300 nm for bulk Au. Importantly, a plateau-like region develops in the S-parameter versus E_P curves around the beam energy E_P value 15 keV for both irradiated bulk Au and np- Au and these abnormal deviation occurs in the sample depth where the Fe^+ ion induced vacancy concentration is higher. This indicates that the defects that are generated in the ligaments during the evolution of porosity interact with Fe atoms and forms Fe-vacancy complex clusters.

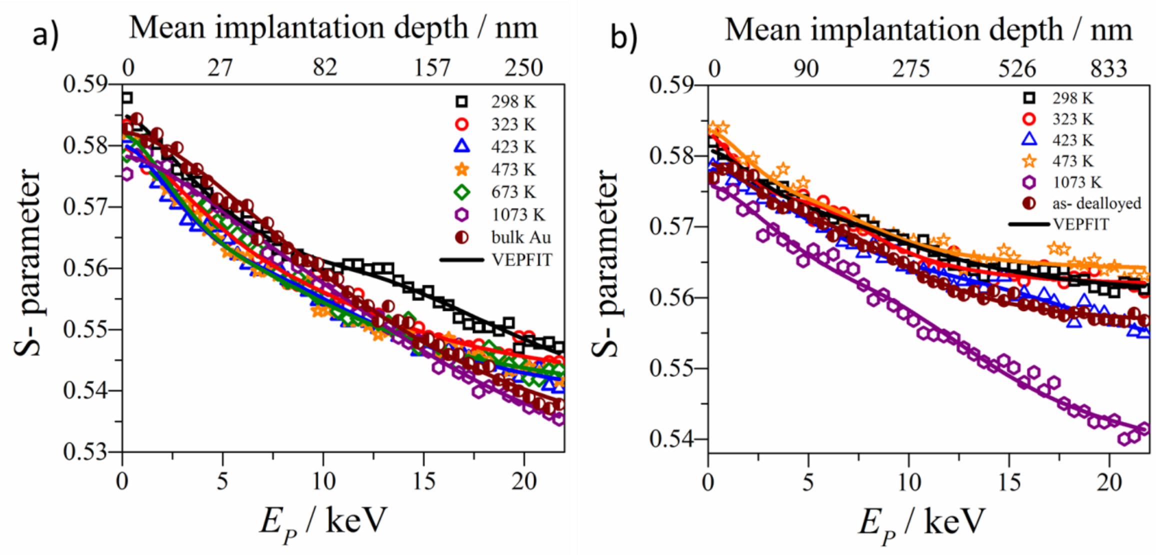

Fig. 6.4 S - parameter versus positron incident beam energy E_P for Fe^+ ion irradiated and un-irradiated a) bulk Au and b) np- Au samples at various temperatures. Solid lines passes through the data points in both sub figures represent the best fit to the data using the VEPFIT code.

The average concentration of defects C_v can be deduced from the fitted S(E_P) curves if specific trapping rate and bulk life time of the Au are known for the following equation [24],

$$C_v = \frac{1}{\mu_v \tau_b}\left[\frac{S - S_b}{S_d - S}\right] \tag{6.1}$$

where S_b and S_d are S - parameter corresponding to the bulk and defect, respectively. Here, are assume a specific trapping rate $\mu_v = 1.35 \times 10^{14}\ s^{-1}$ for vacancies in Au and positron bulk lifetime τ_b for Au (122 ps) [3].

In Figure 6.5 a), we show the annealing temperature dependent average defect concentration C_v of as- dealloyed np- Au, irradiated np- Au and irradiated bulk Au. It is seen that the concentration of defects in as- dealloyed and irradiated np- Au samples increases significantly up to 473 K and after which the C_v value decreases monotonically and falls back to the value close to that of bulk Au. It must be mentioned that the C_v versus annealing temperature behavior shown in sub figure 6.5 a) is similar to that obtained from the S(E_P) plots on un-irradiated np- Au (cf. Figure 5.3 b) in Chapter 5. With the support of literature reports and based on our previous microstructure studies on np- Au [130], we infer that the initial increase in the C_v value with annealing temperature shown in Figure 6.5 a) may be attributed to formation of additional Fe-vacancy clusters. The decreasing trend in the C_v versus annealing temperature obtained above 473 K might be indicative of dissociation of Fe-vacancy and vacancy annealing associated with the rapid growth of ligament diameter with increasing annealing temperature [21].

In order to understand the implications of the variation in the hardness and the evolution of vacancies in irradiated np- Au with annealing, we have plotted the peak hardness of irradiated np- Au samples with annealing temperature and compared with measurements in irradiated bulk Au and un-irradiated np- Au (Figure 6.5 b)). Among all the peak hardness results depicted in Figure 6.5 b), the Fe ion irradiated np- Au shows the highest hardness value. We have taken the peak hardness value for the present discussion because of the fact that the depth at which the hardness value reached maximum corresponds to the region where the concentration of Fe-vacancy clusters is higher.

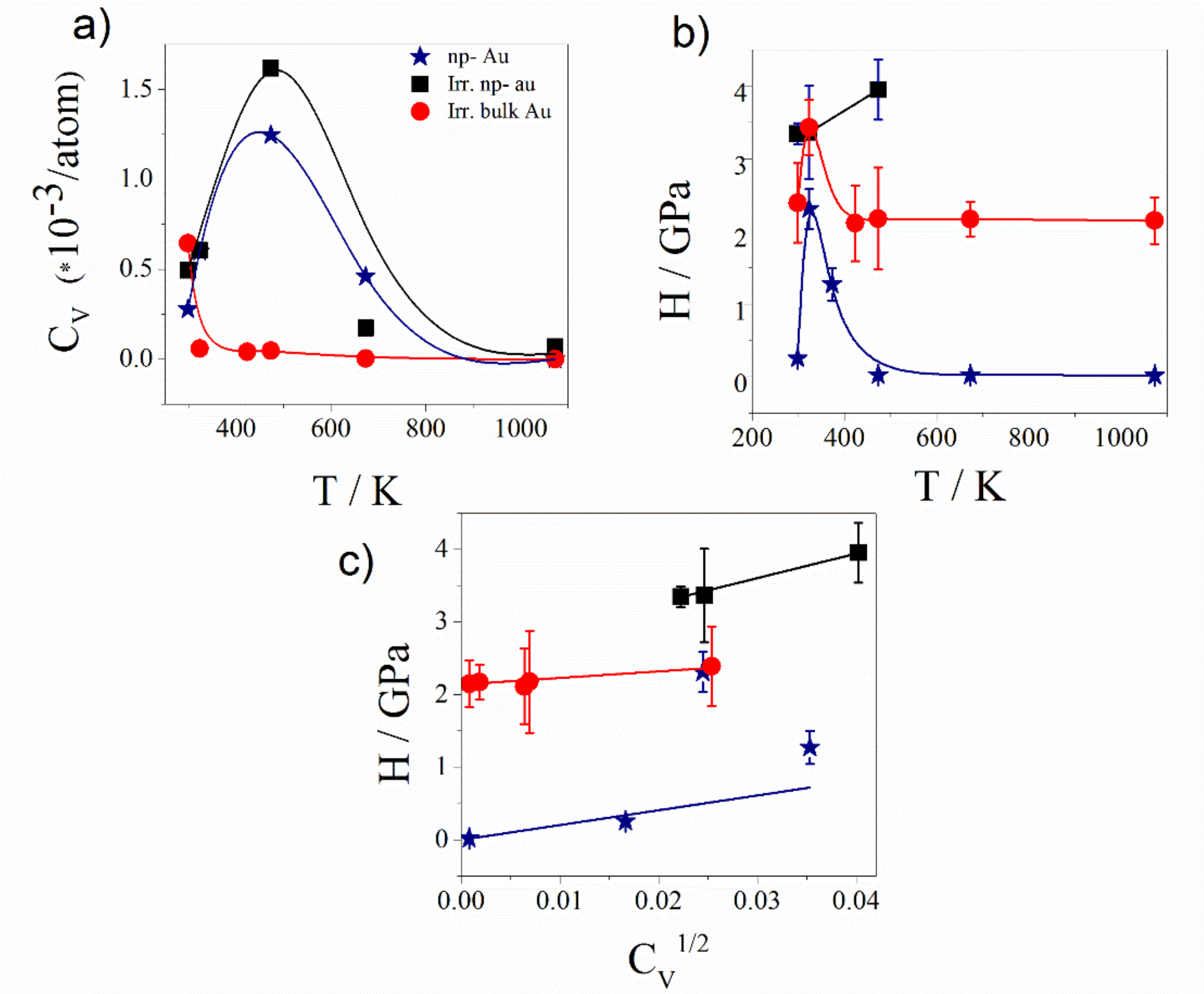

Fig. 6.5 a) Concentration of vacancies C_v in as- dealloyed np- Au, Fe$^+$ ion irradiated np- Au and Fe$^+$ ion irradiated bulk Au computed from positron beam Doppler broadening S - parameter with annealing temperature. b) Peak hardness obtained from figure 6.3 with annealing temperature for as dealloyed and irradiated np- Au and irradiated bulk Au. c) Relationship between the nanoindentation hardness and the square root of vacancy concentration in irradiated np- Au and irradiated bulk Au.

Irradiation induced hardening in metal has been extensively studied for decades using experiments and simulations [155–158] but several issues still requires better understanding. Positron annihilation spectroscopy coupled nanoindentation could offer the possibility to understand the nature of defect structure that is responsible for the higher hardness value in Fe$^+$ ion irradiated np- Au. If the irradiation induced vacancy clusters in np- Au is responsible for the strengthening, then it is of interest to examine the correlation between the hardness and the vacancy concentrations. The correlation between the experimentally obtained depth-wise defect structure and the indent-depth dependent hardness values allow to understand the atomic level changes that are responsible for the higher hardness value obtained in irradiated np- Au. It is shown that the hardness value depicted in Figure 6.5 c) is related to the defect concentration in the ligaments and scales as $C_v^{0.5}$. Chang et al. also reported similar observation that the obstacle to the pinning dislocation caused by dislocation-point defect interaction leads to a square root dependence of the yield strength on the defect concentration according to the relation, $H_V = 6\gamma\mu C_v^{0.5}$, where μ is the shear modulus (27 GPa for bulk Au [159]), γ is a coefficient and is less than unity, which depends on the strength of the interaction and C_v is the defect density [160,161]. The slope of linear correlation between hardness and $C_v^{1/2}$ gives the hardening rate or hardening coefficient of the material. It can be seen that the irradiated np- Au is more effective hardener than irradiated bulk Au. Moreover, the defect density and dominant defect are different at elevated temperature. The vacancy defect and its cluster impede the dislocation motion results the higher hardness upto 400 K and these defects are no longer stable at higher temperature which means the generated point defects annihilated through the absorption by dislocations makes the hardness decreases. The present and our earlier positron annihilation studies have summarized the implanted Fe atoms interacts with negatively charged vacancies and forming complex Fe-vacancy clusters. Based on the above facts, one can be believed that the higher hardness value obtained in both irradiated np- Au and bulk Au might be due to the formation of large density of Fe solute-vacancy clusters and the resulting hindrance to the impeding dislocation motion underneath to the indentation.

6.4. Conclusion

The low energy positron beam Doppler broadening spectroscopy combined with Nanoindentation hardness measurements offer a clear picture of defect dislocation interaction in irradiated layer. Nanoindentation measurements have successfully shown the effect of ion-irradiation on the mechanical properties of np- Au and bulk Au. Defect concentration and its complex interactions with dislocation around the Fe implanted region, confirmed by significant increase of S - parameter, contributes significantly for the enhancement of hardness values in irradiated np- Au and bulk Au samples. The correlation between the experimentally obtained depth-wise defect structure and the indent-depth dependent hardness values allow to understand the atomic level changes that are responsible for the higher hardness value obtained in irradiated np- Au. More studies towards this direction are highly essential for further understanding the atomic level changes that occur during the formation of complex Fe-vacancy cluster structures around the Fe implanted region in nanoporous Au.

Chapter 7

Summary and Future scope

The present thesis discussed about the development of nanoporous metallic materials, investigation of microstructure coupled defect evolution during fabrication, and defect correlated mechanical behavior of nanoporous metallic materials. The thesis started with the investigation on a model nanoporous metallic material, nanoporous Au using positron annihilation spectroscopy which provides the new insights about ligament-pore interface properties. Understanding of defects and their evolution has yielded a better understanding of the underlying mechanism in the evolution of nanoporous Au and structure coarsening with effect of atomic defects presents in ligament-pore network. A brief, chapter-wise summary of the thesis along with the scope for future study, is outlined.

7.1. Key findings of the thesis

The results from the development of nanoporous Au and microstructural evolution with chemical information of np- Au towards electro-oxidation/reduction as discussed in chapter 3, are summarized as follows.

- Successfully produced nanoporous Au through electrochemical dealloying method with ligament diameter of 5 nm.
- Pseudo-capacitive double layer structure develops explicitly at the as- dealloyed nanoporous Au/$HClO_4$ interface where the reduced nanoporous Au/$HClO_4$ interface is capacitive in nature.
- Initial stage of electro-oxidation corresponding to the monolayer adsorption of oxygen containing species occurs on the ligament surfaces in reduced np – Au.

The formation of oxides in as- dealloyed np - Au occurs by a sequential conversion of Au - OH dipoles to AuO and subsequently by a conversion and growth of Au_2O_3 on top of AuO by a chemical reaction $2AuO + H_2O \rightarrow Au_2O_3 + 2H^+ + 2e^-$.

- The inter-planar spacing for Au (111) and Au (200) in as- dealloyed nanoporous Au has increased by 8% in comparison to those obtained in reduced nanoporous Au and in bulk Au. The occurrence of such unusual lattice swelling effect evolved in as- dealloyed np- Au, in contrast to reduced np- Au and bulk Au is attributed to the binding of oxygen ads-species, albeit weakly, in the presence of lattice defects.

The results from the measurement of specific surface area of nanoporous Au, as discussed in chapter 4, can be summarized as follows:

- Electrochemical double layer capacitance ratio method accurately determines the temperature dependent variation of specific capacitance C_S and specific-mass surface area α_m in nanoporous Au for two distinct surface states viz., as- dealloyed and reduced clean metallic.
- As- dealloyed np-Au does not change its C_S and α_m values, suggesting that the adsorbed oxygen containing species weakly bonded with Au during the evolution of nanoporous architecture and prevents ligament coarsening upon heating. This observation is in contrast to the pronounced ligament coarsening with temperature that exists on reduced clean metallic np-Au.
- Determined the specific surface area of np- Au through electrochemical (double layer charging / OH adsorption-desorption) and analytical (BET) methods and compared with the geometrical ball-stick model successfully. The master plot α_m vs. d, successfully brought out the complementary nature of various methods used in this study.

The results obtained through positron diffusion behavior in nanoporous Au, as discussed in chapter 5, can be summarized as follows:

- The role of defects in the process of ligament coarsening with temperature have been studied using low energy positron Doppler beam broadening spectroscopy measurements.
- The low energy positron beam experiments have also been analyzed to extract the positron diffusion length.
- The positron diffusion length increases with the ligament diameter and scales according to $d^{1/3}$, which points to the dominance of defects localization along the length of the ligaments.

The results of defect correlated mechanical behavior of nanoporous Au and bulk Au, as discussed in chapter 6, are summarized as follows:

- The low energy positron beam Doppler broadening spectroscopy combined with nanoindentation hardness measurements offered a clear picture of defect dislocation interaction in irradiated layer.
- The influence of ion-irradiation on the mechanical properties of np- Au and bulk Au was studied by nanoindentation method. Higher hardness value was obtained on Fe^+ ion Irradiated np- Au.
- The observation of hardness of np- Au increasing linearly with $C_v^{0.5}$ probably caused by the presence of SFTs in the ligaments and ligament interconnects which impede the motion of dislocation.
- Vacancy cluster (void, SFT) - solute complexes enhance the stress field required for plastic deformation in irradiated np- Au samples.

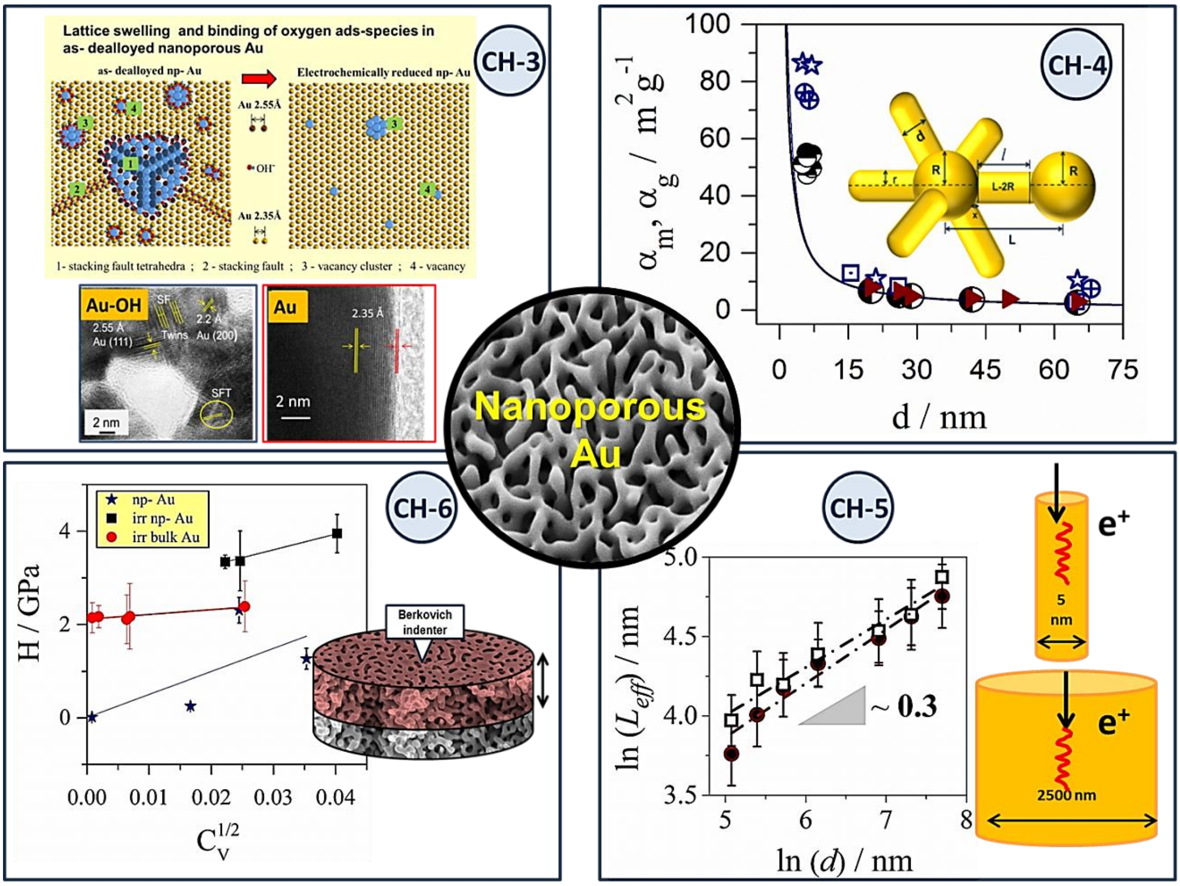

Fig. 7.1 Schematic view of key finding of the present thesis.

The key findings of this thesis are schematically shown in Fig. 7.1. Mechanically stable skeleton nanoporous Au samples were prepared by electrochemical dealloying method. High density of atomic defects populates in the ligaments during the evolution of metallic Au skeleton structure. Microstructural characterizations were carried out on np-Au with different surface states to understand the influence of subtle variation of surface states on microstructural evolution. Surface area of np- Au was determined using both experimental and geometrical methods. To identify the nature of defects that are responsible for the ligament coarsening in np- Au, positron annihilation spectroscopy measurements were carried out. The role of defects in the variation of mechanical behavior in np- Au with annealing temperature and with ion irradiation has been studied. The linear correlation obtained between hardness and square root of vacancy concentration predicts that vacancy-type defects have larger effects on mechanical behavior in np- Au. The aforementioned results are the key findings of this thesis research work.

7.2. Future scope

- Designing of reduced nanoporous Au as positron moderator material.
- Study of positron diffusion and positronium fraction in reduced np- Au samples.
- Study of positron lifetime behavior of reduced nanoporous Au with respect to annealing temperature.
- Developing other nanoporous metals like Pt, Pd and W for potential applications.
- Electrochemically coating metal oxides on nanoporous Au to enhance their functional properties.

References

[1] J. Biener, A. Wittstock, L. A. Zepeda-Ruiz, M. M. Biener, V. Zielasek, D. Kramer, R. N. Viswanath, J. Weissmüller, M. Bäumer, and A. V. Hamza, Nat. Mater. **8**, 47 (2009).

[2] J. Erlebacher, M. J. Aziz, A. Karma, N. Dimitrov, and K. Sieradzki, Nature **410**, 450 (2001).

[3] R. N. Viswanath, V. A. Chirayath, R. Rajaraman, G. Amarendra, and C. S. Sundar, Appl. Phys. Lett. **102**, 253101 (2013).

[4] B. E. Conway, Prog. Surf. Sci. **49**, 331 (1995).

[5] H. Rösner, S. Parida, D. Kramer, C. A. Volkert, and J. Weissmüller, Adv. Eng. Mater. **9**, 535 (2007).

[6] E. Detsi, E. De Jong, A. Zinchenko, Z. Vuković, I. Vuković, S. Punzhin, K. Loos, G. ten Brinke, H. A. De Raedt, P. R. Onck, and J. T. M. De Hosson, Acta Mater. **59**, 7488 (2011).

[7] P. J. Schultz and K. G. Lynn, Rev. Mod. Phys. **60**, 701 (1988).

[8] R. N. Viswanath, S. R. Polaki, R. Rajaraman, S. Abhaya, V. A. Chirayath, G. Amarendra, and C. S. Sundar, Appl. Phys. Lett. **104**, 233108 (2014).

[9] Y. Ding and Z. Zhang, *Nanoporous Metals for Advanced Energy Technologies* (Springer US, 2016).

[10] D. H. Everett, Pure Appl. Chem. **31 (4)**, 577 (1972).

[11] A. Wittstock, B. Neumann, A. Schaefer, K. Dumbuya, C. Kübel, M. M. Biener, V. Zielasek, H.-P. Steinrück, J. M. Gottfried, J. Biener, A. Hamza, and M. Bäumer, J. Phys. Chem. C **113**, 5593 (2009).

[12] A. Wittstock, J. Biener, and M. Baumer, Phys. Chem. Chem. Phys. **12**, 12919 (2010).

[13] J. Weissmüller, R. N. Viswanath, D. Kramer, P. Zimmer, R. Würschum, and H. Gleiter, Science (80-.). **300**, 312 LP (2003).

[14] D. Kramer, R. N. Viswanath, and J. Weissmüller, Nano Lett. **4**, 793 (2004).

[15] A. J. Forty, Gold Bull. **14**, 25 (1981).

[16] R. C. Newman and K. Sieradzki, Science (80-.). **263**, 1708 LP (1994).

[17] S. Parida, D. Kramer, C. A. Volkert, H. Rösner, J. Erlebacher, and J. Weissmüller, Phys. Rev. Lett. **97**, 35504 (2006).

[18] H. W. Pickering and C. Wagner, J. Electrochem. Soc. **114**, 698 (1967).

[19] J. Erlebacher, J. Electrochem. Soc. **151**, C614 (2004).

[20] C. Lakshmanan, R. N. Viswanath, S. R. Polaki, R. Rajaraman, S. Dash, and A. K. Tyagi, Electrochim. Acta **182**, 565 (2015).

[21] C. Lakshmanan, R. N. Viswanath, R. Rajaraman, S. Dash, G. Amarendra, and C. S. Sundar, Europhys. Lett. **117**, 48007 (2017).

[22] J. Y. Park, H. C. W. Huang, R. W. Siegel, and R. W. Balluffi, Philos. Mag. A **48**, 397 (1983).

[23] J. Gubicza, *X-Ray Line Profile Analysis in Materials Science* (IGI Global, 2014).

[24] R. Krause-Rehberg and H. S. Leipner, *Positron Annihilation in Semiconductors: Defect Studies* (Springer, 1999).

[25] H. E. Schaefer and R. Würschum, Phys. Lett. A **119**, 370 (1987).

[26] H.-E. Schaefer, R. Würschum, R. Birringer, and H. Gleiter, Phys. Rev. B **38**, 9545 (1988).

[27] S. Van Petegem, S. Brandstetter, R. Maass, A. M. Hodge, B. S. El-Dasher, J. Biener, B. Schmitt, C. Borca, and H. Van Swygenhoven, Nano Lett. **9**, 1158 (2009).

[28] P. Liu, P. Guan, A. Hirata, L. Zhang, L. Chen, Y. Wen, Y. Ding, T. Fujita, J. Erlebacher, and M. Chen, Adv. Mater. **28**, 1753 (2016).

[29] B. Zugic, L. Wang, C. Heine, D. N. Zakharov, B. A. J. Lechner, E. A. Stach, J. Biener, M. Salmeron, R. J. Madix, and C. M. Friend, Nat. Mater. **16**, 558 (2016).

[30] R. Zeis, T. Lei, K. Sieradzki, J. Snyder, and J. Erlebacher, J. Catal. **253**, 132 (2008).

[31] X. Lang, A. Hirata, T. Fujita, and M. Chen, Nat. Nanotechnol. **6**, 232 (2011).

[32] B. E. Conway, *Electrochemical Supercapacitors Scientific Fundamentals and Technological Applications* (Springer US, 1999).

[33] B. Hammer and J. K. Norskov, Nature **376**, 238 (1995).

[34] R. Li and K. Sieradzki, Phys. Rev. Lett. **68**, 1168 (1992).
[35] S. Ye, Y. Jia, M. A. M., and B. T. John, Microsc. Res. Tech. **72**, 232 (2009).
[36] A. M. Hodge, J. Biener, J. R. Hayes, P. M. Bythrow, C. A. Volkert, and A. V Hamza, Acta Mater. **55**, 1343 (2007).
[37] L. J. Gibson and M. F. Ashby, *Cellular Solids: Structure and Properties* (Oxford, 1988).
[38] J. Biener, A. M. Hodge, A. V Hamza, L. M. Hsiung, and J. H. Satcher, J. Appl. Phys. **97**, 24301 (2004).
[39] J. Biener, A. M. Hodge, J. R. Hayes, C. A. Volkert, L. A. Zepeda-Ruiz, A. V Hamza, and F. F. Abraham, Nano Lett. **6**, 2379 (2006).
[40] C. A. Volkert, E. T. Lilleodden, D. Kramer, and J. Weissmüller, Appl. Phys. Lett. **89**, 61920 (2006).
[41] M. Hakamada and M. Mabuchi, Scr. Mater. **56**, 1003 (2007).
[42] K. Gall, J. Diao, and M. L. Dunn, Nano Lett. **4**, 2431 (2004).
[43] B. Wu, A. Heidelberg, and J. J. Boland, Nat. Mater. **4**, 525 (2005).
[44] J. R. Greer and W. D. Nix, Appl. Phys. A **80**, 1625 (2005).
[45] J. Li, C. Fan, Q. Li, H. Wang, and X. Zhang, Acta Mater. **143**, 30 (2018).
[46] E. G. Fu, M. Caro, L. A. Zepeda-Ruiz, Y. Q. Wang, K. Baldwin, E. Bringa, M. Nastasi, and A. Caro, Appl. Phys. Lett. **101**, 191607 (2012).
[47] I. J. Beyerlein, A. Caro, M. J. Demkowicz, N. A. Mara, A. Misra, and B. P. Uberuaga, Mater. Today **16**, 443 (2013).
[48] E. M. Bringa, J. D. Monk, A. Caro, A. Misra, L. Zepeda-Ruiz, M. Duchaineau, F. Abraham, M. Nastasi, S. T. Picraux, Y. Q. Wang, and D. Farkas, Nano Lett. **12**, 3351 (2012).
[49] Y. Chimi, A. Iwase, N. Ishikawa, M. Kobiyama, T. Inami, T. Kambara, and S. Okuda, Nucl. Instruments Methods Phys. Res. Sect. B Beam Interact. with Mater. Atoms **245**, 171 (2006).
[50] H. Okamoto and T. B. Massalski, *Phase Diagrams of Binary Gold Alloys* (ASM International Metals Park, 1987).
[51] N. A. Senior and R. C. Newman, Nanotechnology **17**, 2311 (2006).
[52] K. Sieradzki, N. Dimitrov, D. Movrin, C. McCall, N. Vasiljevic, and J. Erlebacher, J. Electrochem. Soc. **149**, B370 (2002).
[53] H. W. Pickering, Corros. Sci. **23**, 1107 (1983).
[54] J. Erlebacher and K. Sieradzki, Scr. Mater. **49**, 991 (2003).
[55] A. Dursun, Nanoporosity Formation in Ag-Au Alloys, The Virginia Polytechnic Institute and State University, 2003.
[56] H. W. Pickering and C. Wagner, J. Electrochem. Soc. **114**, 698 (1967).
[57] K. Sieradzki, R. R. Corderman, K. Shukla, and R. C. Newman, Philos. Mag. A **59**, 713 (1989).
[58] A. J. Bard and L. R. Faulkner, *Electrochemical Methods: Fundamentals and Applications* (John Wiley & Sons, 2001).
[59] C. G. Zoski, *Handbook of Electrochemistry* (Elsevier, 2007).
[60] G. Amarendra, B. Viswanathan, G. V. Rao, J. Parimala, and B. Purniah, Curr. Sci. **73**, 409 (1997).
[61] P. A. M. Dirac, Proc. R. Soc. London. Ser. A **117**, 610 LP (1928).
[62] P. A. M. Dirac, Proc. R. Soc. London. Ser. A **126**, 360 LP (1930).
[63] C. D. Anderson, Phys. Rev. **43**, 491 (1933).
[64] P. Hautojarvi and A. Vehanen, *Positron in Solids* (Springer-Verlag, Berlin, 1979).
[65] C. M. Lederer and V. S. Shirley, *Table of Isotopes* (John Wiley & Sons, 1978).
[66] C. Hugenschmidt, Surf. Sci. Rep. **71**, 547 (2016).
[67] A. Makhov, Sov. Phys. Solid State **2**, 1934 (n.d.).
[68] A. Vehanen, K. Saarinen, P. Hautojärvi, and H. Huomo, Phys. Rev. B **35**, 4606 (1987).
[69] V. J. Ghosh, Appl. Surf. Sci. **85**, 187 (1995).
[70] M. J. Puska and R. M. Nieminen, Rev. Mod. Phys. **66**, 841 (1994).
[71] G. F. Knoll, *Radiation Detection and Measurement, 4th Edition*, 4th ed. (John Wiley & Sons, 2010).

[72] J. Kansy, Nucl. Instruments Methods Phys. Res. Sect. A Accel. Spectrometers, Detect. Assoc. Equip. **374**, 235 (1996).

[73] D. G. Costello, D. E. Groce, D. F. Herring, and J. W. McGowan, Phys. Rev. B **5**, 1433 (1972).

[74] D. A. Fischer, K. G. Lynn, and D. W. Gidley, Phys. Rev. B **33**, 4479 (1986).

[75] P. Coleman, 340 (2000).

[76] K. F. Canter and A. P. Mills Jr., Can. J. Phys. **60(4)**, 551 (1982).

[77] A. van Veen, H. Schut, J. de Vries, R. A. Hakvoort, and M. R. Ijpma, AIP Conf. Proc. **218**, 171 (1991).

[78] L. C. Feldman, .J. W. Mayer, and S. T. Picraux, *Materials Analysis by Ion Channeling: Submicron Crystallography* (Academic Press, New York, 1982).

[79] Z. F. Ziegler, J. P. Biersack, and U. Littmark, *Stopping and Range of Ions in Solids* (Pergamon Press, New York, 1985).

[80] M. Nastasi and J. W. Mayer, *Ion Implantation and Synthesis of Materials* (Springer - Verlag, Berlin, 2006).

[81] J. Goldstein, D. E. Newbury, D. C. Joy, C. E. Lyman, P. Echlin, E. Lifshin, L. Sawyer, and J. R. Michael, *Scanning Electron Microscopy and X-Ray Microanalysis* (Springer, 2003).

[82] Z. Luo, *A Practical Guide to Transmission Electron Microscopy* (Momentum Press Engineering, 2016).

[83] R. F. Egerton, *Electron Energy-Loss Spectroscopy in the Electron Microscope* (Springer Science+Bussiness Media, 2011).

[84] F. Yang and J. C. M. Li, *Micro and Nano Mechanical Testing of Materials and Devices* (Springer US, 2008).

[85] A. C. Fischer-Cripps, *Nanoindentation*, 3rd ed. (Springer, 2011).

[86] W. C. Oliver and G. M. Pharr, J. Mater. Res. **19**, 3 (2004).

[87] A. Revil and P. W. J. Glover, Phys. Rev. B **55**, 1757 (1997).

[88] H. Wang and L. Pilon, J. Phys. Chem. C **115**, 16711 (2011).

[89] J. Clavilier and N. Van Huong, J. Electroanal. Chem. Interfacial Electrochem. **41**, 193 (1973).

[90] M. Smetanin, R. N. Viswanath, D. Kramer, D. Beckmann, T. Koch, L. A. Kibler, D. M. Kolb, and J. Weissmüller, Langmuir **24**, 8561 (2008).

[91] P. Simon and Y. Gogotsi, Nat. Mater. **7**, 845 (2008).

[92] G. Jerkiewicz, G. Vatankhah, J. Lessard, M. P. Soriaga, and Y.-S. Park, Electrochim. Acta **49**, 1451 (2004).

[93] H. Angerstein-Kozlowska, B. E. Conway, K. Tellefsen, and B. Barnett, Electrochim. Acta **34**, 1045 (1989).

[94] H. Angerstein-Kozlowska, B. E. Conway, A. Hamelin, and L. Stoicoviciu, J. Electroanal. Chem. Interfacial Electrochem. **228**, 429 (1987).

[95] H. Angerstein-Kozlowska, B. E. Conway, B. Barnett, and J. Mozota, J. Electroanal. Chem. Interfacial Electrochem. **100**, 417 (1979).

[96] H.-J. Jin, L. Kurmanaeva, J. Schmauch, H. Rösner, Y. Ivanisenko, and J. Weissmüller, Acta Mater. **57**, 2665 (2009).

[97] M. M. Biener, J. Biener, A. Wichmann, A. Wittstock, T. F. Baumann, M. Bäumer, and A. V Hamza, Nano Lett. **11**, 3085 (2011).

[98] K. Kolluri and M. J. Demkowicz, Acta Mater. **59**, 7645 (2011).

[99] C. Jeyabharathi, P. Ahrens, U. Hasse, and F. Scholz, J. Solid State Electrochem. **20**, 3025 (2016).

[100] H.-J. Jin and J. Weissmüller, Science (80-.). **332**, 1179 LP (2011).

[101] C. Gabrielli, *Indentification of Electrochemical Process by Frequency Reponse Analysis in Solatron Insrumentation* (1989).

[102] I. Epelboin, C. Gabrielli, M. Keddam, and H. Takenouti, Electrochim. Acta **20**, 913 (1975).

[103] M. Pourbaix, *Atlas of Electrochemical Equilibria in Aqueous Solutions*, 1st editio (OXford, New York, Pergamon Press, New York, 1966).

[104] S. Cherevko, A. R. Zeradjanin, G. P. Keeley, and K. J. J. Mayrhofer, J. Electrochem. Soc.

161, H822 (2014).
[105] L. D. Burke and P. F. Nugent, Gold Bull. **31**, 39 (1998).
[106] S. J. Zinkle, L. E. Seitzman, and W. G. Wolfer, Philos. Mag. A **55**, 111 (1987).
[107] M. Kiritani, Mater. Chem. Phys. **50**, 133 (1997).
[108] B. N. Singh and S. J. Zinkle, J. Nucl. Mater. **206**, 212 (1993).
[109] *X-Ray Data File No.: 00-044-0784, International Centre for Diffraction Data* (2016).
[110] L. C. Wang, Y. Zhong, H.-J. Jin, D. Widmann, J. Weissmuller, and R. J. Behm, Beilstein J. Nanotechnol. **4**, 111 (2013).
[111] E. Seker, L. M. Reed, and R. M. Begley, Mater. **2**, (2009).
[112] V. Zielasek, B. Jürgens, C. Schulz, J. Biener, M. M. Biener, A. V Hamza, and M. Bäumer, Angew. Chemie Int. Ed. **45**, 8241 (2006).
[113] S. Trasatti and O. A. Petrii, J. Electroanal. Chem. **327**, 353 (1992).
[114] E. Rouya, S. Cattarin, M. L. Reed, R. G. Kelly, and G. Zangari, J. Electrochem. Soc. **159**, K97 (2012).
[115] Y. Liu, S. Bliznakov, and N. Dimitrov, J. Phys. Chem. C **113**, 12362 (2009).
[116] S. Brunauer, P. H. Emmett, and E. Teller, J. Am. Chem. Soc. **60**, 309 (1938).
[117] K. S. W. Sing, Adv. Colloid Interface Sci. **76–77**, 3 (1998).
[118] O. M. Magnussen, J. Wiechers, and R. J. Behm, Surf. Sci. **289**, 139 (1993).
[119] O. M. Magnussen, J. Hotlos, R. J. Behm, N. Batina, and D. M. Kolb, Surf. Sci. **296**, 310 (1993).
[120] M. A. V Devanathan and B. V. K. S. R. A. Tilak, Chem. Rev. **65**, 635 (1965).
[121] H.-J. Jin, S. Parida, D. Kramer, and J. Weissmüller, Surf. Sci. **602**, 3588 (2008).
[122] R. N. Viswanath, D. Kramer, and J. Weissmüller, Electrochim. Acta **53**, 2757 (2008).
[123] D. M. Kolb, Prog. Surf. Sci. **51**, 109 (1996).
[124] Y. H. Tan, J. A. Davis, K. Fujikawa, N. V. Ganesh, A. V Demchenko, and K. J. Stine, J. Mater. Chem. **22**, 6733 (2012).
[125] F. Weigend, F. Evers, and J. Weissmüller, Small **2**, 1497 (2006).
[126] K. R. Painter, P. Ballone, M. P. Tosi, P. J. Grout, and N. H. March, Surf. Sci. **133**, 89 (1983).
[127] N. Huber, R. N. Viswanath, N. Mameka, J. Markmann, and J. Weißmüller, Acta Mater. **67**, 252 (2014).
[128] H. Gleiter, Prog. Mater. Sci. **33**, 223 (1989).
[129] V. S. Bagotzky and M. R. Tarasevich, J. Electroanal. Chem. Interfacial Electrochem. **101**, 1 (1979).
[130] C. Lakshmanan, A. K. Behera, R. N. Viswanath, S. Amirthapandian, R. Rajaraman, and G. Amarendra, Scr. Mater. **146**, 68 (2018).
[131] R. Paulin, R. Ripon, and W. Brandt, Phys. Rev. Lett. **31**, 1214 (1973).
[132] W. Brandt and R. Paulin, Phys. Rev. B **5**, 2430 (1972).
[133] A. Dupasquier and A. P. Mills Jr., *Positron Spectroscopy of Solids* (IOS Press, 1995).
[134] B. Oberdorfer and R. Würschum, Phys. Rev. B **79**, 184103 (2009).
[135] G. Amarendra, B. Viswanathan, G. Venugopal Rao, J. Parimala, and B. Purniah, Curr. Sci. **73**, 409 (1997).
[136] J. Erlebacher, Phys. Rev. Lett. **106**, 225504 (2011).
[137] D. G. Lock and R. N. West, Phys. Lett. A **49**, 137 (1974).
[138] O. MOGENSEN, K. PETERSEN, R. M. J. COTTERILL, and B. HUDSON, Nature **239**, 98 (1972).
[139] A. P. Mills, Phys. Rev. Lett. **41**, 1828 (1978).
[140] P. G. Coleman, R. E. Mason, M. Van Dyken, and A. P. Knights, J. Phys. Condens. Matter **17**, S2323 (2005).
[141] R. Kloske and J. W. Kauffman, Phys. Rev. **126**, 123 (1962).
[142] D. A. Grenning and J. S. Koehler, Phys. Rev. **144**, 439 (1966).
[143] R. Schaeublin, M.-J. Caturla, M. Wall, T. Felter, M. Fluss, B. D. Wirth, T. Diaz de la Rubia, and M. Victoria, J. Nucl. Mater. **307–311**, 988 (2002).
[144] E. Soininen, H. Huomo, P. A. Huttunen, J. Mäkinen, A. Vehanen, and P. Hautojärvi, Phys. Rev. B **41**, 6227 (1990).

[145] J. Weissmüller, R. C. Newman, H.-J. Jin, A. M. Hodge, and J. W. Kysar, MRS Bull. **34**, 577 (2009).

[146] A. Leitner, V. Maier-Kiener, J. Jeong, M. D. Abad, P. Hosemann, S. H. Oh, and D. Kiener, Acta Mater. **121**, 104 (2016).

[147] E. Martínez and B. P. Uberuaga, Sci. Rep. **5**, 9084 (2015).

[148] B. N. Singh, S. I. Golubov, H. Trinkaus, D. J. Edwards, and M. Eldrup, J. Nucl. Mater. **328**, 77 (2004).

[149] L. A. Zepeda-Ruiz, E. Martinez, M. Caro, E. G. Fu, and A. Caro, Appl. Phys. Lett. **103**, 31909 (2013).

[150] M. Caro, W. M. Mook, E. G. Fu, Y. Q. Wang, C. Sheehan, E. Martinez, J. K. Baldwin, and A. Caro, Appl. Phys. Lett. **104**, 233109 (2014).

[151] F. R. A., F. C. W., and O. W. J., J. Biomed. Mater. Res. **7**, 471 (2018).

[152] J. Fischer-Bühner, Gold Bull. **38**, 120 (2005).

[153] A. Kareer, A. Prasitthipayong, D. Krumwiede, D. Collins, P. Hosemann, and S. Roberts, J. Nucl. Mater. **498**, 274 (2017).

[154] S. Pecko, C. Heintze, F. Bergner, W. Anwand, and V. Slugeň, Nucl. Instruments Methods Phys. Res. Sect. B Beam Interact. with Mater. Atoms **415**, 1 (2018).

[155] C. J. Ruestes, C. Anders, E. M. Bringa, and H. M. Urbassek, J. Appl. Phys. **123**, 225903 (2018).

[156] T. Diaz de la Rubia, H. M. Zbib, T. A. Khraishi, B. D. Wirth, M. Victoria, and M. J. Caturla, Nature **406**, 871 (2000).

[157] J. S. Robach, I. M. Robertson, B. D. Wirth, and A. Arsenlis, Philos. Mag. **83**, 955 (2003).

[158] E. Figueroa, D. Tramontina, G. Gutiérrez, and E. Bringa, J. Nucl. Mater. **467**, 677 (2015).

[159] R. W. Hertzberg, *Deformation and Fracture Mechanics of Engineering Materials* (John Wiley & Sons, 1989).

[160] Y. A. Chang, L. M. Pike, C. T. Liu, A. R. Bilbrey, and D. S. Stone, Intermetallics **1**, 107 (1993).

[161] L. M. Pike, Y. A. Chang, and C. T. Liu, Acta Mater. **45**, 3709 (1997).